MECHANICAL METAMATERIALS:

NONLINEAR BEAMS AND EXCESS ZERO MODES

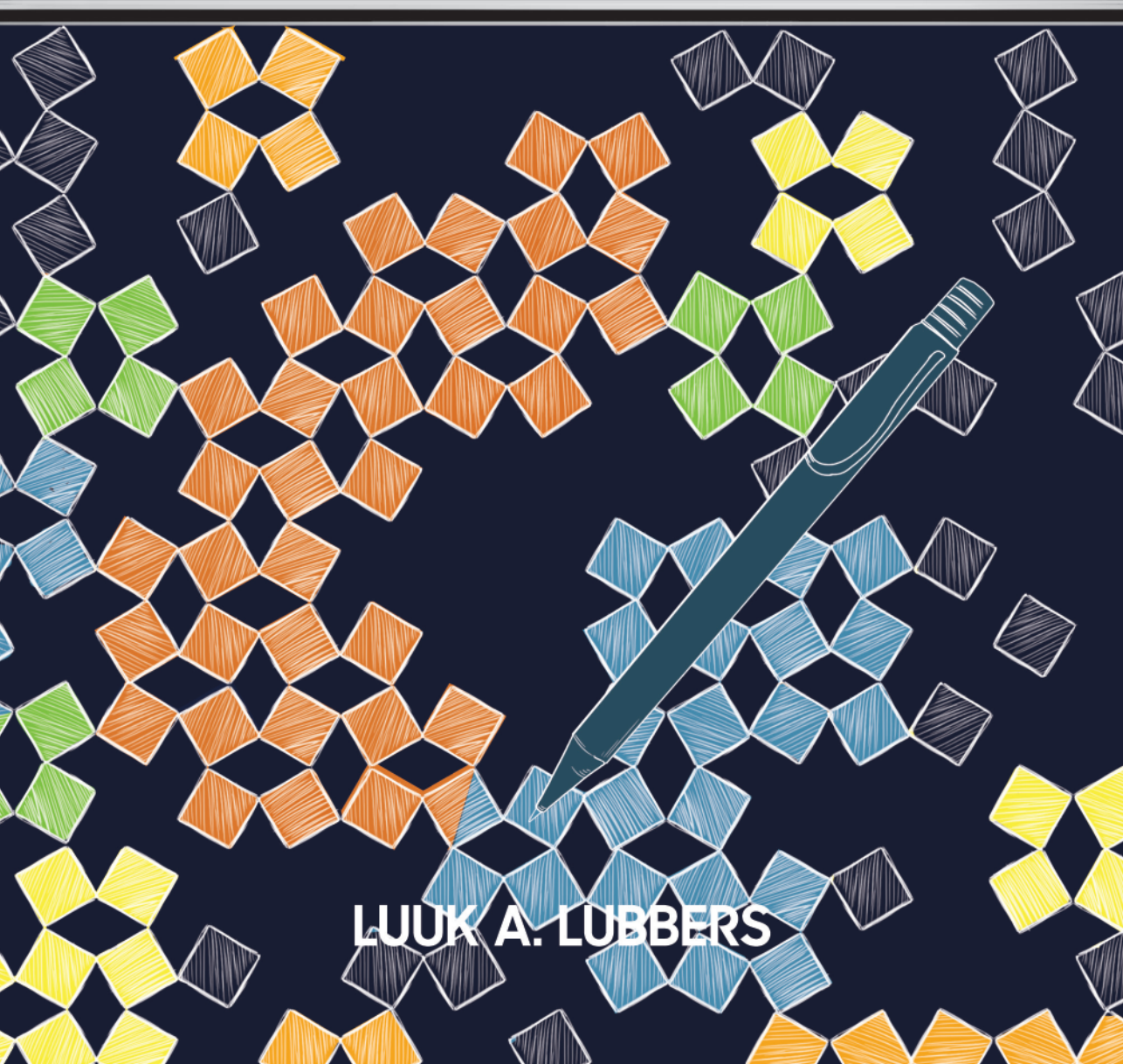

LUUK A. LUBBERS

Mechanical Metamaterials:

Nonlinear Beams and *Excess Zero Modes*

PROEFSCHRIFT

ter verkrijging van
de graad van Doctor aan de Universiteit Leiden,
op gezag van Rector Magnificus Prof. mr. C.J.J.M. Stolker,
volgens besluit van het College voor Promoties
te verdedigen op donderdag 13 september 2018
klokke 11.15 uur

door

Luuk Antonius Lubbers
geboren te Oldenzaal
in 1989

Promotor:
Prof. dr. M.L. van Hecke

Promotiecommissie:
Dr. C. Coulais (*Universiteit Amsterdam*)
Prof. dr. ir. J.H. Snoeijer (*Technische Universiteit Twente*)
Prof. dr. J. Aarts
Prof. dr. E.R. Eliel
Dr. D.J. Kraft
Prof. dr. H. Schiessel

The work described in this thesis was carried out at the Leiden Institute of Physics (LION) of Leiden University and partly at the research institute AMOLF in Amsterdam. It was funded by The Netherlands Organization for Scientific Research (NWO) through a VICI grant, NWO-680-47-609.

Nederlandse titel:
Mechanische Metamaterialen: Niet-lineare Staven en Buitengewone Vrije Bewegingen.

Cover image:
The cover shows a collection of hinging squares with a random linking topology ($\rho \approx 0.3$) in which clusters of densely connected squares are coloured; squares belong to zero (black), one (coloured) or two clusters (bi-coloured). Graphic design by Evelien Jagtman.

Casimir PhD series, Delft-Leiden, 2018-26
ISBN 978-90-8593-355-7

Contents

1 Introduction

Mechanical metamaterials are man-made materials which derive their unusual properties from their structure rather than their composition. Their spatial structure, or architecture, often consists of periodically arranged building blocks whose mutual interactions realize unusual properties, such as zero or negative elastic parameters [1].

Anyone playing with a piece of rubber will have noticed that its sides expand when squeezing it. This is because rubber is essentially incompressible: Volume changes are energetically much more expensive than volume-preserving deformations. This example demonstrates material behaviour which is characterized by a positive Poisson's ratio (defined as the negative ratio of the transverse to axial strain [2]): Compressing (stretching) the material in one direction leads to the expansion (contraction) in directions transverse to the applied force [Fig. 1.1(a)]. Although a positive Poisson's ratio is a material property shared among the vast majority of conventional materials, the recent development of *mechanical metamaterials* realized the practical design of negative Poisson's ratio materials [3, 4]. These are counter-intuitive materials that either contract or expand in all directions when a force is applied [Fig. 1.1(b)], and are also known as *auxetic* materials or simply *auxetics*. Auxetics are widely studied because they feature enhanced properties in comparison to traditional materials, such as a higher indentation [5, 6] and fracture resistance [7], improved energy absorption [8] and the ability to perfectly wrap around objects such as spheres or domes [9–11]. The latter characteristic is for example exploited in industry to optimize the fit of footwear and prosthetics [12], but also for the design of curved aircraft wings and helicopter rotor blades [10, 13, 14].

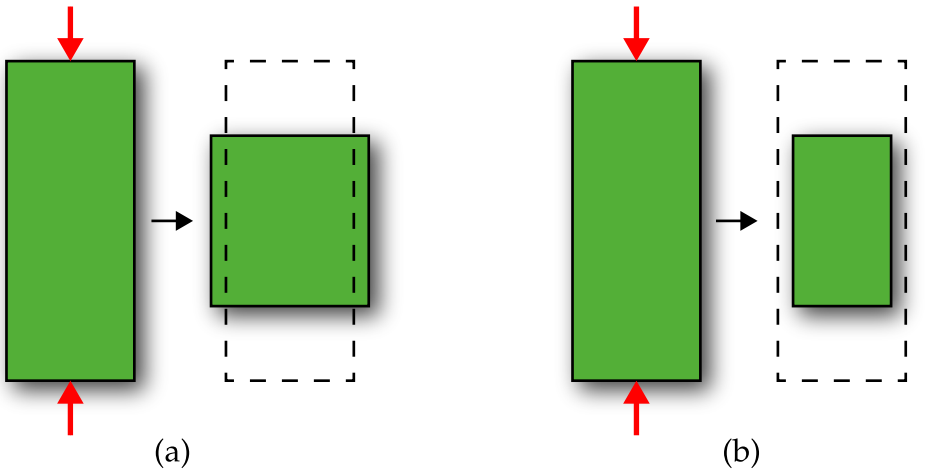

Figure 1.1: Initial and deformed shapes for the uniaxial compression of (a) conventional and (b) auxetic materials. Dashed lines plotted on top of the deformed shapes indicate initial material geometry.

The first development of an artificial auxetic metamaterial was reported in 1987 by Lakes [3]. His famous work outlines how auxetic foams can be produced from conventional foams by designing a structure consisting of three-dimensional, re-entrant unit cells (unit cells with inward deflected sides), and thus demonstrates how structure rather than composition determines the properties of the metamaterial. The regular, two-dimensional equivalent of the underlying re-entrant unit cell is shown in Fig. 1.2(a), which illustrates how a lattice of inverted honeycomb cells obtains its negative macroscopic Poisson's ratio. Followed by the work of Lakes, several other structures have been presented to architect auxetics [15–19]. Auxetic behaviour is particularly pronounced for the hinging motion of a collection of rigid squares [20] linked at their tips by flexible hinges [Fig. 1.2(b)]. This freely hinging, zero-energy motion, known as a *mechanism*, is characterized by the counter-rotations of squares (as indicated by circle-shaped arrows) that leads to a uniform contraction or expansion of the structure.

The key aspect that facilitates the auxetic behaviour for the model of hinged squares, are the sharp tips which connect adjacent squares [zoomed area in Fig. 1.2(b)]. These tips introduce strongly localized de-

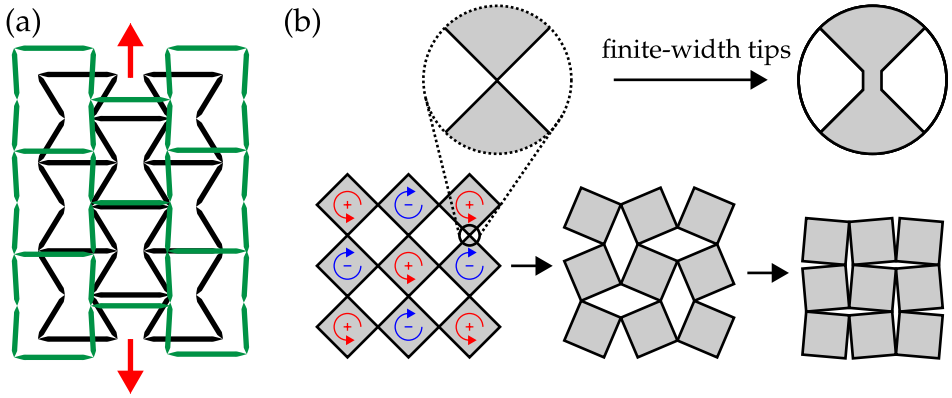

Figure 1.2: Auxetic metamaterials. (a) Structure with inverted honeycomb cells, which expands (shrinks) in the lateral direction when stretched (compressed) [21]. (b) A collection of squares linked at their tips exhibits a free hinging motion (indicated by the coloured arrows), which allows the structure to uniformly contract or expand [20]. Zoomed areas: The sharp tips localize bending and approximate ideal hinges (left). Finite-width tips can be regarded as beams (right).

formations, in contrast to the uniform deformation of a homogeneous sample of rubber. As a result deformations are non-affine [22, 23] and the macroscopic response becomes qualitatively different from its constituent material. Put simply, sharp tips approximate ideal hinges that allow for zero-energy rotational motion of the squares [1]. Moving away from the limit of sharp-tips, finite-width tips [Fig. 1.2(b)] lead to a finite-energy motion which closely resembles the underlying mechanism. Nonetheless, finite-width tips, which can effectively be seen as beams, add complexity to the mechanical properties of the metamaterial. Whereas deformations in sharp tips are entirely bending dominated, the beams in finite-width tips also undergo compressive deformations when excited by an external axial force. The mechanical complexity then arises from the energetic competition between compressive and bending deformations, and can lead to spontaneous symmetry breaking from straight to bent beams. This phenomenon is known as the buckling instability [24], which is associated with a strongly nonlinear relation between macroscopic stresses and strains. Metamaterials that encompass such a buckling instability are known as buckling-based metamaterials [1].

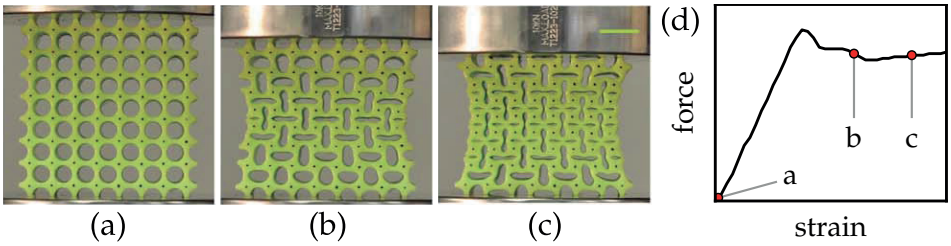

Figure 1.3: Buckling-based auxetic metamaterial. (a-c) Subsequent snapshots for the uniaxial compression of an elastic sheet patterned by circular holes. Under a sufficient load the beam elements undergo a collective buckling instability which induces a pattern transformation from holes to orthogonal ellipses. This pattern switch underlies the mechanism of rotating squares and results in an auxetic response (note how the sides move inwards). (d) Corresponding (experimental) force-strain relation with the (relative) forces and strains associated with panels (a-c) indicated by filled circles. Reproduced from reference [28] with permission from The Royal Society of Chemistry.

The simplest example of a buckling-based metamaterial is an elastic sheet patterned by a square array of circular holes [4, 25–28] as displayed in Fig. 1.3(a), which effectively resembles a structure of rigid squares connected by beams. When uniaxially compressed, the structure undergoes a pattern transformation, as shown in Fig. 1.3(a-c), which is triggered by a collective beam buckling instability. The scenario of collective beam buckling is reflected by the kink (at the maximum force) in the force-strain curve shown in panel (d), which is typical for a buckling instability [24]. Importantly, the characteristics of this pattern transformation are determined by the underlying mechanism. Hence, the properties of this metamaterial are determined by the interplay between the mechanical functionality of the beam elements, and the shape-changing properties of the underlying mechanism [29]. Both of these ingredients play a central role in this thesis, and in the sections hereafter we will discuss their properties in more detail.

1.1 Structural elastic instabilities

The loss of mechanical stability in elastic structures is widely studied and traditionally driven by the desire to design workarounds that can pre-

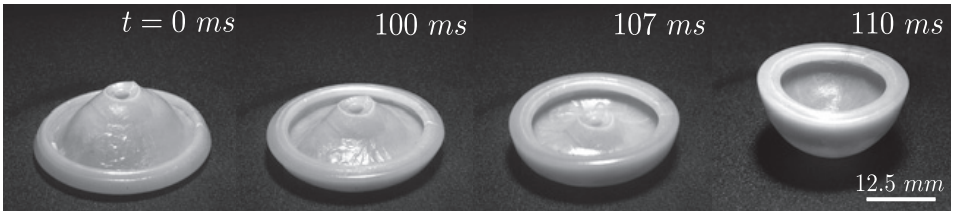

Figure 1.4: Snapping of a jumping popper toy. In order to jump, the shell like-structure first needs to be turned inside out to store elastic energy. Subsequently, the snap-through instability can be triggered by dropping it from a small height. The associated rapid change in curvature converts elastic energy into kinetic energy with an audible pop and causes the toy to jump. Image courtesy of D. Holmes, Boston University; the image has been published in reference [35].

vent structural failure [30]. Objects of focus have mainly been slender structural elements which are prone to buckling and snap-through instabilities, such as beams, plates, shells and frames [30]. More recently, structural instabilities of slender structures are recognized as an opportunity to generate new modes of functionalities in advanced materials [31]. In fact, biological systems make use of instabilities to obtain their functionality. Examples include the Venus fly trap [32] and the waterwheel plant [33], which exploit the rapid dynamics of a snap-through instability to catch their prey. Moreover, snapping lies at the basis of jumping bimetallic disks [34] and rubber popper toys [35] (Fig 1.4), which snap back towards their stable state after being turned inside-out.

Metamaterials that utilize structural instabilities for their functionality are known as instability-based metamaterials [1]. Buckling-based metamaterials [4, 25–28, 36–38] constitute a subclass of instability-based metamaterials that rely specifically on Euler buckling — known as the phenomenon where an elastic beam buckles under a sufficiently large compressive axial load [24], which is perhaps the simplest and most widespread instability. This type of metamaterials exhibit post-instabilities when subjected to compression, due to the collective buckling of beam ligaments which connect adjacent building blocks (e.g. as in Fig. 1.3). Although the pre-buckling regime and the onset of buckling is well understood, their post-buckling behaviour, which usually occurs far from equilibrium accompanied by large beam deformations, is not well developed yet [39]. In particular, the negative post-buckling stiffness, char-

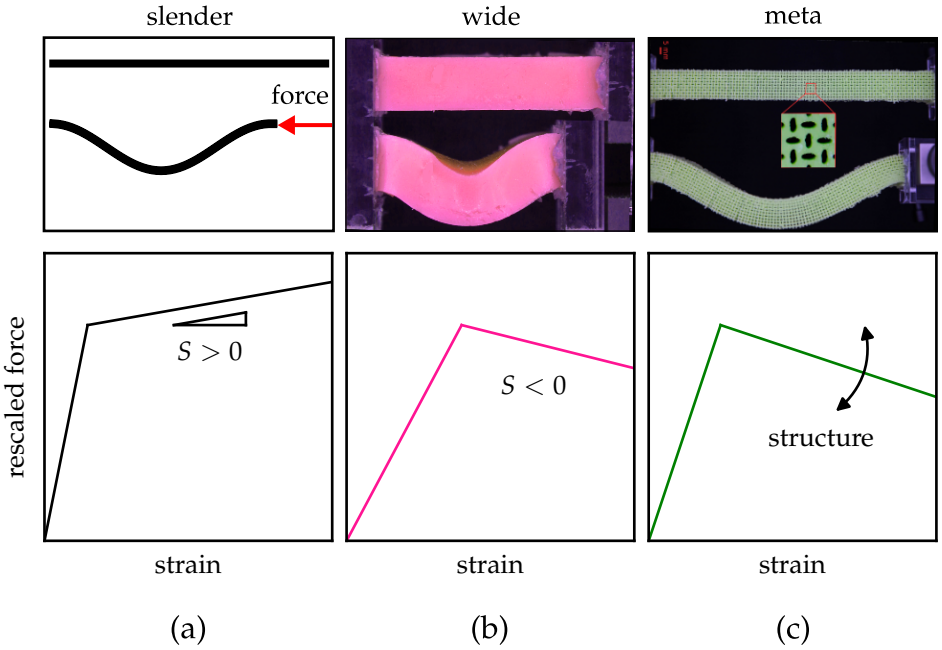

Figure 1.5: Force-displacement curves for the buckling of (a) slender beams, (b) wide beams and (c) metabeams. The post-buckling stiffness is quantified by the slope after buckling, S. For plain beams the post-buckling slope is a function of the beam width. The post-buckling slope of metabeams, however, can be tuned independently of beam width by changing their elliptical pore shapes. Other than utilizing instabilities, metamaterials can thus also be leveraged to change elastic instabilities. Image adapted from [40].

acterized by a decreasing force after buckling [Fig. 1.3(d)], is not well understood. Recently, we showed that the simplest possible setting in which the negative stiffness can be reproduced is on the level of a single beam ligament [40]. Fig. 1.5(a-b) shows how beam width crucially influences the post-buckling stiffness of beams: Slender beams display an increasing force after buckling (positive stiffness), but for wide beams the force after buckling decreases (negative stiffness). Metabeams [Fig. 1.5(c)], which are beams patterned with elliptical holes, can even be used to rationally design any post-buckling stiffness [40]. To our surprise negative post-buckling stiffness in the context of beams is not captured by existing models [41–43] and needless to say, a full understanding of the post-

buckling behaviour of beams is necessary to take full advantage of the buckling instability in the design of buckling-based metamaterials.

In conclusion, sufficiently wide beams exhibit a negative post-buckling stiffness. This intriguing post-buckling behaviour is accompanied by large deformations, a combination which is theoretically not well described. Motivated by the role of (wide) beam ligaments in buckling-induced metamaterials, analysis of the post-buckling properties of beams plays a central role in this thesis. In chapter 2, we first identify the physical ingredient that induces negative post-buckling stiffness, followed by the development of a 1D model that accurately predicts the experimentally and numerically observed negative stiffness without adjustable parameters.

1.2 Role of geometry

In this section we zoom in on the role of geometry in the micro structure of mechanical metamaterials. We focus on the micro structure consisting of hinged square tiles [Fig. 1.2(b)], which composes the backbone of a range of 2D auxetic metamaterials [4, 20, 25–28] and which has inspired the design of programmable [44] and 3D mechanical metamaterials [36, 38]. Owing to its geometric design, the model of hinged squares provides a single zero-energy motion when connected by flexible linkers, also known as a mechanism or zero mode [1]. Consequently, metamaterials underlying the micro structure of hinged squares feature a single predefined mode of deformation. The natural question that arises is then whether new metamaterials can be constructed which are able to morph into multiple predefined shapes when excited by external forces.

To answer this question, we enlarge the design space and study mechanical metamaterials composed of aperiodic, rather than periodic micro structures. Recently, aperiodicity originating from unit cell orientations was applied to 3D mechanical metamaterials for the rational design of arbitrary pre-programmable shape changes [38] — featuring a single mode of deformation per chosen geometry. In this thesis, we construct 2D aperiodic micro structures by diluting (removing squares) the mechanism of hinged squares in order to pre-program multiple shape changes per geometry. Obviously, aperiodicity opens up pathways for the possible design of such structures, since the design space is greatly increased as a

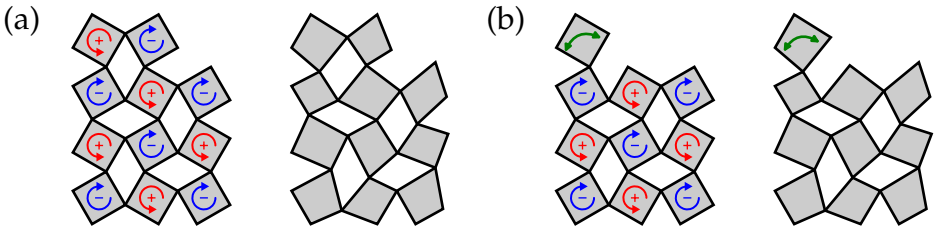

Figure 1.6: Symmetric versus generic systems. (a) The symmetric system (left) allows for a global hinging zero mode in which quads collectively counter rotate (indicated by the coloured arrows), but the generic system (right) is rigid. (b) Removing a quad from the top row allows the remaining quad on top to freely hinge (indicated by the green arrow), introducing an extra zero mode in both the symmetric and generic system.

result of square removal: For full filling, there exists only one way to tile space, but this number grows rapidly when squares are removed.

The resulting diluted systems comprise a two-fold problem. First, as mentioned, the diluted systems are interesting from the metamaterials perspective. Second, the non-generic nature of the square building blocks provides potential to unravel the rigidity of (randomly) diluted symmetric systems. The work presented in this thesis studies both of these aspects and will build a bridge between them. The rigidity of random spring networks has been widely studied [45–50], and is known as rigidity percolation. So far, the focus has been on generic disordered systems, in order to avoid degeneracies arising when symmetries are present. In this thesis however, we study the differences that arise between the rigidity of symmetric and generic systems.

Fig. 1.6 demonstrates two geometries for which the rigidity of systems composed by symmetric squares behave differently from systems composed by generic quads. First, panel (a) shows that sufficiently large generic systems are rigid, in contrast to symmetric systems that always exhibit a hinging mechanism, independently of system size. Using Maxwell counting [51], as will be discussed in chapter 3, it can readily be shown that the minimum system size to ensure rigidity of generic systems is 3×3. Next, panel (b) shows that removing a quad from the top row introduces an additional zero mode in both the symmetric and generic system. Thus, panel (a-b) show two examples in which symmet-

ric systems exhibit one *excess zero mode* in comparison with its generic counterpart. It is conceivable, however, that the number of excess zero modes is not bounded to one, but can become larger for more complex geometries — examples will be discussed in chapter 3.

The above examples demonstrate some of the complexity occurring in the rigidity of symmetric systems and several open questions arise. Can the number of excess zero modes become arbitrary large? What are the necessary ingredients that facilitate the excess zero modes? How can we count the number of excess zero modes given a random dilution pattern? A comprehensive treatise on these questions, and more, are devoted to chapters 3 and 4 of this thesis.

1.3 In this thesis

In this thesis we investigate two aspects of mechanical metamaterials: The role of beam ligaments and the role of symmetries. As motivated above, both aspects play an important role in mechanical metamaterials, and give rise to several open questions.

We first elucidate the negative post-buckling stiffness of wide neo-Hookean beams in chapter 2. We show that the negative stiffness occurs in experiments, 3D simulations and simplified 2D simulations, demonstrating that negative post-buckling stiffness is a robust phenomenon that does not originate from boundary-induced singularities or 3D effects. Using the simplified 2D simulations we then identify the missing physical ingredient — which we will show to be a material nonlinearity — that underlies the negative post-buckling stiffness. Finally, we use this material nonlinearity to build a 1D nonlinear beam model that, without adjustable parameters, successfully captures the intriguing post-buckling behaviour of wide neo-Hookean beams.

In the remainder of this thesis we turn to collections of hinging quadrilaterals in order to probe the role of symmetries. In chapter 3 we investigate randomly diluted lattices of hinging squares, and compare these directly to generic systems featuring irregular quads, when using the same dilution pattern for both. We then demonstrate that symmetric systems exhibit excess zero modes as compared to the generic systems, with their multitude satisfying simple scaling relations with mean field exponents.

Finally, in chapter 4 we develop an approximate, yet accurate method

to count the number of excess zero modes in diluted systems of hinging squares. We note that these modes are driven by densely connected patches of quads — clusters — and develop a procedure to separate any system into clusters, connectors and remaining quads. Using the topology of the clusters and their connectors we then iteratively estimate the number of (excess) zero modes, which allows us to obtain a tight lower bound on the exact, numerical results for their multitude.

2

A nonlinear beam model to describe the post-buckling of wide neo-Hookean beams

Wide beams can exhibit subcritical buckling, i.e. the slope of the force-displacement curve can become negative in the post-buckling regime. In this chapter, we capture this intriguing behaviour by constructing a 1D nonlinear beam model, where the central ingredient is the nonlinearity in the stress-strain relation of the beam's constitutive material. First, we present experimental and numerical evidence of a transition to subcritical buckling for wide neo-Hookean [52] hyperelastic beams, when their width-to-length ratio exceeds a critical value of 12%. Second, we construct an effective 1D energy density by combining the Mindlin-Reissner kinematics [41] with a nonlinearity in the stress-strain relation. Finally, we establish and solve the governing beam equations to analytically determine the slope of the force-displacement curve in the post-buckling regime. We find, without any adjustable parameters, excellent agreement between the 1D theory, experiments and simulations. Our work extends the understanding of the post-buckling of structures made of wide elastic beams and opens up avenues for the reverse-engineering of instabilities in soft and metamaterials.

The work presented in this chapter has been published as:

C. Coulais, J.T.B. Overvelde, **L.A. Lubbers**, K. Bertoldi and M. van Hecke, *Discontinuous buckling of wide beams and metabeams*, Phys. Rev. Lett. **115**, 044301 (2015).

L.A. Lubbers, M. van Hecke and C. Coulais, *A nonlinear beam model to describe the post-buckling of wide neo-Hookean beams*, J. Phys. Mech. Solids **106**, 191-206 (2017).

Guide through this chapter: Readers interested in the main findings can safely skip sections 2.3 to 2.5. These sections are very technical, but provide essential background information to unambiguously construct the energy density which forms the basis of our nonlinear beam model.

2.1 Introduction

Recent years have seen an upsurge of interest in the instabilities and post-instability behaviour of flexible structures. Rather than seeing instabilities as failure, they recently have been leveraged to achieve novel functional (meta)materials and structures [31, 53]. As such, materials and structures featuring snapping [44, 54], wrinkling [55, 56], fingering [57] or buckling [4, 36, 40] have been created. Collectively they constitute a promising route to develop mechanical devices for sensing [38, 58], actuation [55, 59–61] or soft robotics [62, 63].

These structures harness post-instabilities *and* their constituents undergo large deformations. A theoretical description of this regime, where as we will show nonlinearities are key, is not well developed yet. On the one hand, the description of post-buckling behaviour has been widely investigated, but for models in which the constitutive material is assumed to be linearly elastic under small deformations [30, 42, 43, 64–68]. On the other hand, much attention has been devoted to characterizing the instabilities of nonlinear elastic cellular materials [69–72] or structures [73], but only for the onset of instability, and not for the post-instability regime.

Euler buckling, known as the phenomenon where an elastic beam will buckle under a sufficiently large compressive axial load, is perhaps the simplest and the most widespread instability [24]. Much theoretical attention has been devoted to describing it using the classical [74, 75], extensible and shearable [76] elastica problem. Further in-depth studies have focused on the onset of buckling, the structure of buckled states [77, 78], closed form solutions [79–81], large deformations [82–84] and three-dimensional [85–88] deformations. In this chapter we investigate the post-buckling regime of wide beams, where strains are necessarily large. A salient feature of buckling of slender beams is that the post-buckling compliance increases tremendously after buckling, yet remains positive. However, as discussed in the general introduction of this thesis, wide beams that buckle and undergo large deformations can exhibit a negative

post-buckling compliance [40]. Although negative compliance is commonly observed in buckling of shells [30], pipes [64] and the wrinkling of membranes [89–91], it has not been reported for Euler beam buckling, and to the best of our knowledge is not predicted by existing beam models.

Here we develop a 1D nonlinear beam model based on a nonlinear constitutive equation, that without adjustable parameters, describes the post-buckling compliance of wide neo-Hookean beams. In particular, this model allows to analytically capture the onset of subcritical buckling (post-buckling slope < 0) for widths larger than approximately 15%, in good agreement with experiments and FEM simulations. First, in section 2.2 we present experimental and numerical evidence to show that for neo-Hookean beams, the post-buckling compliance becomes negative when the beam width-to-length ratio t exceeds approximately 12%. Second, in sections 2.3-2.5 we discuss the fundamental ingredients for our 1D model. We review mathematical beam descriptions based on Mindlin-Reissner kinematics [41], pinpoint and quantify the role of material nonlinearity using extensive 2D simulations, and construct a 1D energy density that encompasses such nonlinearity by combining the Mindlin-Reissner kinematics with a nonlinearity in the stress-strain relation. Third, in section 2.6 we establish the governing equations of our nonlinear 1D beam model that are based on this energy density including nonlinearity. We then solve the beam equations to obtain the variation of the post-buckling slope with t and find that, without any adjustable parameters, our model is in excellent agreement with experiments and simulations. Our work thus unambiguously unravels the link between stress-strain nonlinearity and post-buckling behaviour. While we focus on the buckling of wide neo-Hookean beams, we note that we only need to include quadratic corrections to the stress-strain relation to correctly capture the physics. Hence, for materials with other nonlinear constitutive laws, including metamaterials as explored in [40] and [92], our description is also valid. Our analytical description can be used to rationally design the post-buckling behaviour of beams, and we hope that it can inspire work to capture and describe post-instability behaviours of other elastic systems. More widely, our work may impact the design of compliant devices, which harness instabilities (e.g. buckling, snapping, wrinkling) to convey mechanical functionalities that are of use in soft robotics [62, 63], sensors [38, 58] and actuators [55, 59–61].

2.2 Phenomenology: Subcritical buckling

In this section, we present and expand the findings from our previous work on subcritical buckling of wide beams [40]. First, we discuss both the experimental and numerical protocols to study buckling of rectangular beams to determine the force-displacement relation. We consider both the numerical protocol for 3D FEM simulations with boundary conditions that closely model the experimental conditions, and 2D simulations with simplified boundary conditions. Second, we analyse the onset of buckling and the post-buckling compliance of beams of varying width-to-length ratio t. We then show that for both experiments and numerics the post-buckling compliance varies systematically with t, and becomes negative for $t \gtrsim 0.12$.

2.2.1 Experiments and FEM simulations

In the analysis below, we consider beams of the width-to-length ratio $t = w/\ell$ and depth d, under load F and corresponding uniaxial displacement u, where $u, F > 0$ correspond to a compressive deformation [Fig. 2.1(a-b)].

Experiments

To perform buckling experiments, we mold 12 solid rectangular beams of rest length $\ell = 45$ mm, depth $d = 35$ mm and widths ranging from $w = 1.55$ mm to $w = 12.85$ mm [Fig. 2.1(a)] out of a well-characterized silicon rubber (Zhermarck, Polyvinyl Siloxane double elite 8, density 1.15×10^3 kg/m^3, Young's modulus $E = 250$ kPa, Poisson's ratio $\nu \approx 0.5$). The extremities of the beams are glued on plexiglass plates that are attached to the uniaxial testing device (Instron 5965) in order to approximate clamped-clamped boundary conditions, and we perform the experiments in a water bath in order to limit the effects of gravity.

3D simulations

We simultaneously carry out a nonlinear analysis using the commercial finite element package Abaqus/Standard on beams with the exact same geometry as in the experiments. We determine the buckling point using a specific algorithm in our finite element code that does not require seeding

the initial geometry with imperfections (see appendix 2.A and reference [40]), allowing to obtain a 0.1% accuracy on the buckling onset.

Material model — The rubbers used in our experiments are well described by the incompressible neo-Hookean formulation of nonlinear elasticity [93]. We therefore use a neo-Hookean strain energy density [52] of the form

$$W = \frac{G}{2}\left(\det(\mathbf{F})^{-2/3}\mathrm{tr}(\mathbf{F}\mathbf{F}^{\mathbf{T}}) - 3\right) + \frac{K}{2}(\det(\mathbf{F}) - 1)^2, \tag{2.1}$$

where G is the shear modulus, K the bulk modulus and $\mathbf{F} \equiv \partial\mathbf{x}/\partial\mathbf{X}$ is the deformation gradient tensor from the undeformed coordinates $\mathbf{X}$ to the deformed coordinates $\mathbf{x}$. In the numerical analysis, we use the moduli $G = 83$ kPa and $K = 42$ GPa, which models accurately the $E = 250$ kPa nearly-incompressible rubber used in the experiments. We note that our results do not sensitively depend on the precise choice of G and K, as long as $G/K \ll 1$. The overall stiffness, given by the Young's modulus $E = 9KG/(3K + G)$, only sets a trivial scale, and to obtain dimensionless results, we scale the stresses by E for the results presented below.

Boundary conditions. — We numerically impose clamped-clamped boundary conditions to resemble the experiments where the endpoints of the beam are glued on plexiglass plates.

Simplified 2D FEM simulations

In addition, we carry out 2D plane stress simulations (Abaqus element type CPS4) using the same material model, yet with simplified slip boundary conditions at both endpoints of the beam, which allows for free lateral expansion at the clamped-clamped endpoints to avoid barrelling effects [94]. The choice for plane stress over plane strain conditions is a priory not obvious because our beams are intermediate between the plane stress limit ($w \gg d$), and plane strain limit ($w \ll d$). We therefore used our 3D simulations to investigate the 3D stresses and strains for beam thicknesses where the post-buckling slope changes sign ($t \approx 0.1$). We found that in this case there are significant out of plane strains, but that the out of plane stresses are small (ratio between the lateral and uniaxial stresses < 0.1) — this motivates us to focus on the plane stress case.

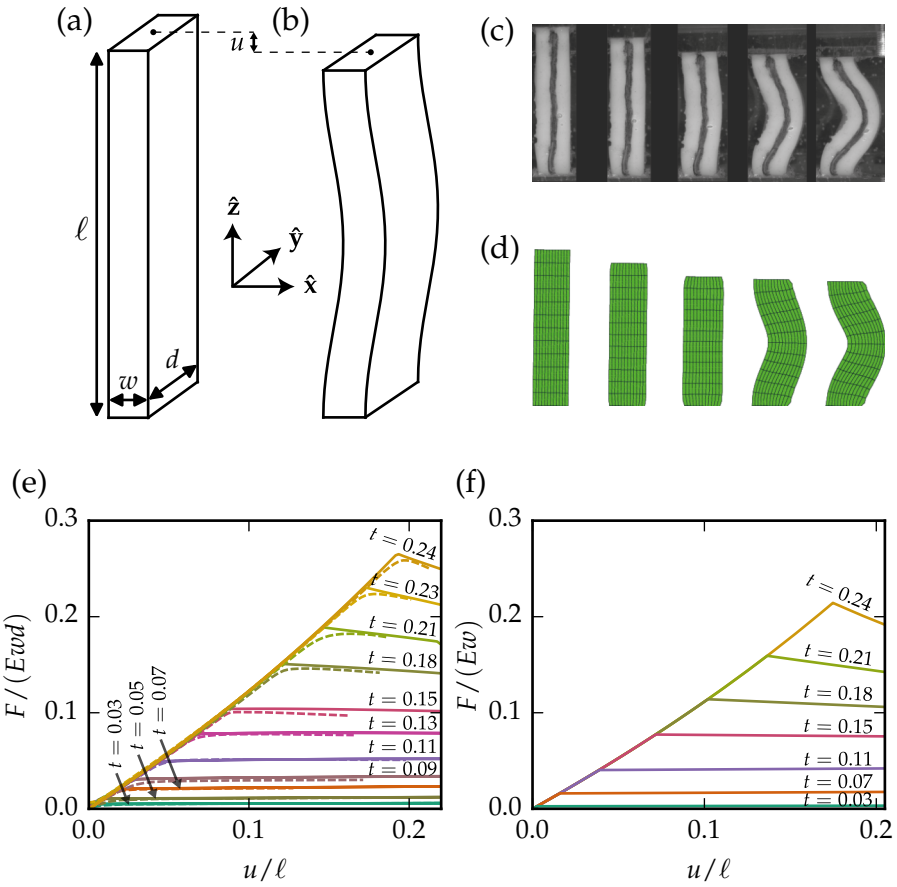

Figure 2.1: Buckling of wide neo-Hookean beams. (a) Sketch of a beam in its initial undeformed state, for which the beam has a rest length ℓ, width w and depth d. (b) Applying a compressive displacement u, leads to compression and eventually buckling of the beam. (c-d) Front-view snapshots of (c) the experiment and (d) the simulation for a beam of length $\ell = 45$ mm, depth $d = 35$ mm and width $w = 11.95$ mm, at compressive displacements (from left to right) $u = 0$, $u = 0.5\, u_c$, $u = 0.99\, u_c$, $u = 1.1\, u_c$ and $u = 1.2\, u_c$. (e-f) Scaled compressive force $F/(Ewd)$ vs. compressive displacement u/ℓ for beams of different width for (e) the experiments (dashed lines) and 3D simulations (solid lines) and (f) the simplified 2D simulations. As the effects of gravity are negligible in the experiments and absent in simulations, the choice of the Young's modulus E is irrelevant and we scale the forces by E.

The plane stress condition, which is nontrivial in finite-strain elasticity, is implemented by requiring that the yy-component [Fig. 2.1(a)] of the true (Cauchy) stress is zero, which necessitates the iterative computation of the deformation gradient component F_{yy} to satisfy this condition [95]. Altogether, these assumptions ensure that more complex 3D and boundary effects can be neglected and allow us to carry out the analysis in the simplest setting where subcritical buckling can be observed, and will be used later to pinpoint the physical mechanism at stake in the post-buckling behaviour of wide beams.

2.2.2 Buckling and Subcritical Buckling

In Fig. 2.1(c-d) we simultaneously display 5 front-view snapshots of experiments and 3D simulations for a beam with $t = 0.23$ ($w = 10.20\,\mathrm{mm}$) at different compressive displacements, which are in very good qualitative agreement. Moreover, we plot the obtained force-displacement curves for the complete range of beam widths in Fig. 2.1(e), which illustrates that 3D simulations and experiments are also in very good quantitative agreement. Hence, the neo-Hookean material model describes the buckling of wide beams well. For all curves, we observe a near-linear increase until the onset of buckling, at which the slope abruptly changes. For thin beams, the force increases after buckling, while for thick beams, the force decreases. For buckling experiments under controlled force of a sufficiently wide beam, the post-buckling branch would thus be unstable and the pitchfork instability would be subcritical. Therefore, we refer to this type of instability as *Subcritical Buckling*. The 2D simulations, albeit considerably simpler, display qualitatively similar behaviour [Fig. 2.1(f)], which demonstrates that subcritical buckling does originate neither from boundary-induced singularities nor from 3D effects. To the best of our knowledge, although subcritical buckling is fairly common in other settings such as the wrinkling instability [96–98] and the wrinkle-to-fold transition [89–91], such sign change is not predicted by any theory as of now for the Euler buckling of wide beams for realistic aspect ratios. Note that Magnusson et al. [42] predicted such transition from supercritical to subcritical post-buckling, yet for overly large aspect ratios (t=0.24), and for which the validity of the extensible, non-shearable elastica is not guaranteed.

We now retrieve the onset of buckling u_c and the post-buckling slope

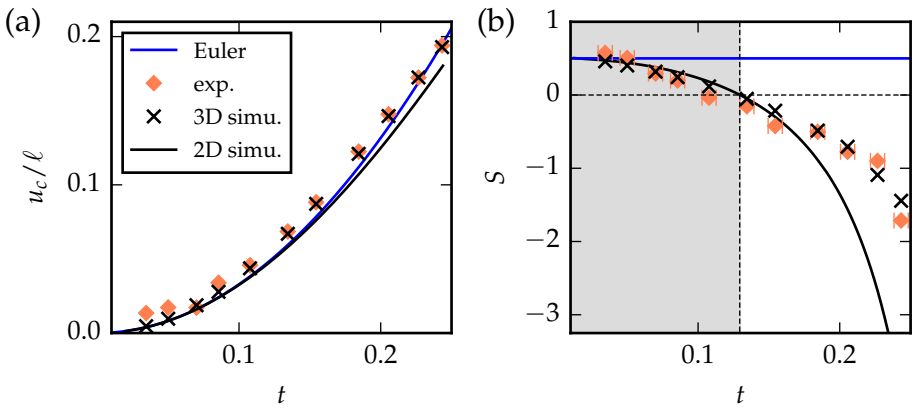

Figure 2.2: Critical compressive displacement and post-buckling slope as function of the beam width-to-length ratio, for Euler's elastica (solid blue), experiments (orange diamonds), 3D FEM simulations (black crosses) and 2D plane stress FEM simulations (solid black). (a) The onset of buckling, u_c, in experiments and simulations qualitatively follows Euler's elastica. (b) The post-buckling slope S in experiments and simulations progressively deviates from the Euler limit $S = 1/2$ for large t. The transition to subcritical buckling ($S < 0$) occurs for $t \gtrsim 0.12$, as indicated by the shaded region.

S, using the relation between the load F and the compressive displacement u in the post-buckling regime:

$$\frac{F - F_c}{F_c} = S\frac{(u - u_c)}{\ell} + \mathcal{O}\left((u - u_c)^2\right), \tag{2.2}$$

with F_c the critical buckling force. In Fig. 2.2(a) we display the onset of buckling as a function of the beam width-to-length ratio t, for the experiments, 3D FEM simulations and the 2D FEM simulations, and observe quantitative agreement with the prediction of Euler's elastica for clamped-clamped boundary conditions, $u_c^{euler}/\ell = t^2\pi^2/3$ [30]. While the onset shows quantitative agreement with Euler's prediction, the results in Fig. 2.2(b) show that the post-buckling slope S strongly deviates from Euler's prediction $S = 1/2$ as t increases, and becomes *negative* for $t \gtrsim 0.12$. Importantly, Fig. 2.2(b) illustrates that subcritical buckling of wide beams is a robust phenomena: Even with the simplifications made in the 2D simulations, the differences in the post-buckling slope between 2D and 3D simulations are modest.

The emergence of subcritical Euler buckling is, as we will show, readily related to nonlinearity in the stress-strain relation [40]. In the following, we will rationalize this behaviour of wide beams—which are 3D structures undergoing large deformations—by constructing a 1D beam model that encompasses such a stress-strain nonlinearity. The behaviour of such a 1D model is more easily tractable than a full tensorial description needed in 3D, and is therefore of significant interest for the design of post-instabilities.

In conclusion, we have shown in this section that, in experiments, in fully 3D numerical simulations, and in 2D simulations, the post-buckling compliance of wide beams varies systematically with the beams aspect ratio t, and becomes negative for $t \gtrsim 0.12$.

Sections 2.3-2.5 provide technical information about the ingredients of our nonlinear 1D beam model. In subsequent order, we review mathematical descriptions of beams, pinpoint and quantify material nonlinearity using extensive 2D simulations and construct a 1D energy density encompassing such nonlinearity. As mentioned before, the reader interested in the main findings of this chapter can continue to section 2.6.

2.3 Mathematical description of beams

In this section we review the basic ingredients and assumptions for 1D beam models of varying degree of sophistication [24, 42, 43]. First, we discuss how 2D deformations of (wide) beams can be mapped onto the deformations of a 1D central beam axis, using the Mindlin-Reissner kinematics [41], which captures the extension, shear and bending of wide beams. Second, we review the governing beam equations that follow from the combination of Mindlin-Reissner kinematics and a linear constitutive law. Third, we numerically solve the most sophisticated linear beam model and compare its outcome to our 2D FEM results in the post-buckling regime. We find that for wide beams, this linear model does not accurately capture the beam shape. These deviations imply that nonlinear corrections to the constitutive law must be taken into account.

2.3.1 Mindlin-Reissner kinematics and strains

We now introduce the Mindlin-Reissner beam kinematics and associated strains that form the basis of our 1D beam description, presented later in this chapter.

The buckling regime of slender beams (elastic lines, $t \to 0$) is bending dominated. Therefore, their shape can be described by a single kinematic field, denoted $\theta(s)$ [Fig. 2.3(a)], which is the rotation angle with respect to the z-axis as a function of the curvilinear coordinate s along the beam [99]. Wide beams, however, have additional modes of deformation, which are dominantly compressive and shear deformations. Following [41, 43, 100], the shape of such beams can be captured by a central beam axis described by a deflection and shear angle, respectively defined as $\theta(s)$ and $\chi(s)$, along with the stretch $\lambda(s)$ [Fig. 2.3(c)]. We refer to this kinematic description as *Mindlin-Reissner kinematics*. The stretch along the central axis is defined as the elongation of a beam element of length ds in the undeformed state, with respect to the same element in the deformed state of length ds', that is, $\lambda(s) = ds'/ds$. Furthermore, the sum of the rotation angle and shear angle, $\theta(s) + \chi(s)$, is defined as the angle enclosed by the vertical vector $\mathbf{e_z}$ and the tangent to the central axis, $\mathbf{t}$. The shear angle can be regarded as the angle enclosed within the normal of the central axis, $\mathbf{n}$, and the tangent to the deformed cross-section in the vicinity of the central axis, $\mathbf{n}'$ [zoomed area in Fig. 2.3(c)]. The rotation angle can then readily follows from the difference between the sum $\theta(s) + \chi(s)$, and $\chi(s)$ itself. Following [41], the Mindlin-Reissner kinematics can be used to introduce a set of compressive, bending, and shear strains, respectively denoted $\tilde{\varepsilon}_0$, ε_1 and γ_0, and defined as

$$\tilde{\varepsilon}_0 = \lambda \cos(\chi) - 1, \tag{2.3}$$

$$\varepsilon_1 = \theta_s, \tag{2.4}$$

$$\gamma_0 = \lambda \sin(\chi). \tag{2.5}$$

In the reminder of this chapter, we refer to this set of strain-displacement relations as the *Mindlin-Reissner strains*. In order to obtain a set of closed beam equations, these strains should be related to stresses via constitutive relations. In the following section we review prior (wide) beam models that are constructed from a combination of Mindlin-Reissner strains and linear elasticity.

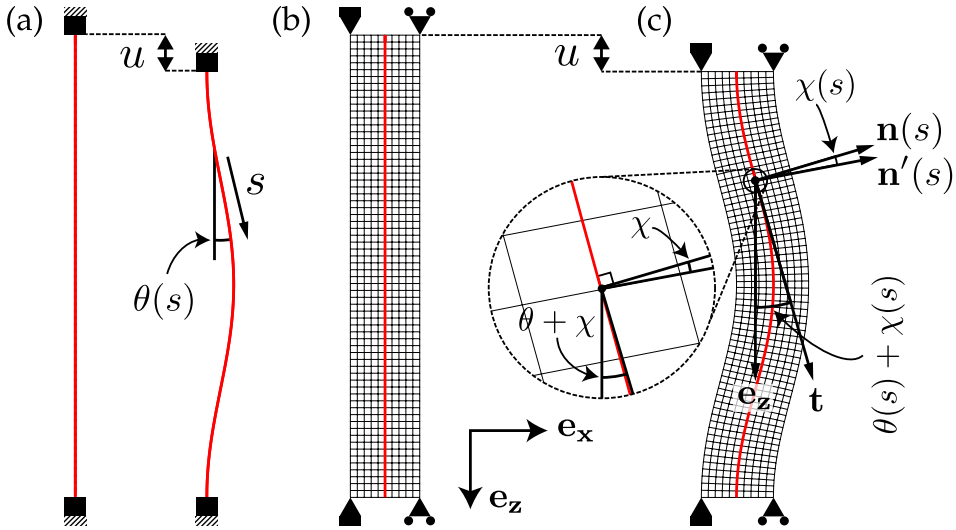

Figure 2.3: Kinematic description of a slender ($t = 0^+$) and wide beam (here, $t = 0.15$). Both beams are compressed equally by a displacement u. (a) The shape of an undeformed (left) and buckled (right) slender beam. We obtain the buckled state by solving Euler's elastica [Eq. (2.6)] for clamped boundary conditions at both ends. The kinematic description of a slender beam is governed by the rotation angle $\theta(s)$. (b) Snapshot from a 2D simulation of a wide neo-Hookean beam in its undeformed state, where each square represents a simulation element. We impose clamped boundary conditions at both ends of the beam, but allow free lateral expansion along the x-direction at top and bottom boundaries. The superimposed, red, solid line depicts the central axis of the beam as obtained from FEM simulations accordingly. (c) Snapshot from the same simulation as in (b), depicting the beam in its deformed state. The deflection of the central axis under a compressive displacement u is described by a combination of the rotation angle, $\theta(s)$, and shear angle, $\chi(s)$ along the curvilinear coordinate of the beam as indicated. For a precise definition of $\theta(s)$ and $\chi(s)$ as well as the vectors $\mathbf{n}(\mathbf{s})$, $\mathbf{n}'(\mathbf{s})$ and $\mathbf{t}(\mathbf{s})$, see the main text.

2.3.2 Linear beam models

Here we present a number of existing models that combine the Mindlin-Reissner strains with conventional *linear* elasticity. We start with a brief review of the bending of elastic lines (Euler's elastica), followed by more complete models that include extensibility and shear effects [42, 43].

Euler's limit— Slender beams can be described through a single Mindlin-Reissner strain, θ_s. The governing beam equation to be satisfied by the bending strain then reads [30]:

$$EI\theta_{ss} + F\sin\theta = 0, \tag{2.6}$$

where I is the second moment of area, which equals $I = \frac{1}{12}w^3 d$ in case of the rectangular cross-section of width w and depth d considered here. The above equation is formally known as Euler's elastica and can be solved analytically to provide an exact prediction for the critical buckling force [99].

Euler's elastica rests on two assumptions, which are of importance as they help us to understand where wide beams start to deviate from slender beams. First, within the reference frame defined in Fig. 2.3(b), the elastica tacitly assumes that the axial nominal strain ε_{zz} across the beam is given by

$$\varepsilon_{zz}(x) = \varepsilon_1 x, \tag{2.7}$$

where x is the horizontal coordinate across the beam section and ε_1 is the curvature of the central axis of the beam, as defined by Eq. (2.4). Second, it assumes a linear constitutive relation between the axial nominal stress σ_{zz} and axial nominal strain, that is,

$$\sigma_{zz} = E\varepsilon_{zz}. \tag{2.8}$$

This assumption of linear elasticity is common regarding slender beams and provides an excellent description of their buckling properties, because the typical strains involved in slender beam buckling are much smaller than unity, $u_c/\ell \ll 1$.

Shearable and extensible beams — Wide beams necessitate the use of all three Mindlin-Reissner strains due to additional compressive and shear deformations. Consequently, the governing beam equations now constitute a set of three coupled equations, rather than a single equation in the case of slender beams. Since the strains involved in wide beam buckling can be substantial (*e.g.* $\sim 10\%$ for a beam with $t = 0.17$), nonlinearities in the stress-strain relation induced by large deformations become significant. Nonetheless, as a first step, recent work [43] has combined all

three Mindlin-Reissner strains with linear elasticity,

$$EI\theta_{ss} + F\left((1+\tilde{\varepsilon}_0)\sin\theta + \gamma\cos\theta\right) = 0, \tag{2.9a}$$

$$EA\tilde{\varepsilon}_0 + F\cos\theta = 0, \tag{2.9b}$$

$$GA\gamma + F\sin\theta = 0, \tag{2.9c}$$

where, $A = wd$ is the cross-sectional area. In the remainder of this manuscript we refer to the above set of equations as the *linear beam model*. Note that previous work also considered beam models that take into account exclusively bending and shear [100, 101] deformations, known as Timoshenko beams, or solely bending and extensibility [42].

As we will show later in section 2.6, the linear beam model somewhat improves the post-buckling description in comparison to Euler's elastica ($S = 1/2$), but fails to predict the experimentally and numerically observed subcritical buckling. Specifically, in the following section we illustrate that the strains predicted by the *linear* elastic beam model significantly deviate from the strains obtained by the 2D FEM simulations, already for a beam of width-to-length ratio $t = 0.1$. This evidences that the Mindlin-Reissner strains given by Eqs. (2.3-2.5) —which remain valid for large strains [85]— cannot be accurately determined from a closed set of beam equations based on linear elasticity. Instead, to accurately predict the post-buckling slope and Mindlin-Reissner strains from a set of beam equations, one needs to develop a model that takes into account a nonlinear stress-strain relation, which is the main objective of this chapter.

2.3.3 Linear wide beam model compared to 2D FEM simulations

We now compare the Mindlin-Reissner strains predicted by the linear beam model [Eqs. (2.9)] to our results obtained from the 2D FEM simulations (Fig. 2.4). Using a shooting method in *Mathematica*, we solve numerically the linear beam model, with boundary conditions $\theta(0) = 0$ and $\theta_s(0) = \theta_s(1) = C$, where C is a constant directly set by the amount of uniaxial displacement u. Comparing the results from FEM simulations (solid black lines) in Fig. 2.4(a-c) with those of the linear beam model, we observe a qualitative agreement for bending and shear deformations. However, there is a very striking difference between the model predictions and numerical results for the compressive deformations [Fig. 2.4(a)]:

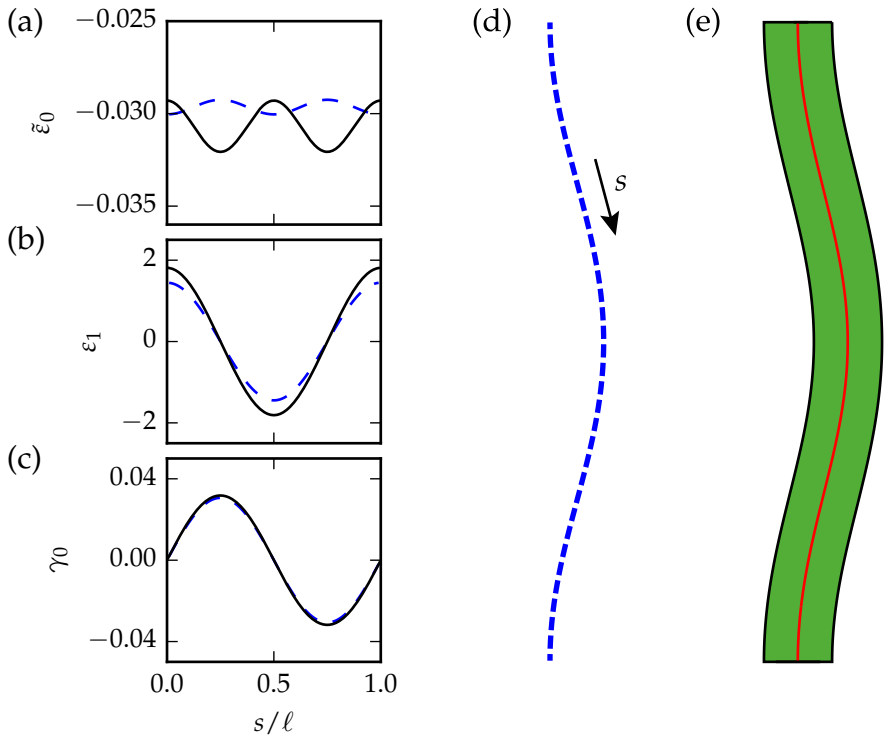

Figure 2.4: Mindlin-Reissner strains and corresponding beam shapes for a beam ($t = 0.1$) which is uniaxially compressed to a displacement of $u/u_c = 1.3$. (a-c) The solid black curves depict data for the Mindlin-Reissner strains obtained from FEM simulations, and the blue dashed curves are numerical solutions of the linear elastic wide beam model [Eqs. (2.9)]. As a function of the curvilinear coordinate s, we show (a) the compressive strain, (b) the bending strain, and (c) the shear strain. (d) Shape of the central axis as predicted by the linear beam model. We have obtained this shape by the integration of the horizontal and vertical component of the displacement gradient with respect to s, respectively given by $\lambda\cos(\theta+\chi)$ and $\lambda\sin(\theta+\chi)$ [41]. (e) Beam shape and associated central axis (solid red) obtained from 2D FEM simulations.

the actual (numerical) modulations of the stretch are much stronger, and incidentally are opposite, to those predicted by the model. Subtle as this deviation may be, the linear beam model cannot predict the experimentally and numerically subcritical buckling (see section 2.6). This suggests that this subtle deviation points to a more fundamental flaw of the linear

model, which arises due to the large deformations that are unavoidable in wide-beam buckling. In the following sections we will uncover, clarify and model the role of nonlinearity in the constitutive equation as the crucial ingredient to describe the post-buckling regime of wide beams.

2.4 Quantifying the role of material nonlinearity

In this section we use FEM simulations to disentangle nonlinearities in the relation between nominal stress and strain. We focus on a transversal slice across the middle of the beam, obtain the stress and strain profiles for slender and for wide beams, both close to and deep into the post-buckling regime. These profiles unambiguously show that, for thick beams, axial stresses and strains are no longer linearly related, but that rather a neo-Hookean description, where the stress is a nonlinear function of strain, describes the data with high accuracy, for beam aspect ratios up to $t \approx 0.2$ and for compressions up to 115% of the critical compression where buckling takes place. We then quantify these axial nonlinearities by a systematic powerlaw expansion of the nominal strain and stress as function of the lateral coordinate, thickness and compression. The leading order terms in this expansion are consistent with Euler's Elastica, but it is not a-priori clear what the structure of the higher order terms is. We therefore use our FEM data to determine the leading order terms in this expansion. This numerical input circumvents the need for heuristics to guess the important terms, and leads to a greatly simplified model where the dominant next order terms in t are properly taken into account. As we will show, these next order terms evidence a nonlinearity in the stress-strain relation which is consistent with the material nonlinearity of neo-Hookean materials [52]. Finally, we repeat the above analysis for the nominal shear strain and stress and show that shear strain and stress can be related linearly. Hence, the crucial main missing ingredient in the linear elastic wide beam model is nonlinearity in the axial nominal strain and stress relation.

2.4.1 Nonlinear uniaxial transverse stress and strain profiles

We start by considering the shape of the transverse profiles of the axial nominal strain, ε_{zz}, and stress, σ_{zz}. We restrict our attention to the cross-

section at the middle of the beam, depicted by the horizontal red lines in Fig. 2.5(a-b). We found (not shown) that the discrepancy between the observed and predicted sinusoidal modulation of $\tilde{\varepsilon}_0$, identified in Fig. 2.4(a), is maximal at the middle of the beam in the immediate post-buckling regime. We then consider $\varepsilon(x) \equiv \varepsilon_{zz}(x, s = \ell/2)$ and $\sigma(x) \equiv \sigma_{zz}(x, s = \ell/2)$ to measure the spatial shape of the axial nominal strain and stress as a function of the transverse coordinate, x, of the deformed geometry.

In the pre-buckling regime, the uniaxial nominal stresses and strains are simply constants as function of x as the beam undergoes uniform uniaxial compression. Under uniaxial uniform compression the neo-Hookean relation predicts the following nominal stress-strain relation (see appendix 2.B.1)

$$\sigma_{nH}(x) = \frac{E}{3}\left(1 + \varepsilon - \frac{1}{(1+\varepsilon)^2}\right). \tag{2.10a}$$

The nonlinearity of this stress-strain relation stems from the combination of large deformations and incompressibility. This nonlinearity can qualitatively be understood from the fact that upon compression (tension) the cross-sectional area increases (decreases) and the stress-strain curve is therefore effectively stiffening (softening). The above equation can be expanded for small strain, ε, as

$$\sigma_{nH}(x) = E\left(\varepsilon - \varepsilon^2\right) + \mathcal{O}(\varepsilon^3). \tag{2.10b}$$

Hence, the linear term is consistent with Hookean elasticity and the leading nonlinear term is quadratic.

In contrast to the uniform uniaxial deformations considered above, buckled beams experience non-uniform deformations, and spatially varying stress and strain fields. Therefore we focus in the following on the evolution of the stress and strain profiles as the excess displacement Δu in the post-buckling regime is increased. In Fig. 2.5 we have plotted the nominal stress rescaled by the Young's modulus (solid black) and nominal strain profiles (dashed red) as function of x in the post-buckling regime, for a slender $(t = 0.01)$ and wide $(t = 0.15)$ beam.

For slender beams, the strains remain sufficiently small for the linear stress-strain relation to be valid. First, in Fig. 2.5(c) we demonstrate that the slender beam at small excess displacement has linear nominal stress

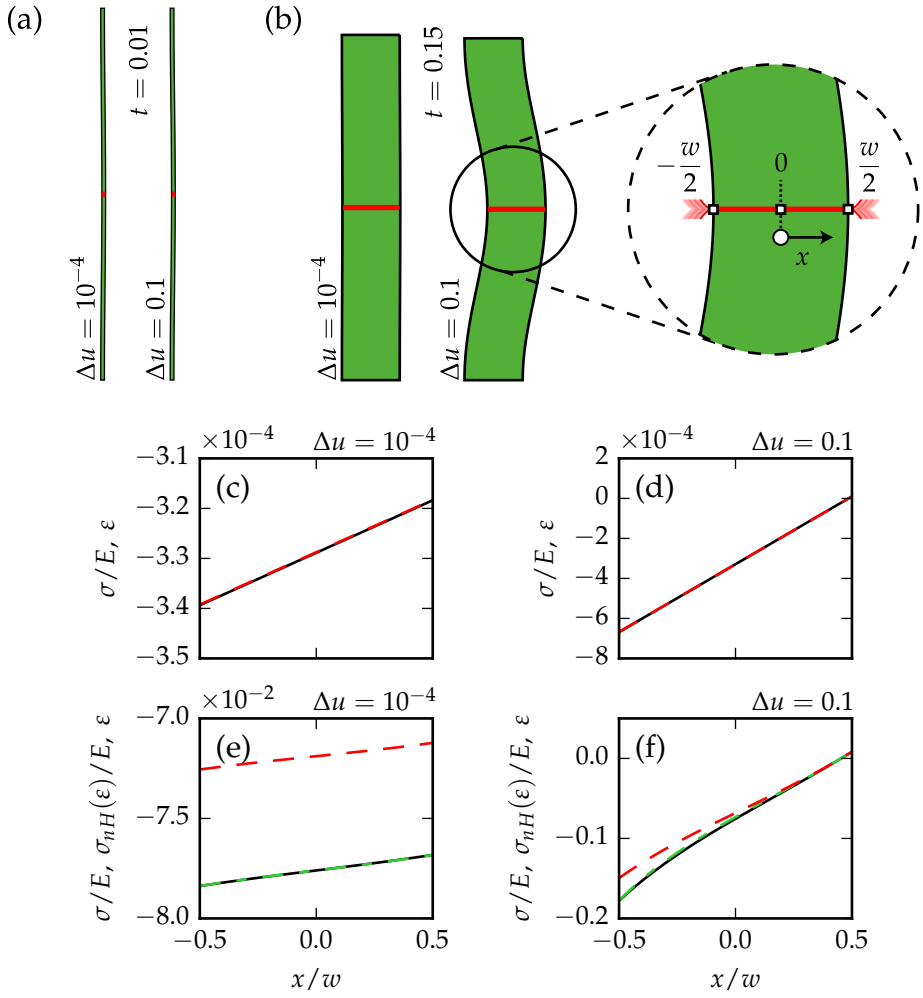

Figure 2.5: Beam shapes, stress-strain relation and stress and strain profiles. (a-b) Beam shapes for (a) a slender $(t = 0.01)$ and (b) wide $(t = 0.15)$ beam at excess strains of $\Delta u = 1 \times 10^{-4}$ and $\Delta u = 0.1$. We track the nominal stress and strain profiles as a function of the transverse coordinate x at the central cross section of the beam, depicted by the horizontal red lines. (c-d) Rescaled uniaxial nominal stress (solid black) and strain (dashed red) profiles for a slender beam $(t = 0.01)$ at an excess strain of (c) $\Delta u = 1 \times 10^{-4}$ and (d) $\Delta u = 0.1$. (e-f) Rescaled uniaxial nominal stress and strain profiles for a wide beam $(t = 0.15)$ at an excess strain of (e) $\Delta u = 1 \times 10^{-4}$ and (f) $\Delta u = 0.1$. The green dash-dotted lines correspond to $\sigma_{\mathrm{nH}}(\varepsilon)/E$, obtained by applying the neo-Hookean stress-strain relation in Eq. (2.10a) to the strain profile obtained from FEM simulations.

and strain profiles across the beam, and that $\sigma/E = \varepsilon$ is a very good approximation. In panel (d) we show data for $\Delta u = 0.1$, which results in a larger average nominal strain and a larger range of nominal strains across the beam, but the profiles remain linear and $\sigma/E \approx \varepsilon$. Both panel (c) and (d) show that the nominal strains involved in slender beam buckling remain sufficiently small for the nominal stress and strain to be simply proportional, as $\sigma = E\varepsilon$. Hence, the stress-strain nonlinearity is negligible for slender beams, both at small (panel c) and larger (panel d) excess displacement.

In contrast to slender beams, nonlinearities become important for thick beams. In Fig. 2.5(e-f) we have plotted the nominal stress and strain profiles for a wide beam $(t = 0.15)$ at $\Delta u = 1 \times 10^{-4}$ and $\Delta u = 0.1$. For small excess displacement, $\Delta u = 1 \times 10^{-4}$, the nominal stress and strain profiles are both linear, but $\sigma/E \neq \varepsilon$. This is because the strains involved are sufficiently large for the neo-Hookean nonlinearity to become important. Indeed, when calculating $\sigma_{\mathrm{nH}}(\varepsilon)$ from Eq. (2.10a), using the numerically obtained strain profile, we find that this stress describes the data extremely well (green dash-dotted curve). For larger excess displacement $(\Delta u = 0.1)$, the effect of the nonlinearity is even more pronounced. We note that here a large range of strain occurs, and that the stress profile becomes strongly nonlinear in x. Again, using the nonlinear stress-strain relation in Eq. (2.10a), $\sigma_{\mathrm{nH}}(\varepsilon)$ describes the numerical stress data very accurately. Taken together, our FEM data provides strong evidence that to correctly describe the stresses in thick beams in the post-buckling regime, including the neo-Hookean correction is necessary and sufficient.

2.4.2 Series expansion of the axial nominal stress and strain

In this section we perform a systematic polynomial expansion of the nominal stress and strain profiles in x/w, t and Δu, and determine all prefactors and scaling exponents using our FEM results. Our findings are consistent with the Euler limit at lowest order in t (quadratic) and confirm that stress and strain are nonlinearly related for higher order in t (quartic and higher).

Polynomial expansion and asymptotic analysis

As described above, the data in Fig. 2.5 suggests that the nominal stress and strain profiles are linear in x for (i) small t or (ii) small Δu, but become nonlinear when t and Δu are large. It is then natural to expand the nominal strain and stress around the buckling strain and stress, respectively denoted ε_b and σ_b, as function of the (scaled) transverse coordinate x/w:

$$\varepsilon\left(t, \Delta u, \frac{x}{w}\right) - \varepsilon_b = \sum_{n=0} C_n\left(t, \Delta u\right)\left(\frac{x}{w}\right)^n, \tag{2.11a}$$

and

$$\frac{\sigma - \sigma_b}{E}\left(t, \Delta u, \frac{x}{w}\right) = \sum_{n=0} D_n\left(t, \Delta u\right)\left(\frac{x}{w}\right)^n, \tag{2.11b}$$

where C_n and D_n are the coefficients of the expansion in x/w of order n. In the remainder of this manuscript, we will refer to these coefficients as the *post-buckling profile coefficients.* At buckling ($\Delta u = 0$), $C_n = D_n = 0$, so it is natural to assume that the post-buckling profile coefficients C_n and D_n grow as power laws in t and Δu in the post-buckling regime. Therefore, we postulate:

$$C_n\left(t, \Delta u\right) = \bar{C}_n t^{\alpha_n} \Delta u^{\beta_n}, \tag{2.12a}$$

and

$$D_n\left(t, \Delta u\right) = \bar{D}_n t^{\rho_n} \Delta u^{\tau_n}. \tag{2.12b}$$

Here, α_n, β_n, ρ_n and τ_n are *post-buckling profile scaling exponents* and $\bar{C}_n$ and $\bar{D}_n$ are the *post-buckling profile prefactors* which we will now determine up to the order $n = 5$ from our numerical simulations. Because of the nature of the Euler buckling instability, we expect that the exponents β_n and τ_n for all value of n will be half integers. Furthermore, as nominal stress and strain are linearly related in lowest order, stress and strain expansions should have the same post-buckling profile scaling exponents with t and Δu for every order, that is $\alpha_n = \rho_n$ and $\beta_n = \tau_n$. We also notice that the order $n = 1$ corresponds to the post-buckling stress and strain profiles of Euler's elastica, for which the post-buckling profile coefficients C_1 and D_1

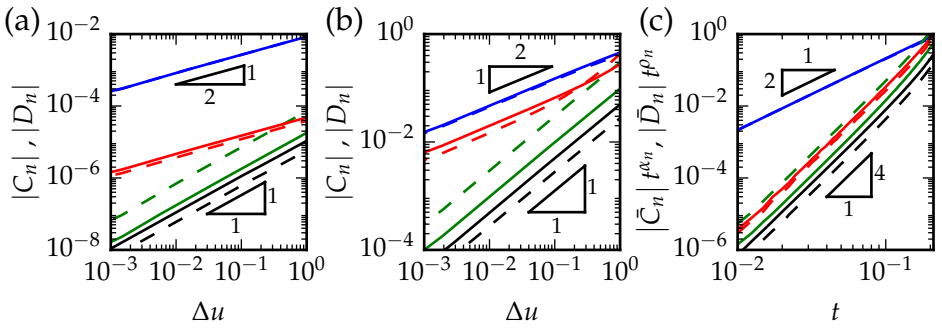

Figure 2.6: Expansion of the nominal strain and stress profiles obtained by FEM simulations, according to Eqs. (2.11-2.12). We plot the post-buckling profile coefficients C_n and D_n in each order as a function of Δu and t. In black, blue, green and red we have plotted C_n (solid lines) and D_n (dashed lines), corresponding to the order $n = 0$, $n = 1$, $n = 2$ and $n = 3$ respectively. (a-b) We have plotted $|C_n|$ and $|D_n|$ as function of Δu for a (a) slender beam ($t = 0.02$) and (b) thick beam ($t = 0.15$). (c) Dependence of C_n and D_n on the beam's aspect ratio t.

can be calculated analytically; below we find that the numerical results for C_1 and D_1 are consistent with their analytical predictions.

To determine all the constants, we use the numerical protocol described in section 2.2.1 and perform $N = 10^2$ simulations for beams with a logarithmically spaced width-to-length ratio in the range from $t = 0.01$ up to $t = 0.25$, and with an excess strain that is increased from $\Delta u = 10^{-3}$ up to $\Delta u = 1$ in 3×10^2 subsequent steps. For each simulation we extract the spatial shape of the nominal stress and strain as function of x/w across the middle of the beam at $s = \ell/2$ and fit $\varepsilon(x)$ and $\sigma(x)/E$ to polynomials of order $n = 5$, by which we obtain the post-buckling profile coefficients $C_n(t, \Delta u)$ and $D_n(t, \Delta u)$ for each specific set of parameter values t and Δu.

One subtle point is that such powerlaw fits are very sensitive to the determination of the point $\Delta u = 0$. To accurately determine Δu, we need an accurate measurement of the critical displacement u_c, as Δu and u_c are related through $\Delta u = u/u_c - 1$. The numerical estimation, u_c^n, determined in FEM simulations through the nonlinear buckling analysis, typically has a relative error of 10^{-3} which is not sufficient when considering the scaling near the critical point. Therefore, we correct $u_c = u_c^n - 1 + \delta$, where the correction δ ensures an increased accuracy for Δu. For each beam we have determined δ from fitting Eq. (2.13a) to our numerical data for C_1.

We choose $n = 1$ to determine Δu, because the linear order is the most pronounced (Fig. 2.6) and therefore gives the most accurate measurement of δ. Having determined δ for $n = 1$, we subsequently fix δ to the same value for $n = 0,2,3,4,5$.

Scaling of the coefficients C_n and D_n with Δu

In this section we describe the scaling of the post-buckling profile coefficients C_n and D_n with Δu for fixed t, i.e., we determine the post-buckling profile exponents β_n and τ_n. In Fig. 2.6(a-b) we plot the coefficients C_n and D_n as function of Δu, for fixed t. In panel (a) and (b) we show results for a slender ($t = 0.02$) and wide ($t = 0.15$) beam, respectively. To uncover power law behaviour for Δu in C_n and D_n we use a log-log scale and then plot $|C_n(\Delta u)|$ (solid lines) and $|D_n(\Delta u)|$ (dashed lines). Note that both panels show results up to $n = 3$ — for higher order terms the scaling exponents and prefactors are provided in Tables (2.1-2.2)). From the straight lines on the log-log scale in Fig. 2.6(a-b) it becomes apparent that C_n and D_n show power law behaviour in Δu as was postulated already in Eqs. (2.12).

Fitting protocol — To determine the post-buckling profile scaling exponents, β_n and τ_n, we first take the absolute sign and log on both sides of Eqs. (2.12) which yields

$$\log(|C_n|) = \beta_n \log(\Delta u) + \log\left[\left|\bar{C}_n\right| t^{\alpha_n}\right], \tag{2.13a}$$

and

$$\log(|D_n|) = \tau_n \log(\Delta u) + \log\left[|\bar{D}_n|\, t^{\rho_n}\right], \tag{2.13b}$$

and then fit our numerical data for the post-buckling profile coefficients C_n and D_n to their respective equations as given directly above. We have tabulated the scaling exponents β_n and τ_n in Table 2.1 up to $n = 5$.

Results — With a fitting range for Δu in $[10^{-3}, 10^{-1}]$ at fixed t, we measure identical exponents for nominal stress and strain within their error bars: $\beta_0 = \tau_0 \approx 1.0$ [black lines in Fig. 2.6(a-b)], $\beta_1 = \tau_1 \approx 0.5$ (blue lines), $\beta_2 = \tau_2 \approx 1.0$ (red lines), and $\beta_3 = \tau_3 \approx 0.5$ (green lines). This is consistent with our earlier assertion that these exponents can be expected

	Δu		t	
n	β_n	τ_n	α_n	ρ_n
0	1.03 ± 0.1	1.05 ± 0.1	4.06 ± 0.4	4.09 ± 0.4
1	$0.51 \pm 0.03\,[\frac{1}{2}]$	$0.51 \pm 0.03\,[\frac{1}{2}]$	$2.00 \pm 0.1\,[2]$	$1.99 \pm 0.1\,[2]$
2	1.03 ± 0.1	1.02 ± 0.1	4.02 ± 0.4	4.00 ± 0.4
3	0.51 ± 0.05	0.51 ± 0.05	4.00 ± 0.4	3.99 ± 0.4
4	1.0 ± 0.15	1.01 ± 0.15	6.05 ± 0.9	6.00 ± 0.9
5	0.51 ± 0.15	0.52 ± 0.16	6.20 ± 1.9	5.82 ± 1.7

Table 2.1: Post-buckling profile scaling exponents of Δu and t, for the expansion of the nominal strain and stress profiles as defined in Eqs. (2.11-2.12). Each row corresponds to a different order of n and values within the square brackets represent analytical results as predicted by Euler's elastica. The error in the relevant scaling exponents is an estimation which we assign to a combination of uncertainties: (i) The error in Δu, which is particularly important for the scaling near the critical point; (ii) The finite range of Δu and t over which the scaling holds is at most 2 decades; (iii) The quantities $\bar{C}_n t^{\alpha_n}$ and $\bar{D}_n t^{\alpha_n}$, necessary to determine the scaling exponents for t, are obtained by extrapolating C_n and D_n to $\Delta u = 1$ [Eqs. (2.13)], hence this error propagates when determining the scaling exponents for t. Taking all effects into account, we estimate an fitting error of 5% for $n = 1$, 10% for $n = 0,2,3$, 15% for $n = 4$ and 30% for $n = 5$.

to be half-integers, and we will now assume they are. As we will further discuss in the following, while the $n = 1$ term dominates for slender beams [Fig. 2.6(a)] and corresponds to Euler's elastica, other orders $n \neq 1$ become significant for wider beams [Fig. 2.6(b)].

Scaling of the coefficients C_n and D_n with t

The next step is to determine how the post-buckling profile coefficients C_n and D_n scale with the beam's aspect ratio t, hence determining the post-buckling profile exponents α_n and ρ_n.

Fitting protocol — The first step is to refine the fit of Eqs. (2.13) to our numerical data for C_n and D_n. To do so, we fix the post-buckling profile exponents β_n and τ_n to their nearest half integer values, which results in alternating exponents 1 or 1/2: $\beta_0 = \tau_0 = 1$, $\beta_1 = \tau_1 = 1/2$, $\beta_2 = \tau_2 = 1$,

and so on. This procedure reduces the number of fitting parameters and thus provides a more accurate measure of the constants $\log[\bar{C}_n t^{\alpha_n}]$ and $\log[\bar{D}_n t^{\rho_n}]$, where t is held fixed in this fitting procedure. By repeating this analysis for t in the range $[10^{-2}, 0.25]$, we determine the constants $\bar{C}_n t^{\alpha_n}$ and $\bar{D}_n t^{\rho_n}$ for each t and plot them versus t on a log-log scale in Fig. 2.6(c). Obviously, the straight lines in Fig. 2.6(c) on the log-log scale suggest that C_n and D_n show power law behaviour in t as well. Fitting this data to

$$\log\left(\left|\bar{C}_n\right| t^{\alpha_n}\right) = \log\left(\left|\bar{C}_n\right|\right) + \alpha_n \log(t), \tag{2.14a}$$

and

$$\log\left(\left|\bar{D}_n\right| t^{\rho_n}\right) = \log\left(\left|\bar{D}_n\right|\right) + \rho_n \log(t), \tag{2.14b}$$

with t in the range $[10^{-2}, 10^{-1}]$. An overview of the scaling exponents α_n and τ_n up to order $n = 5$ is provided in Table 2.1.

Results — We measure identical post-buckling profile exponents for stress and strain within their error bars: $\alpha_0 = \rho_0 \approx 4.0$ (black lines), $\alpha_1 = \rho_1 \approx 2.0$ (blue lines), $\alpha_2 = \rho_2 \approx 4.0$ (red lines), $\alpha_3 = \rho_3 \approx 4.0$ (green lines). Similarly to the exponents of Δu, we find correspondence for the exponents of t with Euler's elastica for $n = 1$, and identical exponents for stress and strain, i.e., $\alpha_n = \rho_n$—moreover, all numerical values for the exponents are consistent with half integers. In the remainder of this manuscript, we will fix the exponents α_n and ρ_n to their nearest integer values: $\alpha_1 = \rho_1 = 4$, $\alpha_1 = \rho_1 = 2$, $\alpha_2 = \rho_2 = 4$, and so on.

So far, we have determined the scaling exponents β_n, τ_n, α_n and ρ_n, but the post-buckling profile prefactors $\bar{C}_n$ and $\bar{D}_n$ remain to be determined. In fact, they simply follow from the fit of the data in Fig. 2.6(c) to Eqs. (2.14). For the most accurate determination of the prefactors, however, we refine our fit by using the fixed exponents α_n and ρ_n, and subsequently redo the fit. In Table 2.2 a summary of the prefactors $\bar{C}_n$ and $\bar{D}_n$, as well as their ratios are given. Note that for the order $n = 1$, such values are in good agreement with those predicted by Euler's elastica for clamped-clamped boundary conditions.

n	$\bar{C}_n$	$\bar{D}_n$	$\bar{C}_n/\bar{D}_n$
0	72.0 ± 25	38.3 ± 13	1.88 ± 0.9
1	21.3 ± 3.2 $\left[\frac{4\pi^2}{\sqrt{3}} \approx 22.8\right]$	21.1 ± 3.2 $\left[\frac{4\pi^2}{\sqrt{3}} \approx 22.8\right]$	$1.01 \pm 0.2\,[1]$
2	-116 ± 41	-553 ± 194	0.21 ± 0.1
3	320 ± 112	254.9 ± 89	1.26 ± 0.6
4	$-6.1 \cdot 10^3 \pm 2.4 \cdot 10^3$	$-1.4 \cdot 10^4 \pm 5.6 \cdot 10^3$	0.42 ± 0.2
5	$1.1 \cdot 10^4 \pm 5.5 \cdot 10^3$	$1.2 \cdot 10^4 \pm 6 \cdot 10^3$	0.99 ± 0.7

Table 2.2: Post-buckling profile prefactors $\bar{C}_n$ and $\bar{D}_n$ and their ratio, for the expansion of the nominal strain and stress profiles as defined by Eq. (2.11-2.12). Each row corresponds to a different order of n and values within the square brackets represent analytical results, predicted by Euler's elastica for clamped-clamped boundary conditions. The errors in the prefactors are an estimation, similar to the estimate made in Table 2.1. Here, however, the errors are larger than for the post-buckling profile exponents, because C_n and D_n follow from extrapolating our data up to $t = 1$ [Eqs. (2.14)]. Therefore, we estimate an error of 15% for $n = 1$, 35% for $n = 0,2,3$, 40% for $n = 4$ and 50% for $n = 5$.

Discussion

We have quantified how the nominal stress and strain profiles arise beyond buckling and observed intricate powerlaw scaling with the transversal coordinate x/w, beam width-to-length ratio t and post-buckling strain Δu:

$$\varepsilon\left(t, \Delta u, \frac{x}{w}\right) - \varepsilon_b = \sum_{n=0} \bar{C}_n t^{\alpha_n} \Delta u^{\beta_n} \left(\frac{x}{w}\right)^n, \tag{2.15a}$$

and

$$\frac{\sigma - \sigma_b}{E}\left(t, \Delta u, \frac{x}{w}\right) = \sum_{n=0} \bar{D}_n t^{\rho_n} \Delta u^{\tau_n} \left(\frac{x}{w}\right)^n. \tag{2.15b}$$

Our results in Table 2.1 indeed confirm that stress and strain share the same exponents in every order n, both in Δu and t. On the one hand, the scaling exponents for Δu of the nominal stress and strain equal 1 for even n, and $1/2$ for odd n. On the other hand, the scaling exponents for t show that the linear order $(n = 1)$ carries the lowest exponent in t, namely $\alpha_1 = \tau_1 = 2$, while the zeroth, quadratic and cubic order $(n = 0,2,3)$ carry

a scaling exponent in t which equals 4 and the quartic and quintic orders ($n = 4,5$) carry a higher scaling exponent in t of 6. We discuss further below how our results establish in detail the nonlinear corrections of the stress and strain profiles beyond the Euler limit.

Euler's limit, $O(t^2)$ **—** The dominant term of the asymptotic expansion given by Eqs. (2.15) is quadratic in t and corresponds to linear stress and strain profiles ($n = 1$, see Table 2.1), whereby the Euler's limit introduced in section 2.3.2 is recovered. This is further confirmed by the quantitative agreement between the measured and theoretical values of the post-buckling profile exponents and prefactors, that is, $\beta_1 \approx \tau_1 \approx 1/2$, $\alpha_1 \approx \rho_1 \approx 1/2$ [30] and $\bar{C}_1 \approx \bar{D}_1 \approx 4\pi^2/\sqrt{3}$. Note that as $\bar{C}_1/\bar{D}_1 \approx 1$, stress and strain are linearly related for $n = 1$, which confirms that linear elasticity is a correct approximation within Euler's limit.

Leading order nonlinear correction, $O(t^4)$ **—** The next contribution to Eqs. (2.15) is quartic in t and contains the zeroth, quadratic and cubic corrections in x/w to the stress and strain profiles ($n = 0,2,3$). A closer inspection of Table 2.2 reveals that, in contrast to $n = 1$, the post-buckling profile prefactors $\bar{C}_n$ and $\bar{D}_n$ are different. Because a linear constitutive relation would imply that Eq. (2.15a) and Eq. (2.15b) are equal, hence would have equal prefactors $\bar{C}_n$ and $\bar{D}_n$, such a difference between the prefactors again evidences a nonlinear relation between stress and strain.

Next orders and convergence of the series expansion, $O(t^6)$ **—** Finally, we have carried out the fitting procedure up to sixth order in t and find that it involves the order $n = 4$ and $n = 5$ corrections in the stress and strain profiles. We have checked that for realistic values of beam width-to-length ratio ($t = 0.15$), these corrections are of relative magnitude $\lesssim 2\%$ and thus can be neglected. Therefore, in the remainder of the analysis we will neglect the orders $n \geq 4$, in other words, assume that the stress and strain profiles are accurately described by cubic polynomials.

2.4.3 Effective stress-strain law for the axial component

Above we argued that the difference between $\bar{C}_n$ and $\bar{D}_n$ evidences nonlinearity in the stress-strain relation. In this section we set up the appro-

priate nonlinear stress-strain relation. Because the post-buckling slope [Eq. (2.2)] is defined in the vicinity of the buckling point, the starting point is to write a Taylor series for the normal stress around the buckling strain ε_b up to quadratic order, which yields

$$\sigma = \sigma_b + \left.\frac{\partial \sigma}{\partial \varepsilon}\right|_{\varepsilon=\varepsilon_b} (\varepsilon - \varepsilon_b) + \frac{1}{2} \left.\frac{\partial^2 \sigma}{\partial \varepsilon^2}\right|_{\varepsilon=\varepsilon_b} (\varepsilon - \varepsilon_b)^2 + \mathcal{O}(\varepsilon - \varepsilon_b)^3 . \tag{2.16}$$

Defining the slope of the stress-strain curve at ε_b as an effective Young's modulus E_b, and the nonlinearity η as $\frac{1}{2}\left(\partial^2\sigma/\partial\varepsilon^2\right)$, Eq. (2.16) can be written more compactly as

$$\frac{\sigma - \sigma_b}{E_b} = (\varepsilon - \varepsilon_b) + \eta (\varepsilon - \varepsilon_b)^2 + \mathcal{O}(\varepsilon - \varepsilon_b)^3 . \tag{2.17}$$

We can calculate E_b and η analytically by evaluating the expansion in Eq. (2.16) using the stress-strain relation for uniaxially compressed neo-Hookean materials [Eq. (2.10a)]. This yields:

$$E_b(\varepsilon_b) = \frac{E}{3}\left(1 + \frac{2}{(1+\varepsilon_b)^3}\right), \tag{2.18a}$$

and

$$\eta(\varepsilon_b) = -\frac{3}{2(1+\varepsilon_b) + (1+\varepsilon_b)^4}. \tag{2.18b}$$

Eqs. (2.18) show that as ε_b becomes increasingly negative, both the effective stiffness E_b and the magnitude of nonlinearity parameter η increase. In particular, we find, by expanding Eqs. (2.18) for small ε_b, that the leading order corrections to E_b and η are linear in ε_b:

$$E_b/E = 1 - 2\varepsilon_b + \mathcal{O}\left(\varepsilon_b^2\right), \tag{2.19a}$$

$$\eta = -1 + 2\varepsilon_b + \mathcal{O}\left(\varepsilon_b^2\right). \tag{2.19b}$$

Furthermore, note that as $\varepsilon_b \to 0$, we retrieve $E_b/E = 1$ and $\eta = -1$, in agreement with the small strain limit of uniaxally compressed neo-Hookean materials given by Eq. (2.10b). In the following, we will take the first order corrections to η and E for finite ε_b into account. However, we

will show in section 2.6.2 that these ε_b corrections are subdominant for our theoretical prediction of the post-buckling slope.

Our previous expansion of the strain and stress profiles, and our determination of the post-buckling profile prefactors $\bar{C}_n$ and $\bar{D}_n$, provide a self-consistency check on the nonlinearity parameter η, detailed in the following. Using the scaling expressions given by Eq. (2.15), we can write the series expansion for the nominal strain, Eq. (2.15a), as:

$$\begin{aligned}\varepsilon(x) - \varepsilon_b = \bar{C}_0 t^4 \Delta u + \bar{C}_1 t^2 \Delta u^{\frac{1}{2}} \left(\frac{x}{w}\right) + \bar{C}_2 t^4 \Delta u \left(\frac{x}{w}\right)^2 \\ + \bar{C}_3 t^4 \Delta u^{\frac{1}{2}} \left(\frac{x}{w}\right)^3 + \mathcal{O}\left(\left(\frac{x}{w}\right)^4\right).\end{aligned} \tag{2.20a}$$

Similarly, we can write the series expansion for the nominal stress [Eq. (2.15b)] as:

$$\begin{aligned}\frac{\sigma(x) - \sigma_b}{E} = \bar{D}_0 t^4 \Delta u + \bar{D}_1 t^2 \Delta u^{\frac{1}{2}} \left(\frac{x}{w}\right) + \bar{D}_2 t^4 \Delta u \left(\frac{x}{w}\right)^2 \\ + \bar{D}_3 t^4 \Delta u^{\frac{1}{2}} \left(\frac{x}{w}\right)^3 + \mathcal{O}\left(\left(\frac{x}{w}\right)^4\right).\end{aligned} \tag{2.20b}$$

Substituting Eq. (2.20a) into Eq. (2.17) and comparing the post-buckling profile coefficients in each order of x with those of the proposed stress expansion of Eq. (2.20b), yields the following equalities in lowest order in Δu and t:

$$\bar{D}_0 = \bar{C}_0, \tag{2.21a}$$

$$\bar{D}_1 = \bar{C}_1, \tag{2.21b}$$

$$\bar{D}_2 = \bar{C}_2 + \eta \bar{C}_1^2, \tag{2.21c}$$

$$\bar{D}_3 = \bar{C}_3. \tag{2.21d}$$

The above equalities for the order $n = 0,2,3$ are consistent with the values of $\bar{C}_1$ and $\bar{D}_1$ in Table 2.2, within error bars, thus showing consistency with Eq. (2.17). Furthermore, the equality for $n = 2$, Eq. (2.21c), provides us with the following relation between C_n, D_n and η:

$$\eta = \frac{D_2 - C_2}{C_1^2}, \tag{2.22}$$

from which we then estimate, using Table 2.2, that $\eta \approx -1.0 \pm 0.6$. Though the deformations are not homogeneous in a buckled beam, we thus find that this indirect determination of η is consistent with the expected nonlinearity parameter for homogeneous uniaxial compression of neo-Hookean materials, raising further hope that our expansion scheme is consistent and correct.

2.4.4 Series expansion of the nominal shear stress and strain

As we had seen earlier (Fig. 2.4), shear effects become substantial for wide beams—the nominal shear and compressive strains have the same magnitude for a beam of $t = 0.1$. In this section we therefore analyse in detail how the nominal shear strain and stress profiles evolve with (i) the beam's width-to-length ratio t, and (ii) the post-buckling displacement, Δu. We find that the nominal shear strain and stress profile evolve similarly with Δu and t, which implies a *linear* stress-strain relation for the shear.

We consider the shear profile at an inflection point of the beam $(x, s = \ell/4)$, where the shear is maximal [see Fig. 2.4(c)]. We consider then the profiles $\gamma(x) \equiv \varepsilon_{xz}(x, s = \ell/4)$ and $\tau(x) \equiv \sigma_{xz}(x, s = \ell/4)$ to measure the spatial shape of the nominal strain and stress as a function of the scaled transverse coordinate x/w.

Polynomial expansion and asymptotic analysis

Following a similar series expansion as in Eqs. (2.11-2.12), we expand the nominal shear strain and stress profiles as:

$$\gamma\left(t, \Delta u, \frac{x}{w}\right) = \sum_{n=0} J_n\left(t, \Delta u\right)\left(\frac{x}{w}\right)^n, \tag{2.23a}$$

and

$$\frac{\tau}{G}\left(t, \Delta u, \frac{x}{w}\right) = \sum_{n=0} K_n\left(t, \Delta u\right)\left(\frac{x}{w}\right)^n, \tag{2.23b}$$

where J_n and K_n are the post-buckling profile coefficients of the expansion at order n. Note that prior to buckling, the beam simply undergoes uniform uniaxial compression and has not developed any curvature yet.

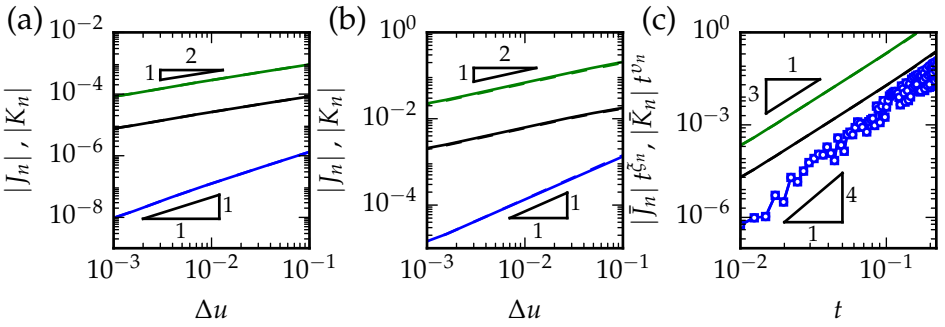

Figure 2.7: Dependence of the spatial nominal shear strain and stress profiles on Δu and t, obtained by FEM simulations. In black, blue and green we have plotted the post-buckling profile coefficients J_n (solid lines) and K_n (dashed lines), corresponding to order $n = 0$, $n = 1$ and $n = 2$ respectively. (a-b) We have plotted $|J_n|$ and $|K_n|$ as function of Δu for (a) a slender beam ($t = 0.02$) and (b) a thick beam ($t = 0.15$). (c) Dependence of J_n and K_n on the beam's aspect ratio t.

Therefore, unlike the uniaxial nominal strain and stress which are constant across the beam in the prebuckling regime, the shear stress and strain are strictly zero for $\Delta u \leq 0$.

Similarly to the post-buckling profile coefficients C_n and D_n [Eqs. (2.12)], we use that $J_n = K_n = 0$ at buckling, and we assume that the post-buckling profile coefficients J_n and K_n grow as power laws in t and Δu in the post-buckling regime:

$$J_n(t, \Delta u) = \bar{J}_n t^{\xi_n} \Delta u^{\Xi_n}, \tag{2.24a}$$

and

$$K_n(t, \Delta u) = \bar{K}_n t^{\upsilon_n} \Delta u^{\Upsilon_n}. \tag{2.24b}$$

Here, ξ_n, Ξ_n, υ_n and Υ_n are the post-buckling profile scaling exponents, and $\bar{J}_n$ and $\bar{K}_n$ are the post-buckling profile prefactors which are yet to be determined from numerical simulations.

To determine all the constants, we use the same set of $N = 10^2$ FEM simulations as before, from which we now extract the spatial shape of the nominal shear stress and strain as function of x/w along a cross section at one quarter of the beam, $s = \ell/4$, and fit $\gamma(x)$ and $\tau(x)/G$ to polynomials of order $n = 3$. From the resulting fits we then obtain the post-buckling

	Δu		t	
n	Ξ_n	Υ_n	ξ_n	v_n
0	0.49 ± 0.02	0.49 ± 0.02	3.02 ± 0.15	3.01 ± 0.15
1	1.03 ± 0.05	1.06 ± 0.05	3.98 ± 0.20	3.98 ± 0.20
2	0.50 ± 0.03	0.50 ± 0.03	3.02 ± 0.15	3.01 ± 0.15
3	1.02 ± 0.26	0.93 ± 0.23	5.93 ± 1.48	5.70 ± 1.43

Table 2.3: Post-buckling profile scaling exponents of Δu and t, for the expansion of the nominal shear strain and stress profiles as defined by Eqs. (2.23-2.24). Each row corresponds to a different order of n and results are provided up to cubic order $(n = 3)$. We estimate the errors using the same arguments as in Table 2.1, and estimate an error of 5% for $n \leq 2$ and 25% for $n = 3$.

profile coefficients J_n and K_n for a specific set of parameter values t and Δu. From these quantities we subsequently deduce the post-buckling profile scaling exponents and prefactors up to order $n = 3$.

Fitting protocol — In Fig. 2.7 we plot $|J_n|$ (solid lines) and $|K_n|$ (dashed lines) as function of Δu and t, from which we observe power law behaviour in Δu and t. To determine the post-buckling profile scaling exponents and prefactors we perform the same fitting procedure as in the previous section and provide the results in Tables (2.3-2.4), up to $n = 3$. Note that Fig. 2.7 shows results up to $n = 2$ for clarity.

Results — First, note from Fig. 2.7 that the curves for the shear stress and strain coincide. Similarly, $\bar{J}_n / \bar{K}_n \approx 1$, and we conclude that a linear relation governs the leading order relation between nominal shear stress and strain. Second, we find that the post-buckling profile scaling exponents for Δu equal 1 for even n, and $1/2$ for odd n which is precisely opposite to the situation for the uniaxial nominal stress and strain exponents. Third, the scaling exponents for t show that the zeroth and quadratic order $(n = 0, 2)$ together carry the lowest exponent in t, namely $\xi_0 = \xi_2 = v_0 = v_2 = 3$, followed by the linear order $(n = 1)$ which scales as t^4, and the cubic order $(n = 3)$ which scales as t^6.

n	$\bar{J}_n$	$\bar{K}_n$	$\bar{J}_n/\bar{K}_n$
0	-18.9 ± 1.9	-18.8 ± 1.9	1.0 ± 0.14
1	-45.3 ± 4.5	-45.3 ± 4.5	1.0 ± 0.14
2	205.9 ± 20.6	204.3 ± 20.4	1.0 ± 0.14
3	$-4.4 \cdot 10^3 \pm 1.8 \cdot 10^3$	$-3.7 \cdot 10^3 \pm 1.5 \cdot 10^3$	1.2 ± 0.68

Table 2.4: Post-buckling profile prefactors $\bar{J}_n$ and $\bar{K}_n$ and their ratio, for the expansion of the nominal shear strain and stress profiles as defined by Eqs. (2.23-2.24). Each row corresponds to a different order of n and results are provided up to cubic order ($n = 3$). Using the same arguments as in Table 2.2 we estimate an error of 10% for $n \leq 2$ and 40% for $n = 3$.

Discussion

We have quantified how the nominal shear stress and strain profiles arise beyond buckling and observed intricate powerlaw scaling with the transversal coordinate x/w, beam width-to-length ratio t and post-buckling strain Δu:

$$\gamma\left(t, \Delta u, \frac{x}{w}\right) = \sum_{n=0} \bar{J}_n t^{\zeta_n} \Delta u^{\Xi_n} \left(\frac{x}{w}\right)^n, \tag{2.25a}$$

and

$$\frac{\tau}{G}\left(t, \Delta u, \frac{x}{w}\right) = \sum_{n=0} \bar{K}_n t^{\upsilon_n} \Delta u^{\Upsilon_n} \left(\frac{x}{w}\right)^n. \tag{2.25b}$$

First, we observe that the post-buckling profile exponents and prefactors of the expansions given by Eqs. (2.25) are equal (Table 2.4). Therefore, the nominal shear strain and stress are linearly related, hence we can assume

$$\tau(x) = G\gamma(x), \tag{2.26}$$

which is the result as predicted by [52] in the case of simple shear for neo-Hookean materials. We will use this linear constitutive equation for the shear in the remainder of this chapter.

Upon further inspection of the exponents in Table 2.4 we notice that the zeroth and quadratic order ($\sim t^3$) are dominant at small t. The linear order ($\sim t^4$) then serves as a first order correction to the shear profile, while the cubic order ($\sim t^6$) represents a higher order correction.

Timoshenko's limit, $\mathcal{O}(t^3)$ — The dominant terms within the expansions given by Eqs. (2.25) encompass both the polynomial order $n = 0$ and $n = 2$, which show the same scaling with t and Δu. The quadratic $(n = 2)$ contribution to the nominal shear strain and stress is the strongest (Table 4). As a matter of fact, such a quadratic shear profile is in agreement with the textbook approach for the bending of linear elastic bars [100]. We will show later that this agreement is also quantitative.

Higher order corrections $\mathcal{O}(t^4)$ and convergence — The next contribution to Eqs. (2.25) is quartic in t and contains the linear correction to the shear stress and strain profiles $(n = 1)$. We will take this term into account throughout the remainder of this manuscript. Lastly, to ensure the convergence of the asymptotic approach, we also carried out the expansion up to sixth order in t, and showed that it results in a cubic, negligible correction to the shear stress and strain profiles — for a beam with $t = 0.15$ and an $\Delta u = 0.1$, its relative magnitude is $\lesssim 1\%$.

In conclusion, we have developed a systematic expansion of the stress and strain profiles that allow us to capture the leading order effect of finite beam width for the post-buckling regime. This expansion involves terms of the form $t^p \Delta u^q (x/w)^n$, and we use our FEM simulations to determine the exponents p and q for the uniaxial and shear components of the strain and stress at each power n. This procedure circumvents the need for heuristics to guess the important terms, and leads to a greatly simplified model where the dominant next order terms in t are properly taken into account.

2.5 Energy density including material nonlinearity

In this section, we construct the 1D energy density which includes material nonlinearities, which come in two flavours. We first present the simplest version of the energy density, which has zero free parameters and does not need numerical input, and which is based on the combination of stress-strain nonlinearity and Mindlin-Reissner strains. The second version of the model takes corrections to the Mindlin-Reissner strains, such as Timoshenko's shear correction factor, into account, and it is this version that needs numerical input. Finally, this section ends with a discussion

of the physical interpretation of these corrections and a clear overview of the dominant next order terms in t and Δu to the energy density.

We start by expressing the total increase of the elastic energy beyond buckling. This increase follows from an integral of the respective products of stress and strain, integrated over the surface area of the beam, that is,

$$\begin{aligned}\mathcal{E}/d = \int ds\,dx \Bigg(&\int_0^{\varepsilon_{xx}} d\varepsilon'_{xx}\sigma_{xx} + \int_0^{\varepsilon_{yy}} d\varepsilon'_{yy}\sigma_{yy} + \int_{\varepsilon_b}^{\varepsilon_{zz}} d\varepsilon'_{zz}\sigma_{zz} \\ &+ \int_0^{\varepsilon_{xy}} d\varepsilon'_{xy}\sigma_{xy} + \int_0^{\varepsilon_{yz}} d\varepsilon'_{yz}\sigma_{yz} + \int_0^{\varepsilon_{xz}} d\varepsilon'_{xz}\sigma_{xz}\Bigg).\end{aligned} \tag{2.27}$$

Even though we consider 2D beams, we keep a factor d (the depth) here to facilitate comparison to 3D beam results. For 2D beams, the 'yy', 'xy' and 'yz' contributions are zero. Moreover, since the beam can freely expand along the x direction without any barrelling effects near the boundaries, we expect that $\sigma_{xx} \approx 0$ at each point of the beam, which we have verified numerically. As a result, we are left with the 'zz' and 'xz' terms, which correspond to the uniaxial and shear deformations, respectively.

Our aim is to set up an energy functional using the Mind-lin-Reissner strains — 1D fields describing the shape of the beam along the curvilinear coordinate s. Therefore we define a linear energy density $\epsilon(s)$ as follows:

$$\mathcal{E} = \int_0^\ell ds\,\epsilon(s), \tag{2.28a}$$

where

$$\frac{\epsilon(s)}{d} = \int_{-\frac{w}{2}}^{\frac{w}{2}} dx \int_{\varepsilon_b}^{\varepsilon_{zz}(x)} \sigma\left(\varepsilon'_{zz}\right) d\varepsilon'_{zz} + \int_{-\frac{w}{2}}^{\frac{w}{2}} dx \int_{\varepsilon_b}^{\gamma(x)} \tau\left(\gamma'\right) d\gamma'. \tag{2.28b}$$

Here, $\epsilon(s)$ represents the linear energy density that captures the amount of energy in a cross sectional area of the beam per unit length of the curvilinear coordinate s.

2.5.1 1D energy density without distortions

Here we present the energy density constructed from the Mindlin-Reissner strains without additional distortions. In that case, the nominal axial

and shear strain profiles across the beam equal $\varepsilon_{zz}(x) = \varepsilon_b + \varepsilon_0 + \varepsilon_1 x$ and $\varepsilon_{xz}(x) = \gamma_0$. We then evaluate the energy density in Eq. (2.28b) using these strain profiles in combination with the nonlinear axial stress-strain relation given by Eq. (2.17) and the linear shear stress-strain relation given by Eq. (2.26), and find that

$$\frac{\epsilon}{E_b} = A\varepsilon_b\,\varepsilon_0 + \frac{1}{2}A\varepsilon_0^2 + I\left(\frac{1}{2} + \eta\,\varepsilon_0\right)\varepsilon_1^2 + \frac{GA}{2E_b}\gamma_0^2. \tag{2.29}$$

As can be seen from the above expression, the nonlinearity η introduces a coupling between the compressive strain ε_0 and the bending strain ε_1, and such coupling is absent in previous, linear, beam models [42, 43]. The energy density given by Eq. (2.29) forms the basis of our nonlinear beam model we will derive in section 2.6, and, as mentioned above, this energy density has zero free parameters and therefore does not rely on numerical input.

2.5.2 1D energy density including distortions

We now present the energy density comprising distortions from the Mindlin-Reissner strains and built with the aid of numerical results. To this end, we substitute the respective stress-strain relations [Eq. (2.17) and Eq. (2.26)] in Eq. (2.28b) and carry out the integration with respect to the nominal strains ε_{zz} and γ. Second, we integrate with respect to x by using the expansions of the uniaxial and shear strain profiles up to cubic order [Eq. (2.15a) and Eq. (2.25a)]. This yields:

$$\begin{aligned}\frac{\epsilon}{E_b A} = &\left\{\frac{\bar{C}_1^2}{24}\right\}\Delta u\, t^4 \\ &+ \left\{\frac{\bar{C}_1\bar{C}_3}{80} + \bar{C}_0\bar{C}_B + \frac{\bar{C}_2\bar{C}_B}{12} + \frac{G}{E_b}\left(\frac{1}{2}\bar{J}_0^2 + \frac{1}{12}\bar{J}_0\bar{J}_2 + \frac{1}{160}\bar{J}_2^2\right)\right\}\Delta u\, t^6 \\ &+ \left\{\frac{\bar{C}_3^2}{896} + \left(\frac{\bar{C}_0^2}{2} + \frac{\bar{C}_0\bar{C}_2}{12} + \frac{\bar{C}_2^2}{160} + \eta\frac{\bar{C}_0\bar{C}_1^2}{12} + \eta\frac{\bar{C}_1^2\bar{C}_2}{80} + \frac{G}{24E_b}\bar{J}_1^2\right)\Delta u\right\}\Delta u\, t^8 \\ &+ \mathcal{O}\left(\Delta u^2 t^{10}\right).\end{aligned} \tag{2.30}$$

We have now carefully established the beam's energy density up to second order in excess strain and eighth order in the beam's width-to-length

ratio, $\mathcal{O}\left(\Delta u^2 t^8\right)$. The above analysis identifies and quantifies precisely how nonlinearity in the stress-strain laws and distortions to the Mindlin-Reissner kinematics alter the 1D energy density formulation. While the order $\mathcal{O}\left(\Delta u t^4\right)$ corresponds exactly to Euler's elastica, the order $\mathcal{O}\left(\Delta u t^6\right)$ comprises the classical Timoshenko beam contribution as well as distortions from the linear bending profile. The order $\mathcal{O}\left(\Delta u^2 t^8\right)$ contains the nonlinearity η as well as further distortions for bending and shear.

After a few manipulations which we explain hereafter, it can be shown that Eq. (2.30) can be converted in terms of the Mindlin-Reissner strains as:

$$\begin{aligned}\frac{\epsilon}{E_b} = A\varepsilon_b\varepsilon_0 + \frac{1}{2}A\zeta_2(\eta)\varepsilon_0^2 + I\left(\frac{1}{2}\zeta_1(t) + \eta\,\varepsilon_0\right)\varepsilon_1^2 \\ + \frac{GA}{2E_b}\gamma_0^2\left(k_1 + k_2\gamma_0^2\right),\end{aligned} \tag{2.31a}$$

where the coefficients $\zeta_1(t)$ and $\zeta_2(\eta)$ are given by

$$\zeta_1(t) = 1 + 2\left(\frac{\bar{C}_2\bar{C}_B}{\bar{C}_1^2} + \frac{3}{20}\frac{\bar{C}_3}{\bar{C}_1}\right)t^2 + \frac{3}{112}\left(\frac{\bar{C}_3}{\bar{C}_1}\right)^2 t^4, \tag{2.31b}$$

$$\zeta_2(\eta) = 1 + \frac{1}{6}\frac{\bar{C}_2}{\bar{C}_0}\left(1 + \frac{3}{40}\frac{\bar{C}_2}{\bar{C}_0} + \frac{3}{20}\eta\frac{\bar{C}_1^2}{\bar{C}_0}\right), \tag{2.31c}$$

and where k_1 and k_2 are given by

$$k_1 = 1 + \frac{1}{6}\frac{\bar{J}_2}{\bar{J}_0} + \frac{1}{80}\left(\frac{\bar{J}_2}{\bar{J}_0}\right)^2, \tag{2.31d}$$

and

$$k_2(t) = \frac{1}{12}\frac{\bar{J}_1^2}{\bar{J}_0^4}t^{-4}. \tag{2.31e}$$

To obtain the above results we have used the fact that there is a clear pattern in the scaling exponents of the higher order corrections of the uniaxial and shear strain profiles with the excess displacement Δu, which alternate between 1/2 or 1 (see Tables 2.1 and 2.3). Consequently, we can factorize the Δu dependence and express the higher order corrections in terms of the Mindlin-Reissner strains. For example, the quadratic post-buckling profile coefficient of the axial strain profile, $C_2 = \bar{C}_2\Delta u\, t^4$, can be expressed in terms of $\varepsilon_0 \equiv C_0 = \bar{C}_0\Delta u\, t^4$ as $C_2 = (\bar{C}_2/\bar{C}_0)\,\varepsilon_0$.

2.5.3 Discussion

Here we discuss the physical interpretation of the corrections to the Mindlin-Reissner strains, and provide a clear overview of the dominant next order terms in t and Δu to the energy density.

Shear correction factors— Using Table 2.4, k_1 and k_2 can be evaluated as $k_1 = 0.67 \pm 0.15$ and $k_2(t) \approx 0.0013\, t^{-4}$. The constant k_1 is formally known as Timoshenko's shear correction factor and our numerical value is in agreement with the value known in literature for beams with a rectangular cross section [102–104]. The shear correction factor accounts for the strongly quadratic, rather than uniform, shape of the shear profile across the beam [100]. This strong quadratic shape is also directly reflected by the data shown in Fig. 2.7, where the quadratic component is dominant over the zeroth and linear order component.

The quantity $k_2(t)$ corrects for the linear component of the shear strain profile and represents a higher order correction to the shear profile. Note that even though $k_2(t)$ is singular for $t \to 0$, $k_2(t)$ appears only within the product $k_2\gamma_0^4$ in Eq. (2.31a) (with $\gamma_0 \sim t^4$), such that the product $k_2\gamma_0^4$ is regularized for $t \to 0$.

Bending correction factors— Using Table 2.2, $\zeta_1(t)$ and $\zeta_2(\eta)$ can be evaluated as $\zeta_1(t) \approx 1 + 6\left(t^2 + t^4\right)$ and $\zeta_2(\eta) \approx 0.8 - 0.15\eta$. These quantities, which we refer to as bending corrections factors, describe the distortion of the linear strain profile, and thus take an analogous role as the shear correction factors described above, yet for bending. The mapping of energy contributions that arise from distortions of the linear strain profile onto the Mindlin-Reissner strains is one of the crucial aspects of this section.

Summary— We summarize our findings in Table 2.5: This clear analysis of the leading order terms and their relation to Timoshenko ($\mathcal{O}(\Delta u\, t^6)$) and Mindlin-Reissner ($\mathcal{O}(\Delta u^2\, t^8)$) beam formulations is one of the key results of this work.

Model	Euler's Elastica	Timoshenko w/ bending correction	This work
Order	$\mathcal{O}(\Delta u\, t^4)$	$\mathcal{O}(\Delta u\, t^6)$	$\mathcal{O}(\Delta u^2\, t^8)$
Terms	$1/2\, I\varepsilon_1^2$	$1/2\, I\,(\zeta_1(t) - 1 - \zeta_1'(t))\,\varepsilon_1^2$ $+ A\varepsilon_b\varepsilon_0 + 1/2\, GAk_1\gamma_0^2/E_b$	$I\,(\eta\varepsilon_0 + 1/2\, I\,\zeta_1'(t))\,\varepsilon_1^2$ $+ 1/2\, A\zeta_2(\eta)\varepsilon_0^2$ $+ 1/2\, GAk_2\gamma_0^4/E_b$

Table 2.5: Summary of the leading order terms in the expression of the (rescaled) linear energy density ϵ/E_b, extracted from Eqs. (2.30-2.31). We have defined $\zeta_1'(t) \equiv \frac{3}{112}\left(\frac{\bar{C}_3}{\bar{C}_1}\right)^2 t^4$ for convenience. While we recover exactly Euler's elastica at the order $\mathcal{O}(\Delta u\, t^4)$, our results suggest that Timoshenko's approximation requires a correction from the nonlinear bending profile at order $\mathcal{O}(\Delta u\, t^6)$. Moreover, this demonstrates that our work encompasses a higher order correction for the shear and a nonlinear correction for the stress-strain nonlinearity.

2.6 1D nonlinear beam model

In this section we formulate a 1D nonlinear model to describe the post-buckling of wide beams. Our model assumes (i) that the kinematics of the 1D model are captured by the Mindlin-Reissner strains, namely axial strain, curvature and shear [41]; (ii) that axial stress and strain are related nonlinearly. Based on these assumptions, we derive an expression for the 1D energy density as well as the governing equations for the mechanical equilibrium of wide beams. We then analytically solve the governing equations and find excellent agreement with 2D simulations for the post-buckling behaviour, without any adjustable parameters. Finally, we refine our beam model using extensive 2D simulations and show that distortions from Mindlin-Reissner kinematics have a negligible effect on the predictions by the model.

2.6.1 Mindlin-Reissner beam with a nonlinear stress-strain relation

Mindlin-Reissner kinematics describe beams that can be compressed, bent and sheared. These three deformation modes are quantified by a compressive $\tilde{\varepsilon}_0(s)$, curvature $\varepsilon_1(s) \equiv \theta_s(s)$ and shear strain $\gamma_0(s)$, as function

of the curvilinear coordinate s along the beam's central axis, with θ the deflection angle of the beam's axis with respect to the vertical. Therefore the total elastic energy of these beams is a functional of the form

$$\mathcal{E}\left[\tilde{\varepsilon}_0(s),\theta(s),\varepsilon_1(s),\gamma_0(s)\right] = \int_0^\ell ds\, \epsilon\left[s,\tilde{\varepsilon}_0(s),\theta(s),\varepsilon_1(s),\gamma_0(s)\right], \tag{2.32}$$

where the 1D energy density of the beam $\epsilon\left[s,\tilde{\varepsilon}_0(s),\theta(s),\varepsilon_1(s),\gamma_0(s)\right]$ exclusively depends on these strains.

The second key assumption is that stress and strain are related nonlinearly. To describe the vicinity of post-buckling, we set up an expansion of the nominal stress σ around the buckling strain ε_b up to quadratic order. This expansion, as derived already in section 2.4.3, yields

$$\frac{\sigma-\sigma_b}{E_b} = (\varepsilon-\varepsilon_b) + \eta\,(\varepsilon-\varepsilon_b)^2 + \mathcal{O}\,(\varepsilon-\varepsilon_b)^3, \tag{2.17}$$

where E_b and σ_b are the effective Young's modulus and nominal stress at buckling. In the case of neo-Hookean materials under plane stress conditions, the coefficients of this expansion can be determined analytically and read $\eta = -1 + \mathcal{O}(\varepsilon_b)$ and $E_b = E + \mathcal{O}(\varepsilon_b)$ (see section 2.4.3 for a demonstration). In the case of plane strain conditions, not considered here, it can be shown that $\eta = -3/2 + \mathcal{O}(\varepsilon_b)$ (see appendix 2.B.2). The nonlinearity of the above stress-strain relation stems from the combination of large deformations and incompressibility and can qualitatively be understood from the fact that upon compression (tension) the cross-sectional area increases (decreases) and the stress-strain curve is therefore effectively stiffening (softening). In addition, we assume a linear relation between the nominal shear stress τ and shear strain γ, $\tau = G\gamma$ in agreement with the elasticity of neo-Hookean materials [52].

Based on these two assumptions, we find that the 1D energy density describing post-buckling reads (see section 2.5):

$$\begin{aligned}\epsilon\left[\varepsilon_0(s),\varepsilon_1(s),\gamma_0(s)\right] =& E_b A\,\varepsilon_b\,\varepsilon_0 + \frac{1}{2}E_b A\varepsilon_0^2 \\ &+ E_b I\left(\frac{1}{2}+\eta\,\varepsilon_0\right)\varepsilon_1^2 \\ &+ \frac{GA}{2}\,\gamma_0^2,\end{aligned} \tag{2.33}$$

with $\varepsilon_0(s) = \tilde{\varepsilon}_0(s) - \varepsilon_b$, $A = wd$ (the cross-sectional area) and G is the shear modulus. Note that the nonlinear correction proportional to η introduces a coupling between the compressive and bending strain, given by $\varepsilon_0\varepsilon_1^2$, and such coupling is absent in previous linear beam models [42, 43].

To establish the governing beam equations, the total elastic energy $\mathcal{E}$ has to be minimized under the geometrical constraint set by the boundary conditions. In the case of Euler buckling, a uniaxial displacement is applied along the vertical axis of the beam and is associated to the following geometrical constraint:

$$\Pi = F\left(u - \left(\ell - \int_0^\ell ds\,((1+\varepsilon_b+\varepsilon_0)\cos\theta - \gamma_0\sin\theta)\right)\right), \tag{2.34}$$

where F is the Lagrange parameter associated with the axial displacement u that corresponds to the external axial force applied on the beam. We use the fact that $\varepsilon_1 \equiv \theta_s$ to apply the Euler-Lagrange formulation [105] on the energy functional including the constraint:

$$\tilde{\mathcal{E}}\left[\varepsilon_0(s), \theta(s), \varepsilon_1(s), \gamma_0(s)\right] = \int_0^\ell ds\,\epsilon - \Pi, \tag{2.35}$$

which yields the governing equations of the beam:

$$E_b I\theta_{ss} + F\left\{(1+\varepsilon_b+\varepsilon_0)\sin\theta + \gamma_0\cos\theta\right\} + 2\eta E_b I\left(\theta_s\varepsilon_0\right)_s = 0, \tag{2.36a}$$

$$F\cos\theta + E_b A\left(\varepsilon_b+\varepsilon_0\right) + \eta E_b I\theta_s^2 = 0, \tag{2.36b}$$

$$GA\gamma_0 - F\sin\theta = 0. \tag{2.36c}$$

This set of three coupled equations determine the beam's central axis in the post-buckling regime of wide beams. We will refer to this set of equations as the 1D *nonlinear* beam model, since it includes the nonlinearity η.

Please note that in the limit of linear materials ($\eta = 0$ and $E_b = E$), Eqs. (2.36) correspond to the equations for a shearable and extensible beam derived by [43]. If additionally the beam is assumed non-shearable, $\gamma_0(s) = 0$ and Eq. (2.36c) drops out, leaving us with a simpler model derived by [42]. Finally, for inextensible beams $\varepsilon_0(s) = \varepsilon_b = 0$, Eq. (2.36b) drops out, and we recover Euler's elastica $EI\theta_{ss} + F\sin\theta = 0$ [24]. Our beam model thus correctly captures all these linear models.

2.6.2 Solutions to the 1D nonlinear beam model

In this section we solve the 1D nonlinear beam model given by Eqs. (2.36) and show that the post-buckling slope is dramatically changed and the compressive Mindlin-Reissner strain significantly improved, when incorporating a nonlinearity η.

Dimensionless form

The results below will be presented in dimensionless form and we introduce the following dimensionless quantities:

$$\bar{s} = \frac{s}{\ell}; \qquad \bar{F} = \frac{F\ell^2}{E_b I}; \qquad \Lambda^{-2} = \frac{I}{A\ell^2}. \tag{2.37}$$

The quantities $\bar{s}$ and $\bar{F}$ represent the dimensionless curvilinear coordinate and force respectively, and $\Lambda \sim \ell/w$ can be recognized as the slenderness ratio [30]. Using the dimensionless quantities, the set of scaled beam equations that follows from Eqs. (2.36) reads:

$$\theta_{\bar{s}\bar{s}} + \bar{F}\left\{(1+\varepsilon_b+\varepsilon_0)\sin\theta + \gamma_0\cos\theta\right\} + 2\eta(\theta_{\bar{s}}\,\varepsilon_0)_{\bar{s}} = 0, \tag{2.38a}$$

$$\varepsilon_0 = -\left(\bar{F}\Lambda^{-2}\cos\theta + \eta\Lambda^{-2}\theta_{\bar{s}}^2 - \varepsilon_b\right), \tag{2.38b}$$

$$\gamma_0 = \bar{F}\Lambda^{-2}\frac{E_b}{G}\sin(\theta). \tag{2.38c}$$

In the remainder of this chapter we drop the over-bars, unless if noted otherwise. For convenience, we additionally define:

$$r \equiv \frac{E_b}{G} = 2(1+\nu) + \mathcal{O}\left(\varepsilon_b(t)\right), \tag{2.39}$$

where ν is the Poisson's ratio.

In Eqs. (2.38) we use Euler's prediction for ε_b that accurately describes the onset of buckling, even for wide beams [Fig. 2.2(a)]. Furthermore, all the parameters E_b, r and η can be determined theoretically to leading order in the beam width-to-length ratio t. In what follows we use these predictions as input parameters and solve Eqs. (2.38) to obtain a closed-form expression for the post-buckling slope as function of and to leading order in t.

Closed-form expression for the post-buckling slope as a function of t.

Here we derive our main result, namely the post-buckling slope as a function of beam width-to-length ratio t. In deriving the post-buckling slope, we are interested only in the mechanical response of the beam infinitesimally beyond buckling. Therefore, we only need to solve Eqs. (2.38) for small $(\theta(s) \ll 1)$, yet nonlinear beam deflections. As a first step, we expand the governing beam equations up to the cubic order in θ, and substitute Eqs. (2.38b-2.38c) into Eq. (2.38a) to obtain:

$$\begin{aligned} 0 = \theta_{ss}\left(1 - 2\eta\left(F\Lambda^{-2} + \varepsilon_b\right) - 6\theta_s^2\Lambda^{-2}\eta^2\right) + \theta\left(F + (r-1)F^2\Lambda^{-2}\right) \\ - \theta^3\left(\frac{1}{6}F + \frac{2}{3}(r-1)F^2\Lambda^{-2}\right) + \theta^5\left(\frac{1}{12}F^2\Lambda^{-2}(r-1)\right) \\ + \left(\theta^2\theta_{ss} + \theta\theta_s^2 + \frac{1}{6}\theta^3\theta_s^2\right)F\Lambda^{-2}\eta. \end{aligned} \tag{2.40}$$

We now solve this expanded equation using a perturbative expansion that is consistent with the symmetry of Eq. (2.40), which only contains odd powers in θ, and that matches the imposed clamped-clamped boundary conditions, $\theta(0) = \theta(1) = 0$:

$$\theta(s) = \alpha \sin 2\pi s + \beta \sin 6\pi s. \tag{2.41}$$

Here, α and β physically correspond to the maximum deflection angle of the first and third harmonic of the Fourier series which describe the beam shape $\theta(s)$. To see how α and β are coupled, we substitute the perturbative expansion for $\theta(s)$ in Eq. (2.40). By collecting all terms proportional to $\sin(6\pi s)$, and setting the sum of their coefficients to zero, we found that β is coupled to a higher power of α, specifically $\beta \sim \alpha^3$. Therefore, since $\alpha \ll 1$, $\beta \ll \alpha$, and in the following we set $\beta = 0$.

Under the assumption $\beta = 0$, Eq. (2.40) leads to an explicit equation relating the force F to the deflection α. Expanding $F(\alpha)$ for small deflection α, yields the shape of the pitchfork bifurcation [106]:

$$F(\alpha, \Lambda, \eta, r) = F_c + \kappa\alpha^2 + \mathcal{O}(\alpha^4), \tag{2.42}$$

where κ is the curvature of the pitchfork. To connect this excess force to the axial displacement u, we establish the relation between the deflection

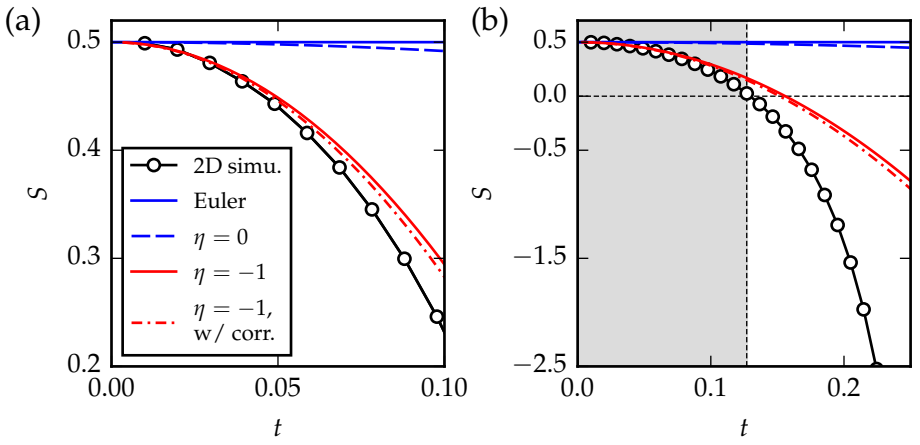

Figure 2.8: Post-buckling slope S as function of the beam width-to-length ratio t, for five different models. In the Euler limit $S = 1/2$, while in 2D simulations (open circles) S varies with t. Solutions to our model, given by Eq. (2.44), are shown for $\eta = 0$ (dashed blue) and $\eta = -1$ (solid red). Finally, we also show data for an extension of our model discussed in section 2.6.3 (dash-dotted red). (a-b) Panel (a) shows a close-up for $0 < t < 0.10$ and panel (b) shows a wider range of width-to-length ratio $(0 < t < 0.25)$. The shaded region indicates the cross-over to subcritical buckling $(S < 0)$ for the 2D simulations.

angle α and the axial displacement using the geometrical relation

$$u/\ell = 1 - \int_0^1 ds\,\{(1 + \varepsilon_b + \varepsilon_0)\cos\theta - \gamma_0 \sin\theta\}, \tag{2.43}$$

which upon small deflections, can be expanded to obtain the desired relation $u(\alpha, F, \Lambda, \eta, r)$. We then invert this relation to $\alpha(u, F, \Lambda, \eta, r)$ and substitute it in Eq. (2.42), resulting in an equation that needs to be solved for $F(u, \Lambda, \eta, r)$. The final step is then to expand the solution for F in the limit $u \to u_c^+$, which leads to an equation of the form as in Eq. (2.2), with the post-buckling slope S equal to:

$$S = \frac{1}{2} - \left(\frac{1}{12} + 2\eta^2\right)\pi^2 t^2 + \mathcal{O}(t^4). \tag{2.44}$$

This result confirms that Euler's elastica prediction $(S = 1/2)$ is recovered in the limit of slender beams $(t \to 0)$ and shows that the leading

order correction to the post-buckling slope S is quadratic in t. Notice that such correction comprises the stress-strain nonlinearity η. Does this correction bring an improvement for the prediction of the post-buckling slope? To check this, we compare the value of the post-buckling slope S obtained from 2D simulations to the prediction of Eq. (2.44), where the value of η is independently determined using the neo-Hookean model under the simplifying assumption that the neo-Hookan material is uniaxially compressed (see section 2.4.3). The comparison shown in Fig. 2.8 shows excellent agreement between the simulations and our prediction in Eq. (2.44), namely the quadratic correction matches the data very well for small t and remains accurate up to $t \approx 0.1$ [Fig. 2.8(a)]. Although we should not expect our prediction to be accurate for wider beams, it remains in qualitatively agreement with the simulations and succeeds in predicting subcritical buckling at a critical width-to-length ratio $t \approx 0.15$ [Fig. 2.8(b)].

Beyond the success of our asymptotic approach, a closer inspection of the quadratic correction to the post-buckling slope S [Eq. (2.44)] allows us to infer three important conclusions. First, the quadratic correction is independent of the ratio of moduli r, given by Eq. (2.39). Since r sets the magnitude of shear deformations with respect to uniaxial compression, we conclude that shear is subdominant in the lowest order terms of $S(t)$. Second, the coefficient of the quadratic correction is quadratic in η [Eq. (2.44)], suggesting the sign of the nonlinearity does not play a role. This finding is consistent with earlier simulations and experiments on metabeams characterized by a positive nonlinearity ($\eta > 0$) [40], which similar to plain neo-Hookean beams ($\eta < 0$) were found to display a decreasing post-buckling slope as function of beam width. Third, the coefficient of the quadratic correction confirms our initial hypothesis that the stress-strain nonlinearity is the crucial ingredient to capture $S(t)$ correctly: The magnitude of this coefficient is entirely determined by the nonlinearity parameter η. In the absence of η the magnitude of the coefficient is much smaller, and $S(t)$ would be only weakly decreasing with t (see Fig. 2.8). We thus conclude that the nonlinearity η ensures that our theoretical prediction in Eq. (2.44) is able to capture the subcritical buckling at realistic aspect ratios, in contrast to earlier linear theories [41–43].

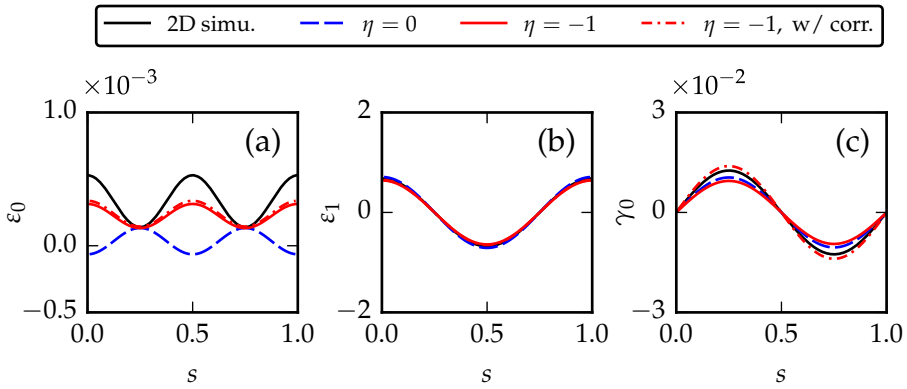

Figure 2.9: Mindlin-Reissner strains as a function of s, for four different models. We consider a wide ($t = 0.1$) beam which is compressed to an axial displacement of $u/u_c = 1.06$. We show results for 2D simulations (solid black), and compare them to numerical solutions to our beam model in Eqs. (2.38) for $\eta = 0$ (dashed blue) and $\eta = -1$ (solid red). Finally, we also show numerical solutions to an extension of our beam model in Eqs. (2.48) discussed in section 2.6.3 (dash-dotted red). (a-c) We have respectively plotted the compressive, bending and shear Mindlin-Reissner strain along the beam.

Mindlin-Reissner strains in the nonlinear beam model

We will now illustrate that the prediction for the compressive Mindlin-Reissner strain $\varepsilon_0(s)$ is significantly improved by the nonlinearity η. In Fig. 2.9(a-c) we plot the compressive, bending and shear Mindlin-Reissner strain for the 2D simulations and the beam model in Eqs. (2.38). First, panel (a) shows a significant qualitative difference in the Mindlin-Reissner strain $\varepsilon_0(s)$ between the linear and nonlinear beam model. In contrast to the linear beam model, the nonlinear beam model is in good qualitative agreement with the FEM simulations and the prefactors of the sinusoidal modulations all carry the same sign, albeit with a slightly smaller amplitude. This confirms our earlier assertion that the nonlinearity η is the crucial factor to capture correctly the large deformations of wide neo-Hookean beams. Finally, panel (b) and (c) show that the Mindlin-Reissner strains $\varepsilon_1(s)$ and $\gamma_0(s)$ remain essentially unchanged due to the nonlinearity and the model shows excellent agreement with the 2D simulations.

2.6.3 Distortions from Mindlin-Reissner kinematics with nonlinear stress-strain relation

The previous derivation of the 1D nonlinear beam model in Eqs. (2.38) is simple and directly follows from the use of two basic assumptions. In particular, using Mindlin-Reissner kinematics is a customary yet not controlled assumption. In this section, we investigate the validity of such a choice by using extensive numerical simulations and demonstrate that distortions from the Mindlin-Reissner kinematics systematically occur, modifying the 1D energy density and governing equations, albeit with a subdominant effect.

To explore deviations from Mindlin-Reissner strains, we have systematically investigated the stress and strain profiles in section 2.4. In particular, we find that the axial strain profile at the centre of the beam takes the form

$$\varepsilon(x) = \tilde{\varepsilon}_0 + \varepsilon_1 x + \varepsilon_2 x^2 + \varepsilon_3 x^3 + \cdots, \tag{2.45}$$

where $x \in [-\frac{w}{2}, \frac{w}{2}]$ is the transverse coordinate across the beam width. Furthermore, $\tilde{\varepsilon}_0 = \varepsilon_b + \varepsilon_0$ and ε_1 are Mindlin-Reissner strains introduced in section 2.3, and ε_i (with $i \geq 2$) correspond to distortions from a linear axial strain profile. In section 2.4 we have also performed a similar systematic analysis for the shear profile.

Based on the extensive simulations and thorough asymptotic analysis procedure in sections (2.4-2.5), we found that the 1D energy density takes the form:

$$\begin{aligned} \epsilon\left[\varepsilon_0(s), \varepsilon_1(s), \gamma_0(s)\right] =& E_b A\, \varepsilon_b\, \varepsilon_0 + \frac{1}{2} E_b A \left(1 + \zeta_2(\eta)\right) \varepsilon_0^2 \\ &+ E_b I \left(\frac{1}{2}\left(1 + \zeta_1(t)\right) + \eta\, \varepsilon_0\right) \varepsilon_1^2 \\ &+ \frac{GA}{2} \gamma_0^2 \left(k_1 + k_2 \gamma_0^2\right), \end{aligned} \tag{2.46}$$

where the coefficients E_b, η, $\zeta_1(t)$, $\zeta_2(\eta)$, G, k_1 and k_2 can be determined numerically. Note that in the limit when ζ_1,ζ_2 and k_2 are zero, we recover Eq. (2.33). Eq. (2.46) is very similar to Eq. (2.33) and the numerical values of the coefficients E_b, η, and G match the values that come from the neo-Hookean material model [52] (see section 2.4). In addition we see that the differences associated to distortions from the Mindlin-Reissner

kinematics can be captured by the coefficients $\zeta_1(t)$, $\zeta_2(\eta)$, k_1 and k_2. While $k_1 = 0.67 \pm 0.15$ is a classical coefficient known as the shear correction factor [100, 102] whose value quantitatively matches Timoshenko's prediction [103, 104], $\zeta_1(t)$, $\zeta_2(\eta)$, and k_2 are undocumented and correspond to higher order distortions of the strain profiles. They have been determined in section 2.4 as:

$$\zeta_1(t) = 6\left(t^2 + t^4\right), \tag{2.47a}$$

$$\zeta_2(\eta) = -0.2 - 0.15\eta, \tag{2.47b}$$

$$k_2(t) = 0.0013t^{-4}. \tag{2.47c}$$

Note that even though $k_2(t)$ is singular for $t \to 0$, γ_0 scales as t^4, such that the product $k_2\gamma_0^4$ that arises in Eq. (2.46) is regularized for $t \to 0$. Nonetheless, we see that the distortions in Eqs. (2.47) introduce minor modifications to the prefactors in Eq. (2.46) and in what follows we show that they do not play a major role in the model.

We now carry out the same Euler-Lagrange approach as previously and find the refined governing equations:

$$\zeta_1(t)E_bI\theta_{ss} + F\{(1+\varepsilon_b+\varepsilon_0)\sin\theta + \gamma_0\cos\theta\} + 2\eta E_bI(\theta_s\varepsilon_0)_s = 0, \tag{2.48a}$$

$$F\cos\theta + E_bA(\varepsilon_b + \zeta_2(\eta)\varepsilon_0) + \eta E_bI\theta_s^2 = 0, \tag{2.48b}$$

$$GA\gamma_0\left(k_1 + 2k_2\gamma_0^2\right) - F\sin\theta = 0. \tag{2.48c}$$

This set of equations is the equivalent of the previously established beam equations [Eqs. (2.38)] and has been determined through a well defined and rigorous set of assumptions. Unfortunately, the coefficients $\zeta_1(t)$, $\zeta_2(\eta)$ and k_2 have to be determined numerically. Following the procedure in section 2.6.2 we linearise and solve Eqs. (2.48) and find that

$$S = \frac{1}{2} + \frac{\left(-3 + 2\left(1+\zeta_2(\eta)\right) - 24\eta^2\right)\pi^2}{12\left(1+\zeta_2(\eta)\right)}t^2 + \mathcal{O}(t^4), \tag{2.49}$$

which reduces to Eq. (2.44) by setting $\zeta_2 = 1$. We have plotted Eq. (2.49) in Fig. 2.8 and see that the corrections ζ_1,ζ_2 and k_2 result in a minor improvement to the post-buckling prediction for S. Finally, we numerically solved Eqs. (2.48) to obtain the Mindlin-Reissner strains and plotted the result for $\eta = -1$ in Fig. 2.9. Again, we find that the corrections result in a

minor improvement to the post-buckling prediction, now for the Mindlin-Reissner strains. Altogether, this illustrates that the corrections ζ_1, ζ_2 and k_2 have a subdominant contribution to the post-buckling behaviour.

2.7 Conclusions and discussion

We have presented a thorough investigation of the post-buckling of nonlinear elastic beams, using experiments, finite element simulations and theory. In particular we have focussed on subcritical buckling, where, for neo-Hookean beams, the slope of the force-displacement curve becomes negative beyond buckling when the beam width-to-length ratio exceeds 12%. The main result of this chapter is a 1D nonlinear beam model that includes a material nonlinearity η. We constructed the model by building the beam's energy density using Mindlin-Reissner kinematics with a nonlinearity in the stress-strain relation, and demonstrated that this nonlinearity is crucial to accurately capture the post-buckling behaviour of wide beams and in particular to predict subcritical buckling. In contrast with previous works that have reported a significant effect of the ratio E/G on the flexure response [80] and the critical buckling force [43] of extensible and shearable beams, we found that E/G has a subdominant effect on the post-buckling slope.

Though our model has been established in the case of neo-Hookean material nonlinearity $(\eta < 0)$, our findings could be generalized to a wider class of nonlinear elastic materials, such as cellular materials with nonlinear effective properties [21, 92, 107]. We expect this generalization to hold provided that the leading nonlinearity of the elastic material is quadratic in nature and that the material strains do not significantly deviate from the Mindlin-Reissner strain decomposition (as is shown in section 2.6.3 for 2D plane stress beams). For example, in recent work by [40], beams patterned with a periodic 2D pattern of pores were shown to exhibit positive, geometrically induced nonlinearity $(\eta > 0)$. They found that a sufficiently strong nonlinearity leads to subcritical buckling, even when the beam width-to-length ratio is small. Such a transition to subcritical buckling for $\eta > 0$ is in qualitative agreement with our theory that predicts that the post-buckling slope essentially decreases quadratically in η with its maximum at $\eta = 0$ (Fig. 2.10). The present work rationalizes those findings and provide strong guidelines for the design of

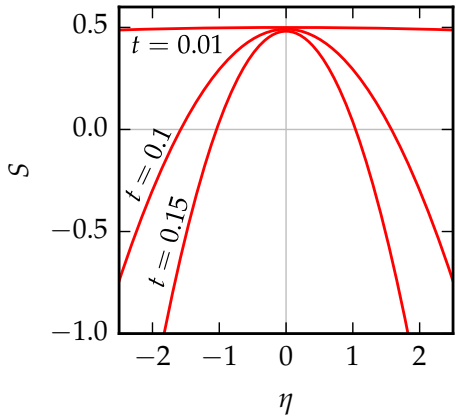

Figure 2.10: Post-buckling slope as a function of the nonlinearity η. Using Eq. (2.44) we have plotted $S(\eta)$ for $t = 0.01$, $t = 0.1$ and $t = 0.15$. The curves show that the post-buckling slope is quadratic in η and that the post-buckling slope does not exceed $S = 1/2$.

post-instability regimes in soft structures and metamaterials [108], where arbitrary values of η can be achieved [92]. We envision in particular that our description could be of interest for the design of compliant hierarchical cellular materials, which often rely on the buckling instability for their functionality [109, 110].

In addition, we note that other types of material nonlinearities could be explored and addressed within our framework, for instance, plasticity, stress-relaxation, swelling [111–115] or even growth and activity, which are ubiquitous in biological solids [116, 117]

Finally, while our work could be of great use for the engineering of systems that draw on Euler buckling for their functionality [36, 118], a plethora of compliant metamaterials harness the *snapping* instability [36, 44, 54, 58, 61, 119–122]. In order to understand the role of material nonlinearities on such instabilities and to devise mechanical design guidelines, our present framework should be generalized to pre-curved geometries, such as curved beams and shells.

Appendix

2.A Numerical protocol for nonlinear buckling analysis

To determine the numerical force-displacement curve, we develop a two-step protocol. First, we perform a step-wise nonlinear stability analysis to approach the buckling displacement, u_c, with a relative accuracy of 10^{-3}. Such a step-wise nonlinear stability analysis consists of successive linear buckling analysis steps to take into account the change in beam geometry for large deformations. Subsequently, we perform an eigenfrequency analysis to determine numerically the proximity of the critical point.

Second, we probe the (stable) post-buckling branch for axial displacements $u > u_c$. One problem that arises in the FEM simulations, however, is that the beam will not automatically jump to one of the two new stable branches that occur once the compression of the initial configuration exceeds u_c: The beam's symmetry is retained even for $u > u_c$ and the beam remains on the unstable branch. One possibility to circumvent this problem would be to seed the initial configuration with imperfections that ensure that the beam selects one of the two stable post-buckling branches. A major drawback of this approach is that it destroys symmetry, hence unfolding the pitchfork bifurcation that underlies buckling, and consequently makes it impossible to study the post-buckling branch in the vicinity of the critical point. In this chapter we crucially need to be able to probe the post-buckling branch in the vicinity of the critical point; we investigate the buckling properties of beams down to a relative post-buckling displacement as small as 10^{-3}. To probe the post-buckling branch with high accuracy, we make use of a temporary transverse perturbation at the centre of the beam: Having obtained u_c from the nonlinear stability analysis, we compress the initial configuration up to $0.95\,u_c$. Next, we force the beam in the bifurcated, buckled state by subsequently applying the transverse pertubation, increasing the compression up to $1.05\,u_c$ and releasing the transverse pertubation again. We then further probe this particular post-buckling branch by the increase of the compressive displacement up to $u = 2\,u_c$. Finally, we smoothly decrease the axial displacement from $u = 2\,u_c$ back to $u = 0.95\,u_c$ from which we can precisely backtrack the post-buckling branch. Altogether, this protocol allows to determine the location of the instability and the post-buckling behavior with high accuracy.

2.B Nonlinear stiffening of hyper-elastic beams

In this appendix we demonstrate for a neo-Hookean material model how the leading nominal stress-strain nonlinearity, η, manifests itself in the pre-buckling regime for beams under (i) plane stress and (ii) plane strain conditions. The focus of our work presented in this chapter lies on plane stress conditions, but we also determine η for the plane strain case which could be used as a further generalization to our model given by Eqs. (2.38).

In the derivation below we consider a beam under unaxial loading in the z-direction with its depth parallel to the y-axis [e.g. as in Fig. 2.1(a)], and allow for free lateral expansion at the boundaries unless noted otherwise. We then determine the leading nonlinearity η by expanding the axial nominal stress-strain relation $\sigma_{zz}(\varepsilon_{zz})$ for small strains as

$$\sigma_{zz}/E = \varepsilon_{zz} + \eta\varepsilon_{zz}^2 + \mathcal{O}(\varepsilon_{zz}^3), \tag{2.50}$$

where ε_{zz} and σ_{zz} are the vertical nominal strain and stress. Since the rubbers used in our experiments are well described by the incompressible formulation of nonlinear elasticity [93], we employ the strain energy density for an incompressible neo-Hookean material [52]

$$W = \frac{E}{6}\left(\lambda_1^2 + \lambda_2^2 + \lambda_3^2 - 3\right), \tag{2.51}$$

with E Young's modulus and λ_i the stretch in the principal direction $\hat{\mathbf{e}}_\mathbf{i}$. The stretch λ is defined as the length ratio given by the length of a deformed line element to the length of the corresponding undeformed line element. Hence, $\lambda_i < 1$ expresses compression and $\lambda_i > 1$ extension of an element oriented along direction $\hat{\mathbf{e}}_\mathbf{i}$. For an incompressible material the volume must remain unchanged under any deformation, which in terms of the principal stretches translates into the constraint $\lambda_1\lambda_2\lambda_3 = 1$. Enforcing the constraint with the aid of a Lagrange multiplier Π, the stress-stretch relation for an incompressible, isotropic neo-Hookean material may be expressed concisely in terms of the Cauchy stresses as [52]

$$\sigma_i^c = \lambda_i \frac{\partial W}{\partial \lambda_i} - \Pi, \tag{2.52}$$

with σ_i^c the Cauchy stress and Π the Lagrange multiplier. The principal Cauchy stresses are readily related to the principal nominal stresses σ_i

through

$$\sigma_i = \sigma_i^c / \lambda_i. \tag{2.53}$$

Now, in the pre-buckling regime deformations are spatially homogeneous, hence λ_i is constant and the principal directions $(\hat{\mathbf{e}}_1, \hat{\mathbf{e}}_2, \hat{\mathbf{e}}_3)$ coincide with the main axes $(\hat{\mathbf{e}}_x, \hat{\mathbf{e}}_y, \hat{\mathbf{e}}_z)$ for each material point in the beam. In that case, adopting $(\hat{\mathbf{e}}_x, \hat{\mathbf{e}}_y, \hat{\mathbf{e}}_z)$ as the new principal directions, λ_z simply relates to the vertical nominal strain ε_{zz} by

$$\lambda_z = 1 + \varepsilon_{zz}, \tag{2.54}$$

whereas Eq. (2.53) can be equally written as [52]

$$\sigma_{zz} = \sigma_z^c / \lambda_z. \tag{2.55}$$

Using these simplifications, the desired relation $\sigma_{zz}(\varepsilon_{zz})$ is readily obtained by calculating σ_z^c. Below we determine σ_z^c and distinguish between plane stress and plane strain conditions.

2.B.1 Plane stress

For plane stress conditions and free lateral expansion at the boundaries, the transverse stresses σ_x^c and σ_y^c must be zero. Therefore, evaluating Eq. (2.52) for the x and y component of the Cauchy stress provides us the constraint

$$\Pi = \frac{E}{3}\lambda_x^2 = \frac{E}{3}\lambda_y^2. \tag{2.56}$$

The above relation implies that $\lambda_x = \lambda_y$, as anticipated, and we proceed using λ_x as the independent stretch parameter. Having identified the constraint, the z component of the Cauchy stress follows as

$$\begin{aligned} \sigma_z^c &= \lambda_z \frac{\partial W}{\partial \lambda_z} - \Pi \\ &= \frac{E}{3}\left(\lambda_z^2 - \lambda_x^2\right) \end{aligned} \tag{2.57}$$

To express σ_z^c solely in terms of λ_z we combine the incompressibility condition $\lambda_x \lambda_y \lambda_z = 1$ with the relation $\lambda_x = \lambda_y$, and obtain $\lambda_x^2 = \lambda_z^{-1}$, so that

$$\sigma_z^c = \frac{E}{3}\left(\lambda_z^2 - \lambda_z^{-1}\right). \tag{2.58}$$

Finally, using the relations in Eqs. (2.54-2.55), we can write

$$\sigma_{zz} = \frac{E}{3}\left(1 + \varepsilon_{zz} - \frac{1}{(1+\varepsilon_{zz})^2}\right), \tag{2.59}$$

which is the result as given by Eq. (2.10a). Expansion of the above equation for small ε_{zz} yields

$$\sigma_{zz}/E = \varepsilon_{zz} - \varepsilon_{zz}^2 + \mathcal{O}\left(\varepsilon_{zz}^3\right), \tag{2.60}$$

hence we conclude that $\eta = -1$ in the pre-buckling regime of beams under plane stress conditions.

2.B.2 Plane strain

In the plane stress case a beam has no deformations in the y-direction and no stresses in the x-direction, owing to the confinement in y-direction. Summarizing these conditions as $\sigma_x^c = 0$ and $\lambda_y = 1$, we identify the constraint as

$$\Pi = \lambda_x \frac{\partial W}{\partial \lambda_x}. \tag{2.61}$$

Therefore, the z component of the Cauchy stress equals

$$\begin{aligned} \sigma_z^c &= \lambda_z \frac{\partial W}{\partial \lambda_z} - \lambda_x \frac{\partial W}{\partial \lambda_x} \\ &= \frac{E}{3}\left(\lambda_z^2 - \lambda_x^2\right) \end{aligned} \tag{2.62}$$

To express σ_z^c solely in terms of λ_z we combine the incompressibility condition $\lambda_x\lambda_y\lambda_z = 1$ with the condition $\lambda_y = 1$, and obtain $\lambda_x = \lambda_z^{-1}$, so that

$$\sigma_z^c = \frac{E}{3}\left(\lambda_z^2 - \lambda_z^{-2}\right). \tag{2.63}$$

Following section 2.B.1, the above equation can be converted in terms of nominal stress and strain as

$$\sigma_{zz} = \frac{E}{3}\left(1 + \varepsilon_{zz} - \frac{1}{(1+\varepsilon_{zz})^3}\right). \tag{2.64}$$

Note that the only difference with the result for plane stress in Eq. (2.59) is the exponent of the most right term. This exponent equals 3 for plane strain, but 2 for plane stress. Finally, expansion of Eq. (2.64) for small ε_{zz} yields

$$\sigma_{zz}/E = \frac{4}{3}\varepsilon_{zz} - 2\varepsilon_{zz}^2 + \mathcal{O}\left(\varepsilon_{zz}^3\right), \tag{2.65}$$

where the factor of $4/3$ in front of ε_{zz} is introduced by the plane strain assumption — a beam supported on both sides is stiffer by a factor $1/(1-\nu^2)$ [2]. Defining an effective Young's modulus $E' = E/(1-\nu^2)$, the result in Eq. (2.66) can be rewritten as

$$\sigma_{zz}/E' = \varepsilon_{zz} - \frac{3}{2}\varepsilon_{zz}^2 + \mathcal{O}\left(\varepsilon_{zz}^3\right), \tag{2.66}$$

from which we conclude that $\eta = -3/2$ in the pre-buckling regime of beams under plane strain conditions.

3

Excess zero modes in metamaterials with symmetries

We study the excess zero modes that arise for randomly diluted collections of rigid quadrilaterals, linked by flexible hinges at their tips. For full filling (no quads removed), large systems built from generic quads are rigid. In contrast, large symmetric systems featuring regular, identical squares possess one zero mode [1, 20], irrespective of size. Here we reveal the surprising finding that the number of such excess zero modes can become larger than one in systems where quads are randomly removed, demonstrating the existence of excess zero modes beyond a global hinging mode. Specifically, we show that the average number of excess modes for a large ensemble of randomly diluted systems, $\langle \Delta \rangle$, exceeds one and displays a peak with the fraction of removed quads, ρ, which consistently grows with the system size N. Interestingly, $\langle \Delta \rangle (\rho, N)$ exhibits finite size scaling with simple mean field exponents, suggesting the number of excess modes is an intrinsic quantity, and we obtain similar results for random bond (hinge) removal. Finally, we study the distribution of excess zero modes near the peak and design extreme geometries whose density of zero modes is six times larger than the peak average.

A paper based on the work presented in this chapter is in preparation for submission to Phys. Rev. Lett. as:

L.A. Lubbers and M. van Hecke, *Excess floppy modes in metamaterials with symmetries.*

3.1 Introduction

Collections of stiff elements connected by flexible hinges form a basis model for a wide range of systems, including engineering structures, complex materials and mechanical metamaterials. Depending on the multitude and geometry of links between the elements, such structures can be either floppy or rigid. Here we introduce counting arguments, that, by comparing the number of degrees of freedom and the number of constraints, determine the rigidity of such systems. We start by introducing Maxwell counting, and then show that this simple approach is not sufficient to determine the number of zero modes, due to the potential presence of states of self-stress.

3.1.1 Maxwell counting

In 1864 Maxwell laid the foundation for determining the rigidity of frames [51]. He geometrically described a frame as a system consisting of sites (points) that are connected by bonds (lines). When the sites are connected by a sufficient amount of bonds, the frame becomes rigid and no site(s) can be displaced without stretching or compression of bonds. When the sites are connected by too few bonds, however, the structure features zero modes, which are zero energy deformations that do not stretch bonds. A simple estimate of the relation between the number of sites N_s, bonds N_b and zero modes n_{m} in d dimensions, is given by the Maxwell count, and

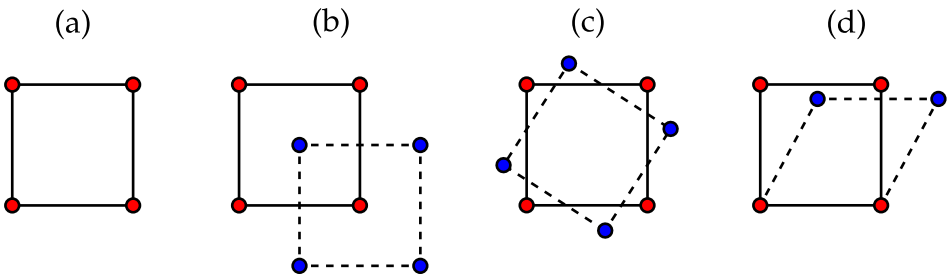

Figure 3.1: Sites, bonds and zero modes. (a) A square frame built from sites (filled circles) and bonds (black lines) has 4 zero modes ($n_m = 4$). (b-c) Trivial zero modes. Panel (b) shows global translation and panel (c) shows global rotation. (d) Internal zero mode.

reads

$$dN_s - N_b = n_m. \tag{3.1}$$

Here, the term dN_s represents the total number of degrees of freedom of the (unconnected) sites, tantamount to d independent translational degrees of freedom per site. The second term equals the number of constraints and is simply equal to N_b. Hence, the Maxwell count can physically be interpreted as a balance between the total number of degrees of freedom and constraints in the system, whose difference yields the number of zero modes.

We now exemplify the Maxwell count for the two-dimensional frame depicted in Fig. 3.1(a), which consists of $N_b = 4$ bonds and $N_s = 4$ sites. Applying Eq. (3.1) using $d = 2$ we find that the frame attains $n_m = 2 \times 4 - 4 = 4$ zero modes. Of these, three are trivial zero modes associated with global translations and rotations [Fig. 3.1(b-c)]. The remaining zero mode is shown in Fig. 3.1(d), and involves internal displacements of the sites. Hence, when focusing on internal zero modes, we exclude the $d(d+1)/2$ global zero modes, and rewrite the Maxwell criterium as

$$dN_s - N_b = n_m^i + \frac{d\,(d+1)}{2}, \tag{3.2}$$

where n_m^i are the internal zero modes. A frame is called stiff when $n_m^i = 0$. Internal zero modes that allow for finite-amplitude displacements of the sites are also called mechanisms, in contrast to infinitesmall zero modes where changes in the energy are at most quartic in the displacement amplitude.

We now present examples that show that Maxwell counting is not exact. To do so, we add diagonal bonds to the square frame, as shown in Fig. 3.2. First, for a single diagonal bond [panel (a)] the frame becomes stiff and we anticipate $n_m^i = 0$. Indeed, Eq. (3.2) confirms that $n_m^i = 2 \times 4 - 5 - 3 = 0$, and Maxwell's rule applies. For a second diagonal bond [panel (b)], we still anticipate $n_m^i = 0$, but the Maxwell count would predict $n_m^i = -1$. This inconsistency is caused by the second diagonal bond, which is redundant, and not needed for the rigidity of the square frame. Redundant bonds introduce so called states of self-stress in the system, which are combinations of tensions and compressions on the bonds that result in a zero net force on all sites. The combination of

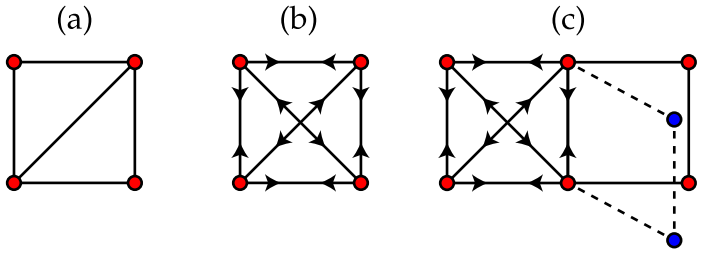

Figure 3.2: States of self-stress. (a) A square frame with a single diagonal bond is isostatic ($n_m^i = n_{ss} = 0$). (b) For two diagonal bonds, the square frame exhibits a single state of self-stress ($n_m^i = 0, n_{ss} = 1$), as indicated by the arrowheads. (c) Frame with one state of self-stress and one internal zero mode ($n_m^i = 1, n_{ss} = 1$).

such tensions and compressions that compose the (single) state of self-stress for the frame in panel (b), is visualized by the black arrows. In this state of self-stress, side bonds are placed under compression and diagonal bonds under tension. In order to accurately predict n_m^i for frames holding redundant bonds, or rather holding n_{ss} self-stresses, a modified criterium that takes into account these self-stresses is necessary. This modified criterium is known as the generalized Maxwell equation, and is given by

$$dN_s - N_b = n_m^i + \frac{d\,(d+1)}{2} - n_{ss}. \tag{3.3}$$

Note that Eq. (3.3) indeed predicts $n_m^i = 0$ for the frame in panel (b) for $n_{ss} = 1$. Frames that neither attain internal zero modes nor have any states of self-stress are called isostatic ($n_m^i = n_{ss} = 0$). Hence, a square frame with a single diagonal is isostatic, but a square frame with two diagonals is not. Finally, we illustrate the generalized Maxwell relation for a more complicated frame, which is shown in Fig. 3.2(c). This frame can be regarded as a combination of an over-constrained region (left square frame) and a floppy region (right square frame), and consequently has $n_m^i = 1$ and $n_{ss} = 1$. Based on the global number of sites and bonds, Eq. (3.3) predicts $n_m^i - n_{ss} = 0$, which demonstrates that the generalized Maxwell equation holds.

3.1.2 This chapter

In this chapter, we study systems that consist of quadrilaterals (quads) linked by flexible hinges at their tips. We will consider and compare generic systems, consisting of irregular quads, to symmetric systems, consisting of identical squares (regular quads). A special property of symmetric systems —which plays a central role in this chapter— is that these systems always feature a hinging zero mode, even for full filling (no squares removed), and independent of the system size. This is not necessarily true for generic systems, as we will demonstrate now by applying the generalized Maxwell count to $N_x \times N_y$ lattices of quads.

To set up the counting argument we need the following two ingredients. First, a single quad has 3 degrees of freedom, namely two translational and one rotational. Second, every hinge, or bond, is equivalent to two constraints. This is most easily understood by considering two separate quads: Their translational degrees of freedom couple when joining any pair of tips, effectively reducing the degrees of freedom by two. Taking these considerations into account, a system of $N_x \times N_y$ squares has a total of $3N_xN_y$ degrees of freedom and $N_x\left(N_y-1\right)+N_y\left(N_x-1\right)$ bonds, equivalent to $4N_xN_y-2\left(N_x+N_y\right)$ constraints. Adapting the generalized Maxwell count as given in Eq. (3.3) to the context of quads, we obtain

$$n_m^i - n_{ss} = -N_xN_y + 2\left(N_x+N_y\right) - 3, \tag{3.4}$$

where we note that the above equation holds for generic and symmetric systems. Now, if the balance $n_m^i - n_{ss}$ exceeds zero the system must have internal zero modes. If $n_m^i - n_{ss} \leq 0$, the system might attain zero modes, depending on the number of states of self-stress. Using N_y as the control parameter, we have evaluated Eq. (3.4) for several values of N_y and tabulated the results in Table 3.1. We now discuss the implications of

N_y	$n_m^i - n_{ss}$
1	$N_x - 1$
2	1
3	$3 - N_x$

Table 3.1: Eq. (3.4) evaluated for $N_y = 1,2,3$.

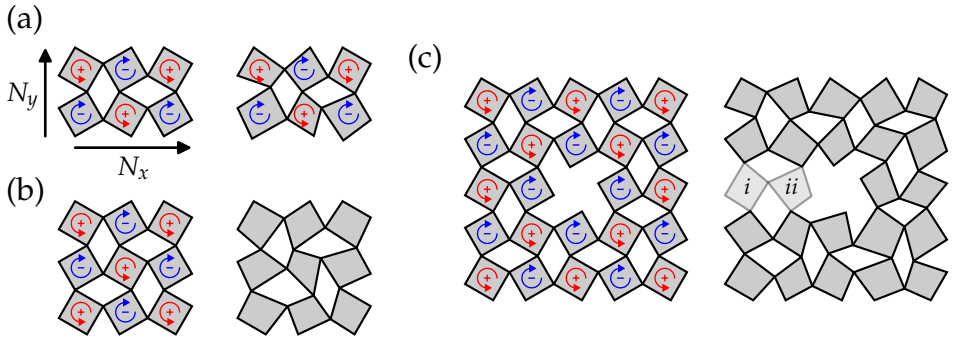

Figure 3.3: Rigidity of strips, 3×3 clusters and looped-strips. (a-c) In each panel, we compare symmetric (left) and generic (right) systems. The coloured arrows indicate a global hinging mode, in which quads collectively counter rotate. (a) Strips always attain a global hinging mode, both in the generic and symmetric case ($n_s = n_g = 1$). (b-c) In contrast, 3×3 clusters (b) or looped-strips (c) only attain a global hinging zero mode when the system is symmetric ($n_s = 1, n_g = 0$). Note that one recovers an ordinary strip ($n_s = n_g = 1$) by the removal of quads *i* and *ii* (illustrated by their lower opacity).

this table for the rigidity of the three basic geometries shown in Fig. 3.3, which will be encountered frequently throughout this chapter.

> In the remainder of this thesis, we make a clear distinction between n_m^i for symmetric and generic systems. We will denote n_m^i associated with symmetric systems as n_s, and n_m^i associated with generic systems as n_g.

Strips [Fig. 3.3(a)]. — From Table 3.1 we infer that $1\times N_x$ and $2\times N_x$ strips are always floppy, as the balance $n_m^i - n_{ss}$ is positive. Moreover, since these strips have no states of self-stress, the number of zero modes for generic and symmetric strips are equal. For $N_y = 1$, the number of zero modes increases with N_x as $n_s = n_g = N_x - 1$. Interestingly, for $N_y = 2$, strips exhibit a single zero mode ($n_s = n_g = 1$), independently of N_x. This internal zero mode is characterized by the hinging motion of quads, as depicted by the coloured arrows in Fig. 3.3(a). This hinging mode will be described in more detail in section 3.2.2.

Clusters of size 3×3 or larger [Fig. 3.3(b)]. — For $N_y = 3$ and $N_x \geq 3$, the balance $n_m^i - n_{ss}$ becomes less than or equal to 0. The system then

only can attain zero modes if a sufficient number of states of self-stress are present. Let us first inspect $N_x = 3$. Here, $n_m^i - n_{ss} = 0$, and for generic clusters both n_g and n_{ss} are zero — the system is isostatic. In contrast, for symmetric clusters, there is always one hinging mode, and n_s equals one, implying that the system also has a state of self-stress. For generic clusters, with $N_x > 3$ and $N_y = 3$, we have $n_g = 0$, $n_{ss} = N_x - 3$; for symmetric clusters of the same size, $n_s = 1$, $n_{ss} = N_x - 2$. More generally, the outcome $n_s = 1$ and $n_g = 0$ persists irrespective of the cluster size, provided $N_x, N_y \geq 3$. This suggests that symmetric clusters attain extra states of self-stress in comparison to generic clusters in order to maintain the balance $n_m^i - n_{ss}$ for a given system.

Looped strips [Fig. 3.3(c)]. — As a third geometry, we consider looped-strips. Their rigidity is most easily understood by regarding it as a strip whose head and tail are connected by two extra bonds. Let us first consider the case before quadrilaterals *i* and *ii* are present; then, $n_s = n_g = 1$ and $n_{ss} = 0$.

When we add quad *i* in the symmetric case, we add 3 degrees of freedom, as well as 4 constraints; since n_s remains 1, this implies we create one state of self-stress. Adding quad *ii* then adds 3 degrees of freedom and 6 constraints; n_s remains one, and n_{ss} becomes 4. In the generic case, the solution is different. Consider the two corners of the quads that would connect to quad *i*. In the generic case, their motions are not correlated, and their distance will be variable. Hence, connecting these corners with quad *i*, the system becomes rigid — $n_g = 0$ and the counting then specifies that $n_{ss} = 0$ as well. Adding quad *ii* then yields $n_g = 0$ and $n_{ss} = 3$.

The 3×3 (or larger) clusters and the looped-strips discussed above illustrate a general observation. For the generic case, strip-like configurations have $n_g = 1$ and $n_{ss} = 0$; think of the looped-strip without quads *i* and *ii*, but also of a 3×3 cluster with one corner removed. Once there is a loop, generic systems become rigid $(n_g = 0)$, but symmetric systems maintain their hinging mode $(n_s = 1)$, implying that these always feature additional states of self-stress. Moreover, loops and sufficiently large clusters thus induce differences between n_s of symmetric systems and n_g of generic systems.

3.2 System and methods

In this section we set up the mathematical description for (diluted) collections of rigid quads that are connected by flexible hinges, and review the basic ingredients of zero mode counting. In section 3.2.1 we present the mathematical framework which covers both symmetric systems featuring regular, identical squares, and generic systems featuring irregular quads. Furthermore, we discuss the procedure to construct stress-free generic systems by the application of small geometric perturbations to symmetric systems. In section 3.2.2 we distinguish two types of zero modes; mechanisms and quartic modes. Section 3.2.3 briefly reviews the standard technique used to count the number of zero modes of symmetric and generic systems. Finally, section 3.2.4 discusses how we choose the magnitude of the perturbations to properly count excess zero modes from numerical simulations.

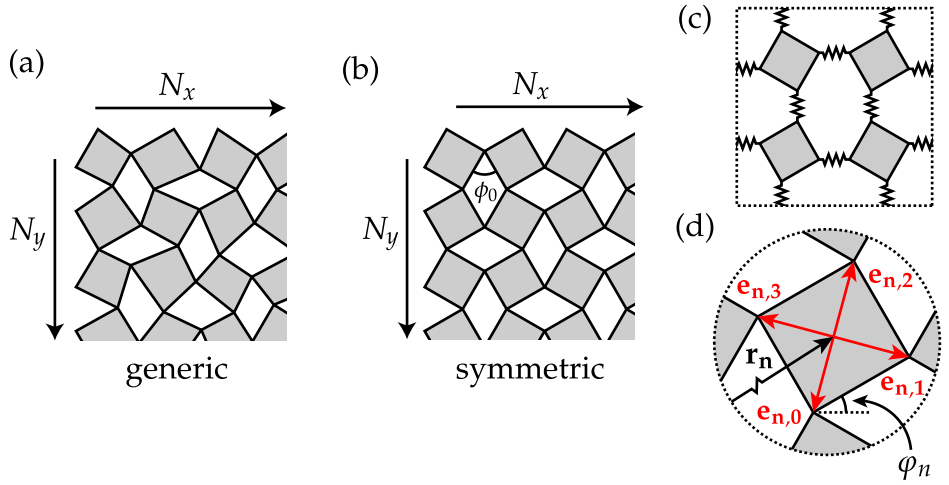

Figure 3.4: System definitions. (a) Generic and (b) symmetric systems of size $N_x \times N_y$. The opening angle between adjacent squares in symmetric systems is denoted ϕ_0. (c-d) Connectivity and quad description; these are shown for a symmetric system, but equally apply to generic systems. (c) Hinges are modelled by linear springs of zero rest length which connect the corners of adjacent quads. Upon relaxation of the springs, the quads' corners coincide. (d) The coordinate system used to describe the shape, position and orientation of individual quads (see main text).

3.2.1 Mathematical description

To study collections of rigid quads connected by flexible hinges, we model these systems as $N_x \times N_y$ lattices of rigid quads connected by springs of unit stiffness and zero rest length [Fig. 3.4]. Unless noted otherwise, we use open boundary conditions, motivated by the goal to obtain designs for finite-sized metamaterials. For full filling, our systems contain a total of $N_t = N_x N_y$ quads and $N_b = 2N_x N_y - (N_x + N_y)$ springs (bonds), where the non-extensive correction term $N_x + N_y$ stems from the missing bonds of the quads located at the boundaries. For very large systems, the number of bonds approaches $2N_x N_y \left[1 - (N_x + N_y)/(2N_x N_y)\right] \approx 2N_x N_y$, indicating that each quad is connected to 4 neighbouring quads. Note that the terms hinges, springs and bonds are used synonymously in this thesis — these terms should all be interpreted similarly.

Quad description and state vector. — To mathematically describe our systems, we assign each of the $N_x N_y$ quads a label, n, along with a centre location $\mathbf{r_n} = (x_n, y_n)$, a rotation angle φ_n, and the centre-to-corner vectors $\mathbf{e_{n,i}}$ $(i = 0,1,2,3,4)$ [see Fig. 3.4(d)]. Note that $\mathbf{e_{n,i}}$ therefore specifies the shape of each quad.

Quads are modelled as rigid objects, implying that their shape remains fixed when the system is deformed. In contrast, $\mathbf{r_n}$ and ϕ_n might change for a given deformation. Having prescribed the shape of the quads, we can therefore fully characterize our systems by the state vector

$$\mathbf{X} = (x_1, y_1, \varphi_1, x_2, y_2, \varphi_2, ...x_N, y_N, \varphi_N)^T, \tag{3.5}$$

which is a $3N \times 1$ vector providing the centre location and rotation angle of each quad.

To build symmetric systems, we use squares of side length 1, which are described by perpendicular centre-to-corner vectors $(\mathbf{e_{n,i}} \perp \mathbf{e_{n,i+1}})$ of magnitude $\sqrt{2}/2$. The centres of the squares are then stacked on a square-like, two-dimensional grid, such that the corners of adjacent squares coincide, as in Fig. 3.4(b). Note that the grid spacing controls the opening angle ϕ_0 between adjacent squares, which is related to the rotation angle of a single square as $\varphi_n = \pm\phi_0/2$. Here, the sign of φ_n depends on the alternating counter or clockwise rotation of quad n. The procedure to build generic systems is different. In these disordered systems, the shape and

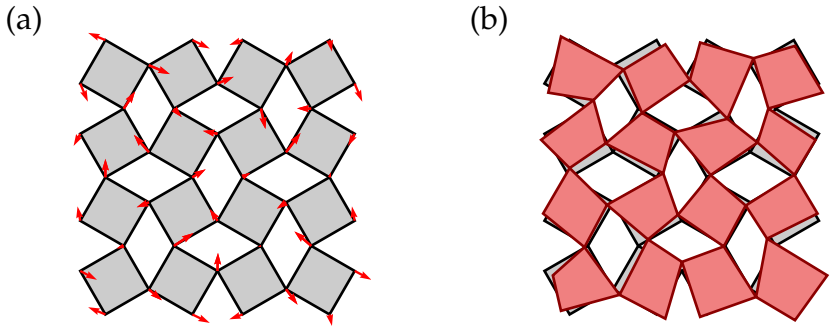

Figure 3.5: Procedure to construct stress-free, generic systems. (a) Starting from a symmetric system, we randomly displace connected corners by a random vector $\mathbf{\Delta e_{n,i}}$, as visualized by the red arrows. Here we have used $\epsilon = 0.3$ and to enhance visualization the magnitude of the resulting vectors is shown at 200%. (b) The resulting generic system (red), superimposed on the symmetric system.

orientation of quads is arbitrary and the corners of adjacent quads generally do not coincide. In the paragraph hereafter we will motivate and discuss the procedure to construct arbitrary generic systems for which the corners of adjacent quads exactly coincide [e.g. as in Fig. 3.4(d)].

Generic, stress-free systems. — We now discuss the procedure to construct stress-free generic systems. In such systems, the corners of adjacent quads coincide and the springs are not pre-stressed. The design of such systems is motivated by the significant simplification of the mode counting analysis described in section 3.2.3. Stress-free systems allow for the random removal of quads while retaining equilibrium, but if pre-stresses would be present, quad removal could initiate the relaxation to a lower energy state. This would require the calculation of intermediate equilibrium configurations with the aid of computationally time-consuming conjugate gradient techniques — stress-free systems circumvent the need for such techniques. Note that, as mentioned already, symmetric systems are automatically stress-free due to the non-generic nature of the squares.

To construct the stress-free, generic systems we systematically perturb symmetric systems by randomly displacing connected corners, as is illustrated in Fig. 3.5. This procedure stretches no springs and thus ensures no pre-stresses develop when changing the squares to irregular quads.

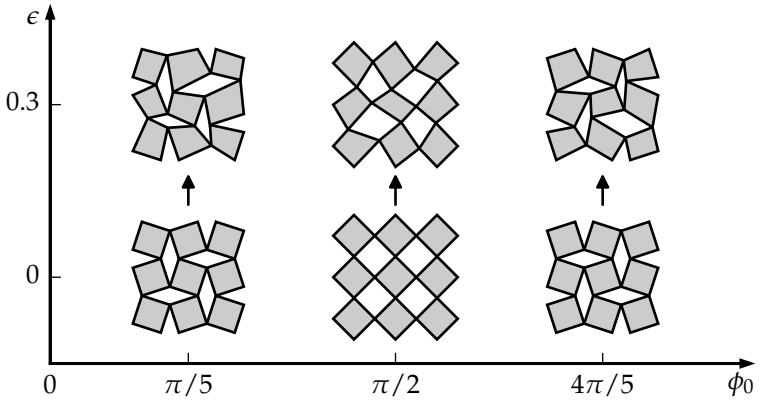

Figure 3.6: Stress-free, generic systems obtained by perturbing symmetric systems with magnitude ϵ, for a range of symmetric opening angles. Note that the top systems do not feature zero modes.

To quantify the magnitude and direction of the random displacements, we use the random vectors $\mathbf{\Delta e_{n,i}} = \left(\epsilon_x, \epsilon_y\right)^T \|\mathbf{e_{n,i}}\|$ (red arrows in Fig. 3.5). The centre-to-corner vectors of the perturbed generic quads then readily follow from the vectorial sum $\mathbf{e'_{n,i}} = \mathbf{e_{n,i}} + \mathbf{\Delta e_{n,i}}$, where we note that $\mathbf{e_{n,i}}$ is associated with the initial symmetric system. Furthermore, ϵ_x and ϵ_y represent random numbers sampled from a uniform probability distribution that lie within the interval $[-\epsilon, \epsilon]$. In the following section we will demonstrate that $\epsilon = 0.1$ is a suitable choice to detect excess zero modes (the modes that only occur in symmetric systems). Finally, Fig. 3.6 shows some more examples of generic systems, obtained by perturbing symmetric systems of different opening angles. In the remainder of this work we utilize the technique as described here to construct stress-free, generic systems.

The energy of the system, E. — The systems introduced in Fig. 3.4 contain N_b springs of unit stiffness and rest length zero. This yields the following expression for the total energy of a system

$$E\left(\mathbf{X}\right) = \frac{1}{2} \sum_{s=1}^{N_b} \ell_s \left(\mathbf{X}\right)^2, \tag{3.6}$$

with ℓ_s the length of spring s. As mentioned before, for fully filled systems (no quads removed), $N_b = 2N_xN_y - (N_x + N_y)$, but this number will be lower in diluted systems. More importantly, it should be noted that the springs lengths are a function of the state vector $\mathbf{X}$; for the undeformed symmetric and (stress-free) generic systems no springs are stretched, hence $E(\mathbf{X}) = 0$. When applying a deformation $\mathbf{X}$ changes and E might change as well. For deformations associated with a zero mode, $E(\mathbf{X})$ remains unchanged up to quadratic order. In contrast, applying deformations that are not associated with zero modes lead to a quadratic increase of $E(\mathbf{X})$. The actual ℓ_s that correspond to a given $\mathbf{X}$ are calculated numerically by subtracting the corner positions of adjacent quads, which are easily calculated by combining $\mathbf{e_{n,i}}$ with $\mathbf{X}$. In section 3.2.3 we will use $E(\mathbf{X})$ to construct the Hessian matrix, which forms the basis of counting zero modes.

3.2.2 Finite amplitude and quartic modes

The zero modes we encounter in this work can be subdivided in two types of zero modes: Finite amplitude mechanisms and quartic modes. A mechanism is a 'finite' zero mode in which finite-amplitude displacements of quadrilaterals stretch no springs. A quartic mode is an infinitesimal zero mode in which spring lengths do not change to first order in the magnitude of quadrilateral displacements, $\mathbf{\Delta X}$, but do so to second order. In the latter case, the energy changes with the quadrilateral displacements as $\mathbf{\Delta X}^4$, hence the name quartic mode. Below we provide examples of a mechanism and quartic mode.

Global hinging. — The mechanism we focus on in this paragraph – global hinging– occurs for arbitrary large symmetric systems with open boundary conditions. For symmetric systems, the centre coordinates of the squares compose a square lattice, thereby allowing for a collective counter rotating motion of the squares without stretching bonds. This collective motion is illustrated in Fig. 3.7(a), using $\phi_0 \in [0, \pi]$ as the control parameter. From these snapshots we observe a non-monotonic unfolding of the tiling for increasing ϕ_0: Starting from a nearly closed system ($\phi_0 = \pi/20$), the system unfolds to maximum opening ($\phi_0 = \pi/2$), and then shrinks again towards the nearly closed system ($\phi_0 = 19\pi/20$). Since this

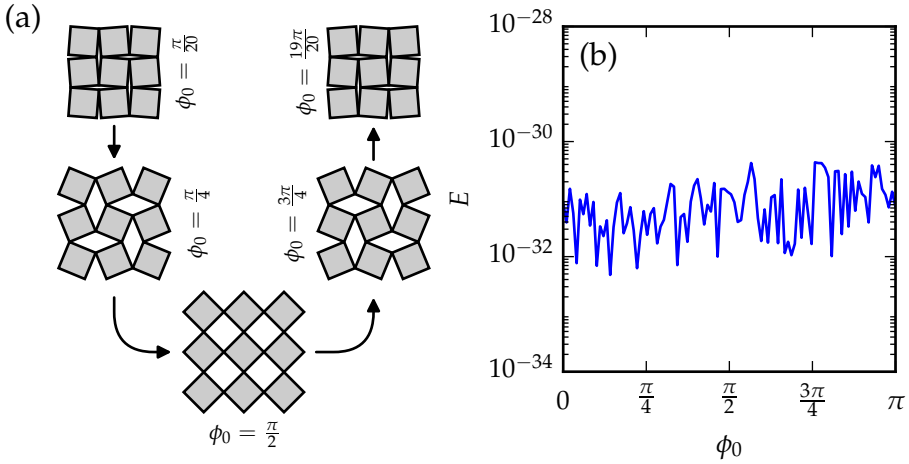

Figure 3.7: Global hinging mode in a symmetric 3×3 system. In this mode the opening angle ϕ_0 can be varied over a finite amplitude without stretching the bonds. (a) Subsequent snapshots of the tiling when varying ϕ_0 from $\pi/20$ to $19\pi/20$. Note that the hinging behaviour for $\phi_0 < \pi/2$ and $\phi_0 > \pi/2$ is related by symmetry. (b) The numerically obtained energy as function of the opening angle ϕ_0.

collective motion of squares relies on hinging and involves a global shape change, we refer to this mode as *global hinging*.

To confirm that no springs are stretched during the global hinging, we have plotted the energy as function of ϕ_0 in Fig. 3.7(b). The energy remains zero (within numerical precision) over the complete range of ϕ_0, and thus reflects that global hinging of symmetric systems is a mechanism.

Finally, we anticipate that the global hinging mode ceases to exist for generic systems, as the underlying square lattice becomes distorted for finite ϵ. This will be confirmed in section 3.2.4, in which we reveal the energy increase of the global hinging mode with ϵ.

Quartic and finite energy modes. — In Fig. 3.8(a) we display an example of spurious quartic modes that occur in symmetric systems with opening angle $\phi_0 = \pi/2$. Due to the symmetry that arises at this opening angle, the two centre squares can undergo a counter rotating motion while the vertical distance y_q is preserved to leading order in the side-

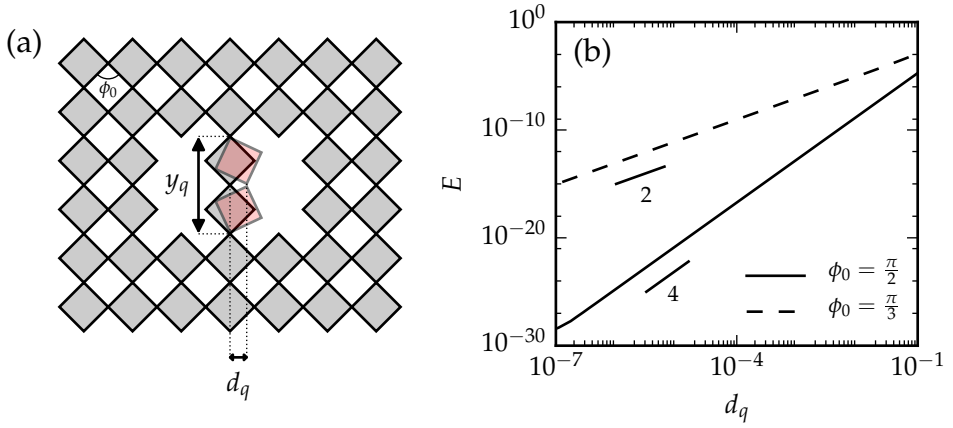

Figure 3.8: Quartic modes in symmetric systems. (a) For $\phi_0 = \pi/2$ the two centre squares can deflect to the right (coloured red), or equally to the left (not shown), while y_q is preserved to leading order in the sidewards deflection d_q. (b) The energy change of this mode as function d_q shows clear powerlaw behaviour with exponent 4 for $\phi_0 = \pi/2$ (solid line), and exponent 2 for $\phi_0 = \pi/3$ (dashed line).

wards deflection d_q. The energy change associated with d_q is plotted in Fig. 3.8(b) (solid line) and shows clear powerlaw behaviour with exponent 4, confirming the zero mode is quartic in nature.

To suppress the spurious quartic modes, we set $\phi_0 = \pi/3$ in the remainder of this work. This (arbitrary) choice destroys the symmetry that arises in symmetric systems for $\phi_0 = \pi/2$ and kills the quartic modes related to this symmetry. This is verified by plotting the energy change associated with d_q for $\phi_0 = \pi/3$ in Fig. 3.8(b) (dashed line), which now shows powerlaw behaviour with exponent 2 rather than exponent 4. The exponent 2 demonstrates that the springs lengths are changing to first order in the magnitude of the quadrilateral displacements (here expressed as d_q) and this exponent is common for finite energy modes. Even though we kill quartic modes related to the opening angle ϕ_0 by setting $\phi_0 = \pi/3$, quartic modes originating from more complex symmetries, although rare, can still appear in diluted symmetric systems (see chapter 4 for examples). The appearance of these quartic modes is inevitable and in the remainder of this thesis we do not distinguish between mechanisms and quartic modes, unless explicitly noted otherwise.

3.2.3 Mode counting

We now discuss the technique to detect the number of zero modes and their spatial structure. For a given tiling in some reference state $\mathbf{X}$ [Eq. (3.5)], deformations associated with zero modes, $\Delta\mathbf{X}$, leave the energy E unchanged up to quadratic order in $\Delta\mathbf{X}$. To find all $\Delta\mathbf{X}$ that satisfy this criterium, the approach is to analytically expand the energy around state $\mathbf{X}$, which yields a matrix equation that can be numerically diagonalized.

Starting with the expansion of the energy in Eq. (3.6) about $\mathbf{X}$ up to quadratic order, we obtain

$$E(\mathbf{X}+\boldsymbol{\Delta}\mathbf{X}) = E(\mathbf{X}) + \boldsymbol{\Delta}\mathbf{X}^T \nabla E(\mathbf{X}) + \frac{1}{2}\boldsymbol{\Delta}\mathbf{X}^T \mathbf{H}(\mathbf{X})\,\boldsymbol{\Delta}\mathbf{X}, \tag{3.7}$$

with $\nabla E(\mathbf{X})$ the gradient and $\mathbf{H}(\mathbf{X})$ the Hessian matrix of the energy evaluated at $\mathbf{X}$. The gradient $\nabla E = \partial E/\partial \mathbf{X}$ is a $3N_xN_y \times 1$ vector that contains all first derivatives of the energy with respect to the quadrilateral positions and orientations,

$$\nabla E = \left[\frac{\partial E}{\partial x_1}, \quad \frac{\partial E}{\partial y_1}, \quad \frac{\partial E}{\partial \varphi_1}, \quad \ldots, \quad \frac{\partial E}{\partial \varphi_{N_t}}\right]^T. \tag{3.8}$$

The Hessian is a $3N_xN_y \times 3N_xN_y$ matrix that contains the second derivatives of the energy with respect to the entries of $\mathbf{X}$, which yields

$$\mathbf{H} = \begin{bmatrix} \frac{\partial^2 E}{\partial x_1^2} & \frac{\partial^2 E}{\partial x_1 \partial y_1} & \frac{\partial^2 E}{\partial x_1 \partial \varphi_1} & \cdots & \frac{\partial^2 E}{\partial x_1 \partial \varphi_{N_t}} \\ \frac{\partial^2 E}{\partial y_1 x_1} & \frac{\partial^2 E}{\partial^2 y_1} & \frac{\partial^2 E}{\partial y_1 \partial \varphi_1} & \cdots & \frac{\partial^2 E}{\partial y_1 \partial \varphi_{N_t}} \\ \frac{\partial^2 E}{\partial \varphi_1 \partial x_1} & \frac{\partial^2 E}{\partial \varphi_1 \partial y_1} & \frac{\partial^2 E}{\partial^2 \varphi_1} & \cdots & \frac{\partial^2 E}{\partial \varphi_1 \partial \varphi_{N_t}} \\ \vdots & \vdots & \vdots & \ddots & \vdots \\ \frac{\partial^2 E}{\partial x_{N_t} \partial x_1} & \frac{\partial^2 E}{\partial x_{N_t} \partial y_1} & \frac{\partial^2 E}{\partial x_{N_t} \partial \varphi_1} & \cdots & \frac{\partial^2 E}{\partial x_{N_t} \partial \varphi_{N_t}} \end{bmatrix}. \tag{3.9}$$

The entries of the gradient and Hessian matrix are complicated functions of the quadrilateral corner coordinates $(x_{n,i}, y_{n,i})$ and the rotation angle φ_n, but can be fully determined analytically. For a detailed analytical derivation of the gradient and Hessian matrix for the systems considered in this work, we refer to appendices 3.A and 3.B.

The expansion of the energy in Eq. (3.7) can be simplified as follows. First, we focus on systems in the absence of external forces for which $\mathbf{X}$ is an equilibrium configuration satisfying $\nabla E(\mathbf{X}) = \mathbf{0}$. As such, the second term on the right hand side of Eq. (3.7) drops out. Second, due to the procedure described in section 3.2.1 systems are free of internal stresses, hence $E(\mathbf{X}) = 0$ and the first term on the right hand side drops out as well. Note that this stress-free condition also ensures the gradient $\nabla E(\mathbf{X})$ remains zero when quadrilaterals are removed. Taking both simplifications into account, the expansion [Eq. (3.7)] turns into

$$E(\mathbf{X} + \Delta\mathbf{X}) = \frac{1}{2}\Delta\mathbf{X}^T\mathbf{H}(\mathbf{X})\Delta\mathbf{X}. \tag{3.10}$$

Then, to find all non-trivial $\Delta\mathbf{X}$ for which the right hand side of Eq. (3.10) is zero, we consider the eigenvectors and associated eigenvalues of the matrix $\mathbf{H}$. Any of such eigenvectors $\Delta\mathbf{X}_{\boldsymbol{\lambda}}$ has the special property to preserve direction when multiplied by $\mathbf{H}$, but to be multiplied by a scalar λ, the associated eigenvalue [123]. More formally, $\mathbf{H}(\mathbf{X})\Delta\mathbf{X}_{\boldsymbol{\lambda}} = \lambda\Delta\mathbf{X}_{\boldsymbol{\lambda}}$, and substitution in Eq. (3.10) yields

$$E(\mathbf{X} + \Delta\mathbf{X}_{\boldsymbol{\lambda}}) = \frac{1}{2}\lambda\|\Delta\mathbf{X}_{\boldsymbol{\lambda}}\|^2, \tag{3.11}$$

which demonstrates that for $\lambda = 0$ the energy is unaltered under a deformation $\Delta\mathbf{X}_{\boldsymbol{\lambda}}$. Hence, eigenvectors with associated eigenvalue $\lambda = 0$ are zero modes. While the Hessian can be determined analytically, the $3N_xN_y$ eigenvalues and eigenvectors need to be determined numerically. In our numerics (double precision) a zero mode typically has $\lambda = \mathcal{O}(10^{-16})$, which is sufficient to distinguish zero modes from finite-energy modes. We will elaborate in more detail on this aspect in the following section.

3.2.4 Magnitude of ϵ and numerical zero modes

For systems consisting of perfect squares, there is a global hinging zero mode (section 3.2.2) — in generic systems consisting of perturbed quadrilaterals, this mode attains a finite energy, and should not be counted as

a zero mode. Once we dilute these systems, new zero modes can arise. In this section we describe how we numerically distinguish zero modes from finite energy modes. In particular we motivate our choice for the magnitude of the perturbations in generic systems and the criterium we use to distinguish zero from non-zero eigenvalues. We show that perturbations with magnitude $\epsilon = 0.1$ and a cut-off criterium for the eigenvalues $\lambda_c = 10^{-10}$ suffice to unambiguously detect the zero modes of both generic and symmetric systems. In the remainder of this section we use $N_x = N_y = 10$ to exemplify our choices.

We now first elaborate on our choice for the magnitude of ϵ. To this end, we determine the eigenvalues of fully-filled, generic systems when varying ϵ over 8 orders of magnitude. We present results using a single simulation per value of ϵ, because we found (from comparison of multiple simulations per ϵ) that their outcome exhibits only very minor scatter (not shown here). Using single simulations for each ϵ, we have visualized the eigenvalues as function of ϵ in Fig. 3.9(a). From this plot we observe that for each value of ϵ, there exists a cluster of eigenvalues with λ of order 1, there are 3 eigenvalues of order 10^{-15}, and in between there is a single eigenvalue, λ_h, whose value exhibits power law behaviour: $\lambda_\mathrm{h} \sim \epsilon^2$. The scaling exponent 2 is very robust and does not depend on the particular value $\phi_0 = \pi/3$ chosen here, but holds for any opening angle within the accessible range.

In terms of eigenmodes, the clusters of eigenvalues at the top are associated with finite energy eigenmodes, while the eigenvalues at the bottom are associated with the three trivial, global eigenmodes of the systems: x-translation, y-translation and rotation. The eigenvalue λ_h arises from the global hinging mode and becomes increasingly smaller as the perturbations decrease. Note that this is what one would expect, since the centre locations of the quadrilaterals converge towards a perfect square lattice for decreasing ϵ. Therefore, the global hinging motion becomes increasingly 'softer' and eventually λ_h becomes of the same order as the eigenvalues associated with the three trivial eigenmodes. Furthermore, the scaling between λ_h and ϵ with exponent 2 can quantitatively be understood by noticing that quadrilateral rotations in generic systems, that arise due to global hinging, involve changes in spring length of order ϵ. Hence, the corresponding change in energy scales as ϵ^2, implying that $\lambda_h \sim \epsilon^2$ by Eq. (3.11).

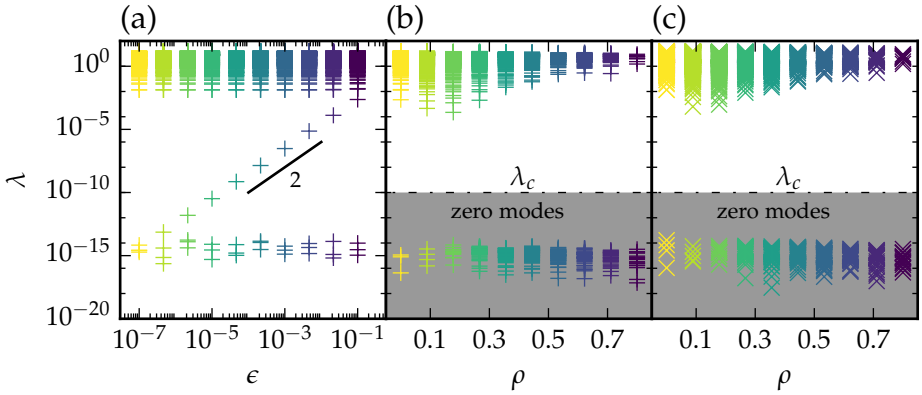

Figure 3.9: Eigenvalues of the Hessian for $N_x = N_y = 10$ and $\phi_0 = \pi/3$. (a) For a fully-filled, generic system, we plot the eigenvalues for varying ϵ. Each color shows the distribution of the $3N_xN_y$ eigenvalues that belong to a given ϵ. (b-c) Eigenvalues for diluted systems as function of the cutting fraction ρ. Here, each colour is associated with the eigenvalues that belong to a given ρ. We consider eigenvalues smaller than $\lambda_c < 10^{-10}$ as zero modes, indicated by the shaded regions. In (b) we show results for generic systems ($\epsilon = 0.1$) and in (c) for symmetric systems ($\epsilon = 0$).

The trivial eigenmodes —global translations or rotation— involve no energy penalty, allowing us to infer from Fig. 3.9(a) that our numerical precision for a zero mode is of order 10^{-15}. Hence, to ensure that the hinging mode attains a finite energy in generic systems, and is not counted as a zero mode, we pick ϵ such that λ_h in generic systems remains orders of magnitude separated from the order 10^{-15}. Therefore, we set $\epsilon = 0.1$ in the remainder of this work. The resulting clear separation in eigenvalues of zero modes versus finite-energy modes occurring for $\epsilon = 0.1$ allows us to define a critical eigenvalue λ_c in order to count the number of zero modes. Using λ_c as a cut-off criterium, we count eigenvalues below λ_c as zero modes, but eigenvalues above λ_c as finite energy modes. Fig. 3.9(a) illustrates that $\lambda_c = 10^{-10}$ is suitable for systems of full filling.

We conclude this section by showing that this cut-off approach remains valid for diluted systems. To study the distribution of eigenvalues in diluted systems, we randomly remove $N_r = \rho N$ quadrilaterals and determine the eigenvalues of the remaining system. We use a single simulation per value of ρ, because we found that, similar to the eigenvalue

study for varying ϵ, eigenvalues exhibit only minor scatter for random dilution (not shown here). In Fig. 3.9(b-c) we have plotted the eigenvalues as function of the cutting fraction ρ using a single simulation per value of ρ, both for generic (panel b) and non-generic systems (panel c). This demonstrates that for increasing ρ new zero modes start to appear, and more importantly, that the clear separation in eigenvalues of zero and finite-energy modes persists over the range of ρ. Hence, $\lambda_c = 10^{-10}$ is also a valid cut-off criterium for diluted systems. In summary, we have motivated the choices $\epsilon = 0.1$ and $\lambda_c = 10^{-10}$ to distinguish true zero modes from finite energy modes, and in the remainder of this work we will use these values.

3.3 Random quad removal

In this section we determine the number of zero modes in generic (n_g) and symmetric (n_s) systems for random quad removal. In section 3.3.1 we present the phenomenology of random quad removal, demonstrate that n_s can exceed n_g, and present the spatial structure of such excess zero modes. In section 3.3.2 we fully characterize the number of excess zero modes as function of system size and the fraction of removed quads, and show that the mean number of excess zero modes exhibits finite size scaling with mean field exponents.

In what follows we consider systems of square periphery and initial full-filling, that is $N_x = N_y = N$ with a total number of N^2 quads. Furthermore, we use the parameter values $\phi_0 = \pi/3$, $\epsilon = 0.1$ and $\lambda_c = 10^{-10}$, as motivated in section 3.2.

3.3.1 Phenomenology

This section presents the phenomenology of random quad removal. To dilute symmetric and generic systems, we randomly remove $N_r = \rho N^2$ quads, where ρ denotes the fraction of removed quads.

Starting with fully filled systems of size $N = 10$, we track the number of zero modes in generic (n_g) and symmetric (n_s) systems for the subsequent removal of quads, when using the same ensemble of dilution patterns for both. In Fig. 3.10(a-b) we show the outcome of n_s and n_g, and their ensembles averages $\langle n_s \rangle$ and $\langle n_g \rangle$, as function of the cutting fraction

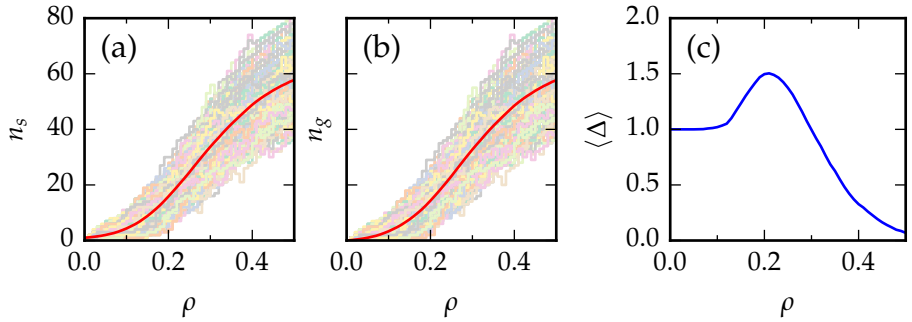

Figure 3.10: Random quad removal in 10×10 systems. (a-b) The number of zero modes in symmetric (n_s) and generic (n_g) systems as function of the cutting fraction ρ. Each panel displays the outcome of 10^3 independent cutting sequences (curves of low brightness) along with the ensemble averages $\langle n_s \rangle$ and $\langle n_g \rangle$ (red curves of high brightness). (c) Subtracting $\langle n_g \rangle$ from $\langle n_s \rangle$ yields the average number of excess zero modes, $\langle \Delta \rangle$.

ρ, for 10^3 independent cutting sequences. As can be observed, n_s and n_g generally increase with ρ, but might incidentally decrease [see lower curves in Fig. 3.10(a-b)] when a quad associated with a given zero mode is removed — a simple example being a quad that is only connected at one corner. The growth of the ensemble averages $\langle n_s \rangle$ and $\langle n_g \rangle$ [solid red curves in Fig. 3.10(a-b)] appear nearly identical, and to reveal differences between symmetric and generic systems we introduce

$$\langle \Delta \rangle = \langle n_s - n_g \rangle. \tag{3.12}$$

This quantity corresponds to the number of extra zero modes that exist in symmetric, but not in generic systems, due to the non-generic nature of the squares. Therefore, we refer to Δ as the number of *excess zero modes*. Interestingly, $\langle \Delta \rangle (\rho)$ [Fig. 3.10(c)], reveals subtle but important differences between symmetric and generic systems. Whereas $\langle \Delta \rangle = 1$ for nearly fully filled systems ($\rho \approx 0$), due to the global hinging mode that is present in symmetric but absent in generic systems, $\langle \Delta \rangle = 0$ for strongly diluted systems ($\rho \to 1$). The latter limit will be clarified in chapter 4, where we show this to be due to an absence of sufficiently large clusters of connected quads. Surprisingly, for intermediate cutting fractions, $\langle \Delta \rangle$ exhibits a peak and exceeds 1, showing that there exist dilution patterns for which $n_s - n_g \geq 2$.

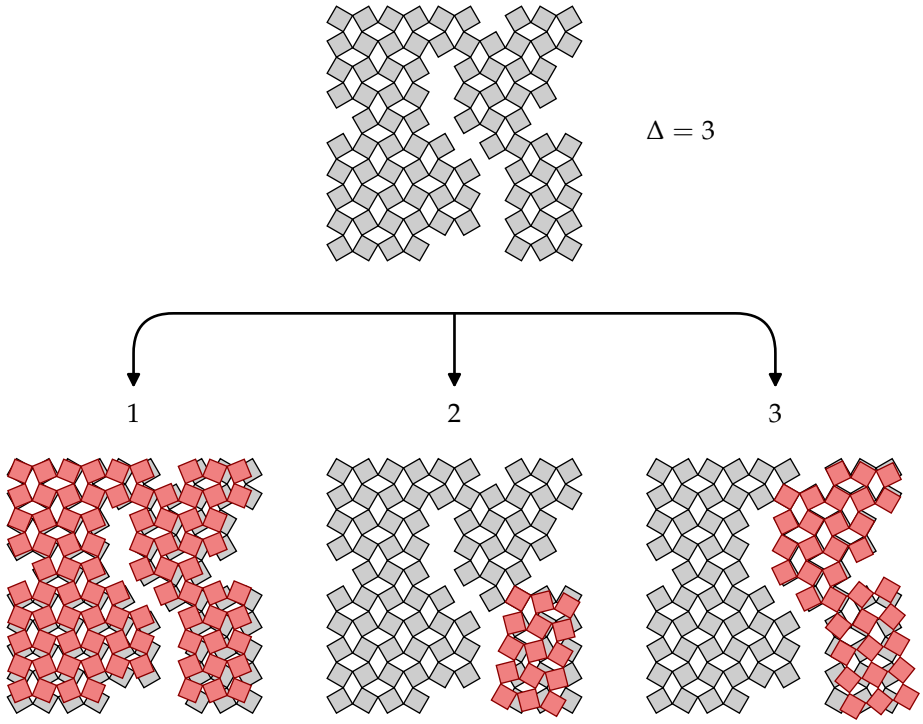

Figure 3.11: Spatial structure of excess zero modes. The randomly diluted 10×10 system ($\rho = 0.16$) shown at the top row has $n_s = 3$ and $n_g = 0$. The bottom row visualizes the spatial motions of the excess zero modes by superimposing the deformed geometry in red. To exclude additional displacements from global translations and/or rotations to these excess modes, the (x,y) position of the upper left square and the y position of the square directly next to it are held fixed (as might be noticed from mode 1).

We now illustrate the spatial structure of some excess zero modes. The particular cutting pattern shown in Fig. 3.11 features three excess zero modes, each of which has been visualized by extracting the associated displacement vector $(\Delta \mathbf{X})$ from the eigenmode analysis. Mode (1) can be recognized as the global hinging mode, whereas (2) and (3) are more complex and rely on the (oblique) sub-hinging of the individual clusters coloured in red. The observed sub-hinging of clusters plays, as we will show, a central role for excess zero modes.

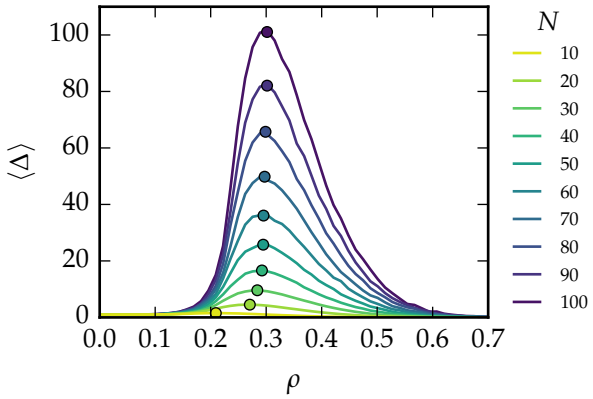

Figure 3.12: Statistics of the excess zero modes. For increasing system size N we have determined the multitude of excess zero modes as function of the cutting fraction. The maximum of each curve is marked by a filled circle.

3.3.2 The multitude of excess zero modes

We now reveal the multitude of excess zero modes $\langle\Delta\rangle$ as function of system size and cutting fraction. In Fig. 3.12 we show $\langle\Delta(\rho,N)\rangle$ for system sizes $N = 10,20,30,\ldots,90,100$, where we indicate the maximum of each curve by a filled circle. The number of runs needed to obtain reasonably well statistically converged curves decreases with N. To quantify the statistical convergence, we use the relative variance of Δ at the maximum as a criterium and demand $\sigma < 0.01\%$. The number of runs that follows from this criterium is subsequently also used for other values of ρ (at fixed N). In particular, using $\sigma^2 < 0.01\%$, we have found that an ensemble of typically 1100 simulations is required for $N = 20$, while an ensemble of only 100 simulations is sufficient for $N = 100$. The lower number of runs required for larger system sizes presumably is a result of spatial self-averaging, in which large systems can be regarded as a collection of smaller subsystems that are sufficiently uncorrelated.

Upon close inspection of the maxima in Fig. 3.12, we can make two observations. First, the location of the maximum, $\rho^{\max}$, increases with the system size and eventually converges to $\rho \approx 0.3$. Second, the value of the maximum, $\langle\Delta\rangle^{\max}$, grows with the system size, and becomes as large as $\langle\Delta\rangle^{\max} \approx 100$ for the largest system size considered. To characterize the

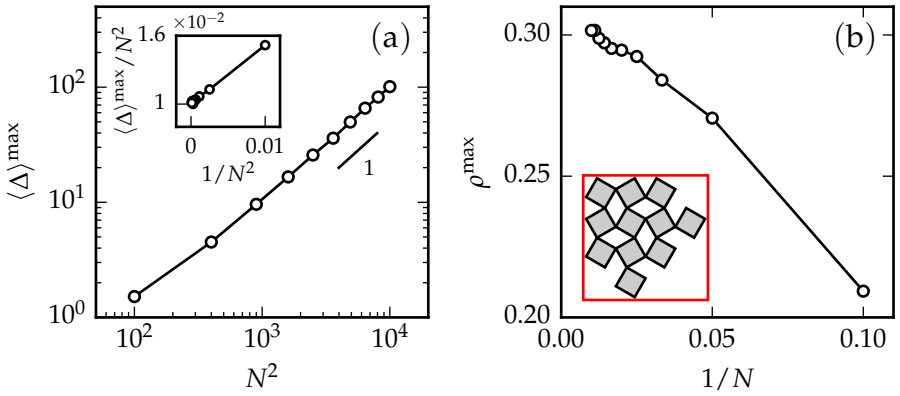

Figure 3.13: Peak behaviour of $\langle\Delta\rangle(\rho)$. For the data shown in Fig. 3.12, we have determined the value and location of the peak with system size. (a) The value of peak grows linearly with N^2 for large N (log scale, slope 1), implying that $\langle\Delta\rangle^{\max} \sim N^2$. Inset (linear scale): For small N, the scaling $\langle\Delta\rangle^{\max} \sim N^2$ exhibits finite size corrections proportional to $1/N^2$. (b) The peak location tends to a constant as $1/N$. Inset: Unit cell to understand the value of ρ_∞ (see main text).

behaviour of the maximum in detail, we measured $\rho^{\max}$ and $\langle\Delta\rangle^{\max}$ for each system size, where we refined our $\langle\Delta\rangle(\rho)$ data by a quadratic fit in the vicinity of the maximum. In Fig. 3.13 we show the obtained results for the value and position of the peak, from which we infer that

$$\langle\Delta\rangle^{\max} \approx \langle\Delta\rangle^{\star} := \beta\left(1 + \alpha/N^2\right)N^2, \tag{3.13a}$$

and

$$\rho^{\max} \approx \rho^{\star} := \rho_\infty - \gamma/N, \tag{3.13b}$$

where $\alpha \approx 51$, $\beta \approx 0.01$ and $\gamma \approx 0.99$ denote proportionality constants, and $\rho_\infty \approx 0.31 \pm 0.01$ the peak location in the $N \to \infty$ limit. We have determined the values of these constants by fitting Eqs. (3.13) to our data. The terms proportional to α and γ should be interpreted as finite size corrections to the large N asymptotics captured by $\langle\Delta\rangle^{\star} = \beta N^2$ and $\rho^{\star} = \rho_\infty$; the values of α and γ describe the convergence towards these large N asymptotics. Note that the asymptotic scaling $\langle\Delta\rangle^{\star} = \beta N^2$ implies that the mean number of excess zero modes in the peak regime is an intrinsic quantity, indicating roughly one extra excess zero mode for each 100

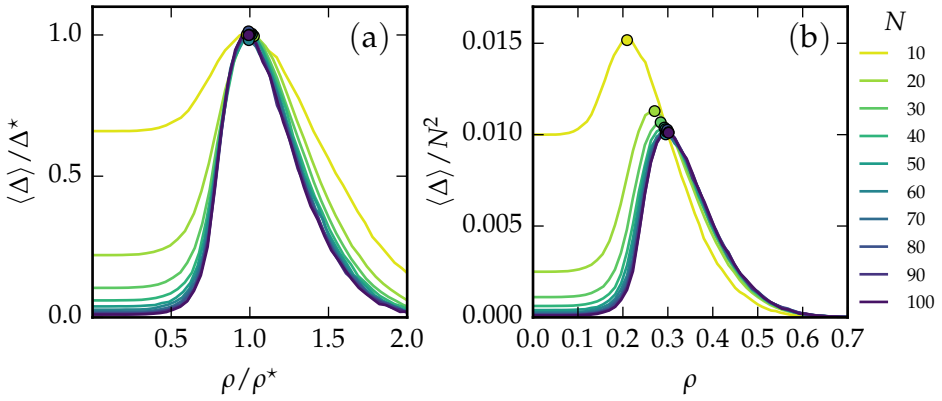

Figure 3.14: Scaling collapses for the $\langle\Delta\rangle(\rho)$ curves in Fig. 3.12. (a) Collapses obtained by rescaling the axes with $\rho^\star$ and $\Delta^\star$ (see main text), using $\alpha = 0.55$, $\beta = 0.01$, $\rho_\infty = 0.31$ and $\gamma = -0.97$. (b) The asymptotic evolution of the curves $\langle\Delta\rangle(\rho)/N^2$ for large N illustrate that, in leading order, $\langle\Delta\rangle$ scales as N^2 and ρ tends to a constant.

quads. The fact that there is a peak, its location, and the corresponding spatial structures can be understood by considering periodic samples with many small clusters. First, the smallest clusters that yield excess zero modes are of size 3×3. We now assume that the maximum number of excess zero modes is obtained by filling the system of given size N with a large number of 3×3 clusters, connected in such a way that all (symmetric) clusters retain their internal hinging mode. The simplest and most intuitive topology that satisfies these conditions consists of 3×3 clusters separated by one column and row each, with a few quads placed on the otherwise empty rows and columns to (weakly) connect adjacent clusters. To make sure the generic system remains rigid, with the symmetric system having many hinging modes, we suggest to connect each cluster pair by two quads. The resulting unit cell of this dilution geometry [see inset of Fig. 3.13(b)] has a cutting fraction $\rho = 5/16 \approx 0.31$. This value shows a surprisingly good agreement with the peak location for random dilution in the $N \to \infty$ limit.

Finally, the relations for peak value and location in Eqs. (3.13) suggest that the mean number of excess zero modes exhibits finite size scaling, as $\langle\Delta\rangle/\langle\Delta\rangle^\star = f(\rho/\rho^\star)$. To demonstrate this, we rescale our $\langle\Delta\rangle(\rho,N)$ data

according to Eqs. (3.13), and plot the result in Fig. 3.14(a). We observe that the peak positions and values collapse, as expected, but we moreover observe that the tails of $\langle\Delta\rangle/\langle\Delta\rangle^\star$ also display a scaling collapse as $N \to \infty$, demonstrating that the mean number of excess zero modes exhibits finite sizing scaling. For completeness, Fig. 3.14(b) shows the leading order scaling collapse, $\langle\Delta\rangle/N^2$, confirming that $\langle\Delta\rangle$ scales as N^2 and ρ goes to a constant for large N.

3.3.3 Distribution of excess zero modes in the peak regime

Having presented the ensemble averages $\langle\Delta\rangle(\rho, N)$, we now focus on the ensemble distribution of excess zero modes in the peak regime of $\langle\Delta\rangle(\rho, N)$. To visualize these distributions with system size, we have determined the cumulative distribution functions (CDFs) for the ensembles of cutting sequences that correspond to $\rho = \rho^\star$ (Fig. 3.15).

The CDFs in Fig. 3.15(a) display the probability P to encounter a given Δ which is less than or equal to k times the mean $\langle\Delta\rangle^\star$. This reveals that the excess modes in the peak regime are symmetrically distributed around their mean for system sizes $\sqrt{N} \gtrsim 30$. In contrast, these appear asymmetrically distributed for smaller N due to the low number of possible excess zero modes in small systems. We furthermore observe that deviations from the mean decrease with system size; the probability to randomly encounter cutting patterns that strongly deviate from the mean is much higher in small systems as compared to large systems, due to the rapid increase of the number of possible cutting patterns with N. In Fig. 3.15(b) we have re-plotted the data in panel (a) as function of $(k-1)N$ and observe a scaling collapse for large N. According to the central limit theorem [124], the collapse demonstrates that the distribution of excess zero modes in the peak regime appears Gaussian, with standard deviation $\sigma \sim 1/N$. Note that this standard deviation implies that the number of independent measures on Δ scales with N^2, confirming our earlier hypothesis that large systems are self-averaging and may be regarded as to consist of sufficiently uncorrelated subsystems.

The findings presented here naturally raise the question how to obtain extreme designs that have significantly more excess zero modes than typical, and in section 3.4 we will develop a procedure that allows us to design geometries featuring $\Delta/\langle\Delta\rangle^\star \approx 6$, even for system sizes as large as $N = 100$.

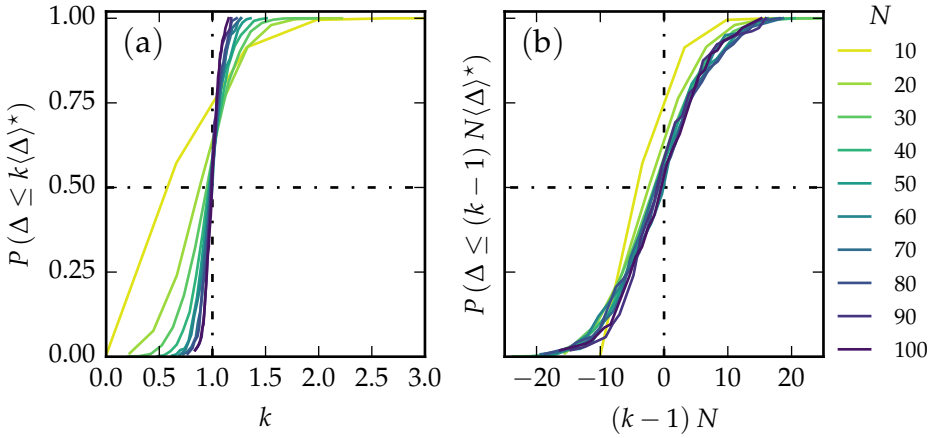

Figure 3.15: CDFs for $\Delta(\rho, N)$ in the peak regime ($\rho = \rho^{\max}$), for the data shown in Fig. 3.12. (a) The excess zero modes are symmetrically distributed around the mean $\langle\Delta\rangle^\star$ ($k = 1$) for sufficiently large system sizes. (b) Re-plotting the data shown in panel (a) as function of $(k-1)N$ results in a collapse of the curves.

3.4 Extreme systems

In this section we design systems with a large number of excess zero modes, where Δ is significantly larger than the average maximum for random cutting, $\langle\Delta\rangle^\star$. To design such systems one could follow two distinct routes. The first one consists of the brute force calculation of all possible configurations given a system size. This method is not feasible, however, as the design space is enormous: The maximum number of configurations grows exponentially with the system size and already becomes $2^{N^2} = 2^{100}$ for 10×10 systems. This number can be reduced to $\binom{100}{21} \approx 10^{21}$ by taking into account configurations at the maximum cutting fraction $\rho^\star = 0.21$ only, but the number remains enormous. Based on benchmarks of our Python based code (~ 200 iterations/s for a 10×10 system) it would take up to 10^{11} years to examine all configurations. Alternatively (the second route), one can determine the maximum Δ for a smaller, feasible system size and utilize it as an unit cell to tile the larger system — which is the approach we will use in this section.

To minimize finite size effects on the tiled system we apply periodic boundary conditions on the unit cell and consider a unit cell whose size

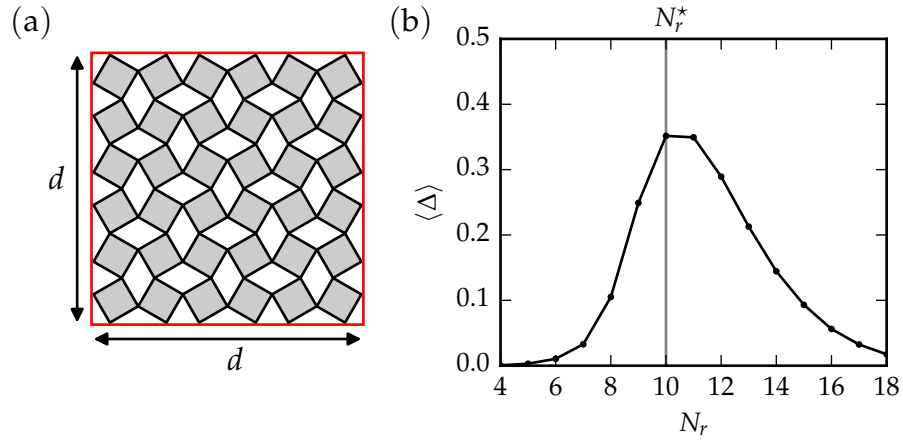

Figure 3.16: Random dilution of a 6×6 unit cell with periodic boundaries. (a) Fully filled unit cell where a fixed box size d ensures periodicity. (b) Average number of excess zero modes as function of the number of randomly removed quads for 10^6 realizations. The curve displays a maximum at $N_r = N_r^\star = 10$ as indicated by the grey line.

is as large as possible, while being computationally feasible. Based on these criteria we use a unit cell of size 6×6 $(N_u = 6)$ confined within a box of size d, as depicted in Fig. 3.16(a). Here the box size d naturally arises for periodic boundary conditions as connecting the left/right and lower/upper boundaries of the unit cell leads to a fixed opening angle ϕ_0 with corresponding box size $d = N_u\,[\cos(\phi_0) + \sin(\phi_0)]$. An important consequence of periodic boundary conditions with fixed d is that symmetric systems lose their global hinging mode, in contrast to systems with open boundaries which always have $n_s = 1$ for full filling. In order to hinge, symmetric systems need to be able to contract/expand [see Fig. 3.7(a)], which is not possible at fixed d. Indeed, Fig. 3.16(b) demonstrates that the number of excess zero modes starts growing from $\langle \Delta \rangle = 0$, rather than $\langle \Delta \rangle = 1$, as in Fig. 3.10(c). Furthermore, Fig. 3.16(b) shows that $\langle \Delta \rangle$ is maximum when the number of removed quads is $N_r = 10$. Denoting this maximum by $N_r^\star$, our goal is to determine Δ for all possible unit cell geometries at $N_r = N_r^\star$.

The number of possible unit cell geometries at $N_r = N_r^\star$ can be reduced by the consistent removal of the upper left quad (or any other quad) in

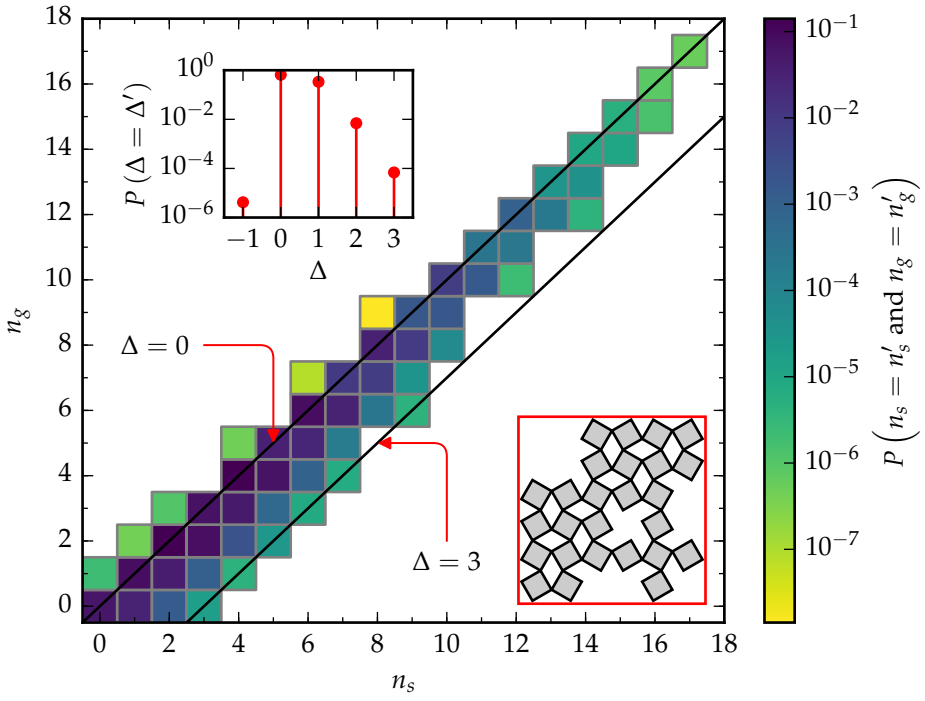

Figure 3.17: Discrete joint probability distribution as a function of n_s and n_g. The data comprises all possible geometries in a 6×6 periodic unit cell when 10 quads are removed. The black lines have constant Δ and its value is indicated by the arrows. Inset graph: Discrete probability distribution of Δ for the same data. Inset dilution geometry: An unit cell featuring $\Delta = 3$, for periodic boundaries.

each geometry we consider. Without loss of generality, this breaks the symmetry that comes with periodic boundaries. This leaves us with a total of

$$\binom{N_u^2 - 1}{N_r^\star - 1} = \binom{35}{9} \approx 7.1 \times 10^7 \tag{3.14}$$

geometries to consider, which takes approximately 4 days for our Python based code. For each geometry we have tracked n_s and n_g and their outcome is graphically displayed by a joint probability distribution in Fig. 3.17. For discrete variables this is also known as a joint probability mass function. In Fig. 3.17 black lines of slope unity represent contours

of constant Δ, with the main diagonal equivalent to $\Delta = 0$. We thus find that a periodic 6×6 system comprises maximally 3 excess zero modes, whereas the probability mass function of Δ (inset graph of Fig. 3.17) exposes that the appearance of $\Delta = 3$ constitutes a fraction $\sim 10^{-4}$ of the design space—tantamount to $\sim 7.1 \times 10^3$ unique cutting geometries, of which the particular unit cell depicted at the right bottom of Fig. 3.17 will be used to tile larger systems in section 3.4.1. The remaining part of the design space is mostly occupied by $\Delta = 0$, since bins of high probability are mainly located along the major diagonal of the joint probability distribution.

Surprisingly, however, Fig. 3.17 reveals that Δ can also become smaller than zero, although its appearance is rare, $P(\Delta = -1) \approx 10^{-6}$. In these cases generic systems, rather than symmetric systems, attain an extra near-zero mode that arises due to a special, coincidental combination of random quad distortions — we have verified these modes disappear when a different random quad distortion is imposed to the same cutting geometry. In particular, we found that near-zero modes typically exhibit $\lambda \approx 10^{-12}$, which is a few orders of magnitude larger than true numerical zero modes (Fig 3.9). Here we note that near-zero modes span a small part of the design space; their detailed consideration lies outside the scope of this thesis.

3.4.1 Tiling the unit cell

We now periodically tile the $N_u \times N_u$ unit cell to built larger $nN_u \times nN_u$ systems $(n = 2,3,\dots)$ [see Fig. 3.18(a) for $n = 2$], and determine their number of excess zero modes accordingly. Importantly, note that we use open boundary conditions for the tiled systems.

In Fig. 3.18(b) we display the number of excess zero modes of the tiled systems with n, which shows that the tiled systems (open circles, solid line) exhibit a significantly larger number of excess zero modes as compared to randomly diluted, non-tiled systems of identical size (dashed blue). Here, the dashed blue line describes the asymptotic growth of the average number of zero modes according to βN^2, with associated density $\beta = 0.01$ (see section 3.3.2). As can furthermore be observed, Δ of the tiled systems grows proportionally to $(nN_u)^2$, implying these systems are characterized by a constant density of zero modes. In particular, we have determined $\Delta/(nN_u)^2 \approx 0.06$ — which exceeds the density of zero

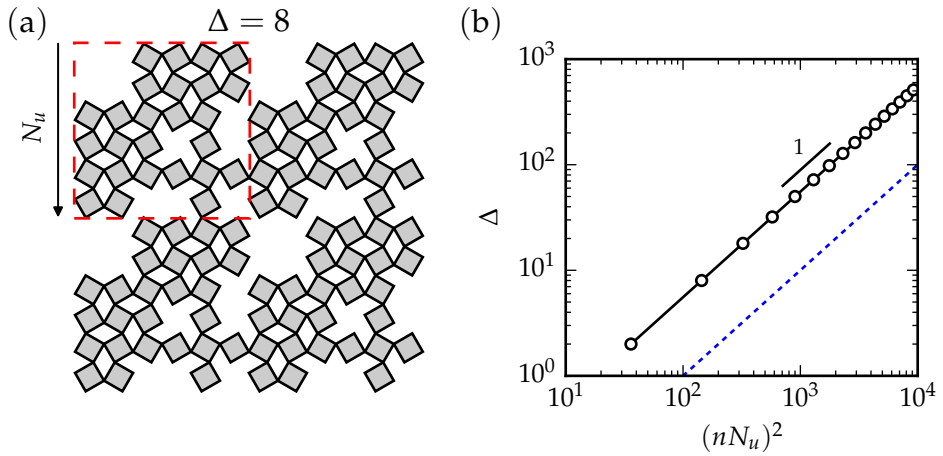

Figure 3.18: Excess modes in $nN_u \times nN_u$ systems built by the periodic tiling of a $N_u \times N_u$ unit cell ($n = 1,2,3,\dots$). (a) System corresponding to $n = 2$, resulting in $\Delta = 8$. The quads enclosed within the dashed red region display the unit cell. (b) The number of excess zero modes grows proportionally with $(nN_u)^2$ (open circles, solid line). We display data up to $n = 16$ ($nN_u = 96$). The blue dashed line represents the asymptotic growth of excess zero modes in randomly diluted systems as function of system size.

modes for random cutting by a factor 6. Hence, this procedure allows us to construct geometries for which Δ is 6 times larger as compared to the average maximum for random cutting ($\Delta/\Delta^\star \approx 6$), at a given system size.

3.5 Random bond removal

In this section we characterize the number of excess zero modes, Δ_b, for random bond removal, as function of the fraction of removed bonds, ρ_b, and system size N, and discuss differences and similarities with random quad removal.

In Fig. 3.19(a) we display $\langle \Delta_b \rangle (\rho_b, N)$ for system sizes $N = 10,20,\dots 80$, which are obtained using a similar procedure as devised for quad removal in section 3.3, now removing bonds rather than quads. Interestingly, these curves are qualitatively similar to results for quad removal (Fig. 3.12) and demonstrate that the number of excess zero modes may equally exceed one in systems where bonds are cut: Analogously to

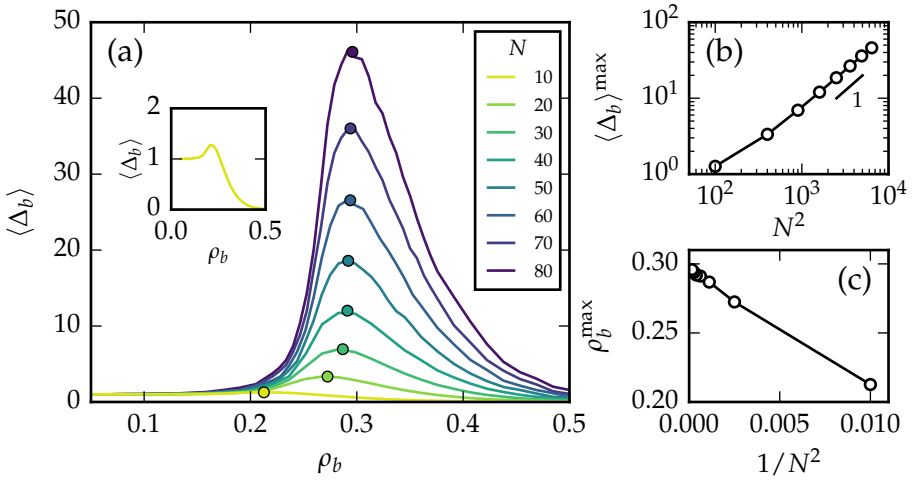

Figure 3.19: Statistics of the excess zero modes for random bond removal. (a) The average number of excess zero modes as function of the cutting fraction for a range of system sizes, using the same ensemble size as for random quad removal. Filled circles mark the maximum of each curve. Inset figure: Zoom in of $\langle\Delta_b\rangle(\rho_b)$ for $N = 10$. (b) The peak value grows linearly with N^2 for large N (log scale, slope 1), implying that $\langle\Delta_b\rangle^{\max} \sim N^2$. For small N, the scaling $\langle\Delta_b\rangle^{\max} \sim N^2$ exhibits finite size corrections proportional to $1/N^2$ (not shown). (c) The peak location tends to a constant as $1/N^2$.

quad removal, $\langle\Delta_b\rangle = 1$ for $\rho \approx 0$ and $\langle\Delta_b\rangle = 0$ for $\rho_b \to 0$ [see inset of Fig. 3.19(a)], whereas $\langle\Delta_b\rangle > 1$ for intermediate cutting fractions, albeit with an amplitude which is roughly 1.5 times smaller than for quad removal at given N. In the low cutting fraction limit ($\rho \approx 0$) systems are over-constrained and retain their rigidity in the generic case, even when some bonds are missing, leading to $\langle\Delta_b\rangle = 1$. In contrast, systems in the high cutting fraction limit ($\rho_b \to 1$) consist of many loosely connected quads that fail to constitute a rigid system in the generic case, hence $\langle\Delta_b\rangle = 0$.

To quantify differences and similarities between quad and bond removal, we follow section 3.3.2 and determine the peak value and location of $\langle\Delta_b\rangle$, which we denote $\rho_b^{\max}$ and $\langle\Delta_b\rangle^{\max}$, as function of the system size. The obtained results are shown in Fig. 3.19(b-c), and suggest the

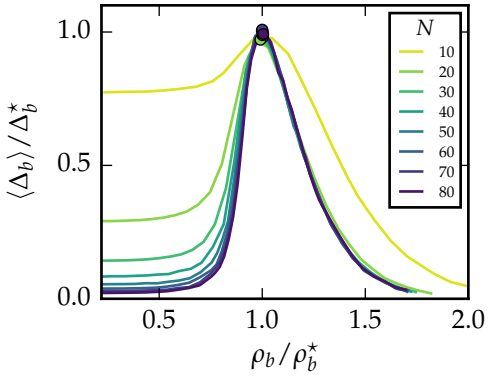

Figure 3.20: Scaling collapse for the $\langle\Delta_b\rangle$ curves in Fig. 3.19(a), obtained by rescaling the axes according to the relations given in Eqs. (3.15).

following asymptotic scaling relations:

$$\langle\Delta_b\rangle^{\max} \approx \langle\Delta_b\rangle^\star := \beta_b \left(1 + \frac{\alpha_b}{N^2}\right) N^2, \tag{3.15a}$$

and

$$\rho_b^{\max} \approx \rho_b^\star := \rho_{\infty,b} - \gamma_b / N^2, \tag{3.15b}$$

where $\alpha_b \approx 75$, $\beta_b \approx 0.007$, $\gamma_b \approx 8.37$ and $\rho_{\infty,b} \approx 0.3 \pm 0.01$ are constants with an interpretation similar to their analogues for quad removal in section 3.3. The asymptotic scaling relations and the values of their associated constants as obtained here reveal some contrasts between quad and bond removal.

First, similar to quad removal [Eq. (3.13a)], the peak value for bond removal grows proportionally to N^2, such that β_b can again be interpreted as the intrinsic spatial density of excess zero modes. Interestingly, we find that the intrinsic spatial density of zero modes for quad removal exceeds that of random bond removal by a factor $\beta/\beta_b \approx 1.5$, in agreement with the observation $\langle\Delta\rangle^{\max} > \langle\Delta_b\rangle^{\max}$. Apparently, the more correlated removal of bonds that occurs in quad removal (4 per removed quad) promotes the development of excess zero modes.

Second, the peak locations for bond and quad removal converge differently as function of N, but their peak locations in the $N \to \infty$ are the same within error bars: Whereas the peak location for quad removal

tends to the constant $\rho_\infty \approx 0.31 \pm 0.01$, the peak location for bond removal tends to the constant $\rho_{\infty,b} \approx 0.30 \pm 0.01$. We note that rescaling $\langle \Delta_b \rangle (\rho_b, N)$ according to Eqs. (3.15) yields a scaling collapse for large N (Fig. 3.20), demonstrating that $\langle \Delta_b \rangle$, similar to random quad removal, exhibits finite size scaling with simple mean field exponents.

In short, we have demonstrated that random bond removal qualitatively displays the same features as random quad removal. In both cases, the large N asymptotics prescribe that the peak tends to a constant location and that the number of excess zero modes grows proportionally to N^2. Quantitatively, we have found that the asymptotic peak peak location for quad and bond removal agrees within error bars, although the peak locations converge with different exponents. Furthermore, we have shown that the absolute number of excess zero modes is roughly 1.5 times larger for quad removal than for bond removal.

3.6 Conclusions

In this chapter we compared the number of zero modes in generic and symmetric collections of flexibly linked, rigid quads. We showed that symmetric systems featuring identical squares can possess excess zero modes that do not exist in generic systems consisting of irregular quads.

We have determined the average number of excess zero modes, $\langle \Delta \rangle$, for a large ensemble of independent, diluted systems, in which a fraction ρ of the total number of quads has been randomly removed. By using the same dilution pattern for symmetric and generic systems, we determined the ensemble averages $\langle \Delta \rangle (\rho, N)$ and revealed subtle but important differences between symmetric and generic systems. We found that $\langle \Delta \rangle \to 1$ for small cutting fractions ($\rho \to 0$), and $\langle \Delta \rangle \to 0$ for large cutting fractions ($\rho \to 1$). Interestingly, the number of excess zero modes at intermediate cutting fractions was shown to exhibit a maximum for which $\langle \Delta \rangle > 1$.

Subsequently, we determined $\langle \Delta \rangle (\rho, N)$ for a range of system sizes and showed that the peak value and location of $\langle \Delta \rangle$ exhibits simple scaling relations with N. By rescaling $\langle \Delta \rangle (\rho, N)$ using the relations for the peak value and location we obtained a scaling collapse, demonstrating that the average number of excess zero modes is an intrinsic quantity which exhibits finite size scaling with mean field exponents. By periodically tiling a 6×6 unit cell — with the maximum number of 3 excess

modes for periodic boundaries — we have also been able to design dilution geometries with a density of zero modes that is six times higher than the average for random cutting, independently of system size. Finally, for random bond removal, we have a found a very similar scaling collapse and peak location, with a density of zero modes that is roughly 1.5 times smaller than for random quad removal.

Appendix

3.A Constructing the gradient

The goal of this appendix is to analytically construct the energy gradient $\nabla E(\mathbf{X}) = \partial E/\partial \mathbf{X}$, which we will do by expressing the components of the gradient exclusively as functions of the corner coordinates of the quads. This procedure circumvents the need to determine derivatives using finite differences and leads to a significantly faster and more precise calculation of the gradient.

To calculate the gradient we use the energy as given in Eq. (3.6), which yields that

$$\frac{\partial E}{\partial \mathbf{X}} = \frac{1}{2}\frac{\partial}{\partial \mathbf{X}}\left(\sum_{s=0}^{N_b} \ell_s(\mathbf{X})^2\right). \tag{3.16}$$

Here $\ell_s(\mathbf{X})$ is some complicated function that describes the spring lengths as function of $\mathbf{X}$. Since springs are connected the corners of quads, we can express their square length as

$$\ell_s^2(\mathbf{X}) = \left[x_{n,i}(\mathbf{X}) - x_{m,j}(\mathbf{X})\right]^2 + \left[y_{n,i}(\mathbf{X}) - y_{m,j}(\mathbf{X})\right]^2, \tag{3.17}$$

where $(x_{n,i}, y_{n,i})$ and $(x_{m,j}, y_{m,j})$ describe the positions of the corners $(i = 0,1,2,3)$ of quad n and the corners $(j = 0,1,2,3)$ of quad m respectively. Following section 3.2, these corners can be calculated according to

$$\begin{pmatrix} x_{n,i} \\ y_{n,i} \end{pmatrix} = \begin{pmatrix} x_n \\ y_n \end{pmatrix} + \|\mathbf{e_{n,i}}\| \begin{pmatrix} \cos(\theta_{n,i} + \varphi_n) \\ \sin(\theta_{n,i} + \varphi_n) \end{pmatrix}, \tag{3.18}$$

with $\theta_{n,i} = \arg(\mathbf{e_{n,i}})$ the centre-to-corners angles of the quad, and where Eq. (3.18) similarly applies to quad m. Using the above relations, we now express the gradient components $\partial E/\partial x_n$, $\partial E/\partial y_n$ and $\partial E/\partial \varphi_n$ in terms of the corner coordinates $x_{n,i}$ and $y_{n,i}$. Note that we do not evaluate the obtained derivatives as function of the corner coordinates; although these can analytically calculated using Eq. (3.17), this would require specific knowledge about the dilution pattern as entitled in the adjacency matrix.

Derivatives with respect to x_n

Any change in the quad's coordinate x_n involves the x-displacement of the four corners. Therefore, the associated energy change is

$$\begin{aligned}\frac{\partial E}{\partial x_n} &= \frac{\partial E}{\partial x_{n,1}}\frac{\partial x_{n,1}}{\partial x_n} + \frac{\partial E}{\partial x_{n,2}}\frac{\partial x_{n,2}}{\partial x_n} + \frac{\partial E}{\partial x_{n,3}}\frac{\partial x_{n,3}}{\partial x_n} + \frac{\partial E}{\partial x_{n,4}}\frac{\partial x_{n,4}}{\partial x_n} \\ &= \sum_{i=1}^{4} \frac{\partial E}{\partial x_{n,i}}\frac{\partial x_{n,i}}{\partial x_n} \\ &= \sum_{i=1}^{4} \frac{\partial E}{\partial x_{n,i}},\end{aligned} \tag{3.19}$$

where we have used that $\partial x_{n,i}/\partial x_n = 1$, by Eq. (3.18).

Derivatives with respect to y_n

Similarly, the derivative of the energy with respect to y_n can be written as

$$\begin{aligned}\frac{\partial E}{\partial y_n} &= \sum_{i=1}^{4} \frac{\partial E}{\partial y_{n,i}}\frac{\partial y_{n,i}}{\partial y_n} \\ &= \sum_{i=1}^{4} \frac{\partial E}{\partial y_{n,i}}.\end{aligned} \tag{3.20}$$

Derivatives with respect to φ_n

Last, any change in the rotational angle φ_n introduces changes in both the x and y corner coordinates of quad n, yielding the following derivative for φ_n

$$\begin{aligned}\frac{\partial E}{\partial \varphi_n} &= \sum_{i=1}^{4} \left[\frac{\partial E}{\partial x_{n,i}}\frac{\partial x_{n,i}}{\partial \varphi_n} + \frac{\partial E}{\partial y_{n,i}}\frac{\partial y_{n,i}}{\partial \varphi_n} \right] \\ &= \sum_{i=1}^{4} \left[\|\mathbf{e_{n,i}}\| \left(\cos(\theta_i + \varphi_n) \frac{\partial E}{\partial y_{n,i}} - \sin(\theta_i + \varphi_n) \frac{\partial E}{\partial x_{n,i}} \right) \right],\end{aligned} \tag{3.21}$$

where we have substituted $\partial x_{n,i}/\partial \varphi_n = -\|\mathbf{e_{n,i}}\| \sin(\theta_i + \varphi_n)$ and $\partial y_{n,i}/\partial \varphi_n = \|\mathbf{e_{n,i}}\| \cos(\theta_i + \varphi_n)$, as obtained from Eq. (3.18).

3.B Constructing the Hessian matrix

Following the approach of appendix 3.A we now analytically determine the Hessian by expressing all second order derivatives of the energy in terms of the quads' corner coordinates. We therefore consider all possible second order partial derivatives of the energy with respect to the degrees of freedom of quad m and n, respectively given by (x_n, y_n, φ_n) and (x_m, y_m, φ_m). Below we determine the derivatives for the cases $m = n$ and $m \neq n$, which comprise a total of 12 independent types of partial derivatives.

Second derivatives with respect to x_m and x_n

$$\begin{aligned} \frac{\partial}{\partial x_m}\left(\frac{\partial E}{\partial x_n}\right) &= \frac{\partial}{\partial x_m}\sum_{i=1}^{4}\frac{\partial E}{\partial x_{n,i}} \\ &= \sum_{i=1}^{4}\frac{\partial}{\partial x_{n,i}}\frac{\partial E}{\partial x_m} \\ &= \sum_{i=1}^{4}\left[\frac{\partial}{\partial x_{n,i}}\sum_{j=1}^{4}\frac{\partial E}{\partial x_{m,j}}\right] \end{aligned} \tag{3.22}$$

For $m = n$, this yields:

$$\frac{\partial^2 E}{\partial x_n^2} = \sum_{i=1}^{4}\frac{\partial^2 E}{\partial x_{n,i}^2}, \tag{3.23}$$

For $m \neq n$ and under the assumption that corner i of quad n is connected to corner j of quad m, we obtain:

$$\frac{\partial^2 E}{\partial x_n \partial x_m} = \frac{\partial^2 E}{\partial x_{n,i}\partial x_{m,j}}, \tag{3.24}$$

Second derivatives with respect to y_m and y_n.

Following the approach to calculate the second derivatives with respect to x, we obtain

$$\frac{\partial^2 E}{\partial y_n^2} = \sum_{i=1}^{4}\frac{\partial^2 E}{\partial y_{n,i}^2}, \tag{3.25}$$

Under the assumption that corner i of quad n is connected to corner j of quad m, we obtain:

$$\frac{\partial^2 E}{\partial y_n \partial y_m} = \frac{\partial^2 E}{\partial y_{n,i} \partial y_{m,j}}. \tag{3.26}$$

Second derivatives with respect to φ_m and φ_n.

$$\frac{\partial}{\partial \varphi_m}\left(\frac{\partial E}{\partial \varphi_n}\right) = \frac{\partial}{\partial \varphi_m}\sum_{i=1}^{4}\left[\frac{\partial E}{\partial x_{n,i}}\frac{\partial x_{n,i}}{\partial \varphi_n} + \frac{\partial E}{\partial y_{n,i}}\frac{\partial y_{i,n}}{\partial \varphi_n}\right] \tag{3.27}$$

On the right hand side of the above equation, the first term within the summation represents the x contribution and the second term the y contribution for the derivative of E with respect to φ_n. For clarity we will first calculate the above derivative leaving out the second term, because the results for the first and second term will take an identical functional form. Therefore, we start with:

$$\begin{aligned}
&\frac{\partial}{\partial \varphi_m}\sum_{i=1}^{4}\frac{\partial E}{\partial x_{n,i}}\frac{\partial x_{n,i}}{\partial \varphi_n} \\
&= \sum_{i=1}^{4}\left[\frac{\partial^2 E}{\partial \varphi_m \partial x_{n,i}}\frac{\partial x_{n,i}}{\partial \varphi_n} + \frac{\partial E}{\partial x_{n,i}}\frac{\partial^2 x_{n,i}}{\partial \varphi_m \partial \varphi_n}\right] \\
&= \sum_{i=1}^{4}\left[\frac{\partial}{\partial x_{n,i}}\left(\sum_{j=1}^{4}\left[\frac{\partial E}{\partial x_{m,j}}\frac{\partial x_{m,j}}{\partial \varphi_m} + \frac{\partial E}{\partial y_{m,j}}\frac{\partial y_{m,j}}{\partial \varphi_m}\right]\right)\frac{\partial x_{n,i}}{\partial \varphi_n} + \frac{\partial E}{\partial x_{n,i}}\frac{\partial^2 x_{n,i}}{\partial \varphi_m \partial \varphi_n}\right] \\
&= \sum_{i=1}^{4}\left[\sum_{j=1}^{4}\left[\frac{\partial^2 E}{\partial x_{n,i}\partial x_{m,j}}\frac{\partial x_{m,j}}{\partial \varphi_m}\right]\frac{\partial x_{n,i}}{\partial \varphi_n} + \frac{\partial E}{\partial x_{n,i}}\frac{\partial^2 x_{n,i}}{\partial \varphi_m \partial \varphi_n}\right].
\end{aligned} \tag{3.28}$$

For $m = n$, this yields

$$\frac{\partial}{\partial \varphi_m}\sum_{i=1}^{4}\frac{\partial E}{\partial x_{n,i}}\frac{\partial x_{n,i}}{\partial \varphi_n} = \sum_{i=1}^{4}\left[\frac{\partial^2 E}{\partial x_{n,i}^2}\frac{\partial^2 x_{n,i}}{\partial \varphi_n^2} + \frac{\partial E}{\partial x_{n,i}}\frac{\partial^2 x_{n,i}}{\partial \varphi_n^2}\right]. \tag{3.29}$$

For $m \neq n$, and assuming that corner i of quad n is connected to corner j of quad m, we obtain from Eq. (3.28):

$$\frac{\partial}{\partial \varphi_m}\sum_{i=1}^{4}\frac{\partial E}{\partial x_{n,i}}\frac{\partial x_{n,i}}{\partial \varphi_n} = \frac{\partial^2 E}{\partial x_{n,i}\partial x_{m,j}}\frac{\partial x_{m,j}}{\partial \varphi_m}\frac{\partial x_{n,i}}{\partial \varphi_n}. \tag{3.30}$$

We have now calculated the outcome of Eq. (3.27) taking into account the x-contribution only. Because the y-contribution takes the same form as Eqs. (3.29-3.30), we obtain $(m = n)$:

$$\frac{\partial^2 E}{\partial \varphi_n^2} = \sum_{i=1}^{4} \left[\frac{\partial^2 E}{\partial x_{n,i}^2} \frac{\partial^2 x_{n,i}}{\partial \varphi_n^2} + \frac{\partial E}{\partial x_{n,i}} \frac{\partial^2 x_{n,i}}{\partial \varphi_n^2} + \frac{\partial^2 E}{\partial y_{n,i}^2} \frac{\partial^2 y_{n,i}}{\partial \varphi_n^2} + \frac{\partial E}{\partial y_{n,i}} \frac{\partial^2 y_{n,i}}{\partial \varphi_n^2} \right] \tag{3.31}$$

where $\partial^2 x_{n,i}/\partial \varphi_n^2 = -\|\mathbf{e_{n,i}}\| \cos(\theta_i + \varphi_n)$ and $\partial^2 y_{n,i}/\partial \varphi_n^2 = -\|\mathbf{e_{n,i}}\| \sin(\theta_i + \varphi_n)$, by Eq. (3.18). For $m \neq n$ we obtain:

$$\frac{\partial^2 E}{\partial \varphi_m \partial \varphi_n} = \frac{\partial^2 E}{\partial x_{n,i} \partial x_{m,j}} \frac{\partial x_{m,j}}{\partial \varphi_m} \frac{\partial x_{n,i}}{\partial \varphi_n} + \frac{\partial^2 E}{\partial y_{n,i} \partial y_{m,j}} \frac{\partial y_{m,j}}{\partial \varphi_m} \frac{\partial y_{n,i}}{\partial \varphi_n}. \tag{3.32}$$

Cross derivatives with respect to x_m, x_n, y_m and y_n.

$$\begin{aligned} \frac{\partial}{\partial y_m} \left(\frac{\partial E}{\partial x_n} \right) &= \frac{\partial}{\partial y_m} \sum_{i=1}^{4} \frac{\partial E}{\partial x_{n,i}} \\ &= 0, \end{aligned} \tag{3.33}$$

for both $m = n$ and $m \neq n$, because $\partial E/\partial x_{n,i}$ does not depend on y_m. Hence,

$$\frac{\partial^2 E}{\partial x_n^2} = 0, \tag{3.34}$$

and

$$\frac{\partial^2 E}{\partial x_m \partial x_n} = 0. \tag{3.35}$$

Cross derivatives with respect to x_m, x_n, φ_m and φ_n.

$$\begin{aligned}\frac{\partial}{\partial x_m}\left(\frac{\partial E}{\partial \varphi_n}\right) &= \frac{\partial}{\partial x_m}\sum_{i=1}^{4}\left[\frac{\partial E}{\partial x_{n,i}}\frac{\partial x_{n,i}}{\partial \varphi_n}+\frac{\partial E}{\partial y_{n,i}}\frac{\partial y_{i,n}}{\partial \varphi_n}\right]\\ &= \sum_{i=1}^{4}\left[\frac{\partial^2 E}{\partial x_m \partial x_{n,i}}\frac{\partial x_{n,i}}{\partial \varphi_n}+\frac{\partial E}{\partial x_{n,i}}\frac{\partial x_{n,i}^2}{\partial x_m \varphi_n}\right]\\ &= \sum_{i=1}^{4}\left[\frac{\partial}{\partial x_{n,i}}\left(\sum_{j=1}^{4}\frac{\partial E}{\partial x_{m,j}}\right)\frac{\partial x_{n,i}}{\partial \varphi_n}\right]\\ &= \sum_{i=1}^{4}\left[\sum_{j=1}^{4}\left[\frac{\partial^2 E}{\partial x_{n,i}\partial x_{m,j}}\right]\frac{\partial x_{n,i}}{\partial \varphi_n}\right].\end{aligned} \tag{3.36}$$

For $m = n$, this yields

$$\frac{\partial^2 E}{\partial x_n \partial \varphi_n} = \sum_{i=1}^{4}\frac{\partial^2 E}{\partial x_{n,i}^2}\frac{\partial x_{n,i}}{\partial \varphi_n}. \tag{3.37}$$

And for $m \neq n$, assuming that corner i of quad m is connected to corner j of quad n, we obtain

$$\frac{\partial^2 E}{\partial x_m \partial \varphi_n} = \frac{\partial^2 E}{\partial x_{n,i}\partial x_{m,j}}\frac{\partial x_{n,i}}{\partial \varphi_n}. \tag{3.38}$$

Cross derivatives with respect to y_m, y_n, φ_m and φ_n.

The derivation is identical to the cross derivatives with respect to x and φ. For $m = n$, the result therefore is

$$\frac{\partial^2 E}{\partial y_n \partial \varphi_n} = \sum_{i=1}^{4}\frac{\partial^2 E}{\partial y_{n,i}^2}\frac{\partial y_{n,i}}{\partial \varphi_n}. \tag{3.39}$$

And for $m \neq n$, assuming that corner i of quad m is connected to corner j of quad n, we obtain

$$\frac{\partial^2 E}{\partial y_m \partial \varphi_n} = \frac{\partial^2 E}{\partial y_{n,i}\partial y_{m,j}}\frac{\partial y_{n,i}}{\partial \varphi_n}. \tag{3.40}$$

4

Topology based counting of excess zero modes

For disordered systems in 2D, the number of zero modes can be determined exactly from the connection topology [47, 48], but for symmetric systems we are not aware of general techniques to do so. Here we develop an approximate counting method for the number of zero modes in diluted symmetric systems consisting of hinging squares. We describe these systems as a collection of clusters coupled by connectors and use their topology to iteratively estimate the number of zero modes. We compare the iterative results of our topology based counting method to exact calculations based on the Hessian matrix, and show that we obtain a tight lower bound on the number of excess zero modes.

A paper based on the work presented in this chapter is in preparation for submission to Phys. Rev. Lett. as:

L.A. Lubbers and M. van Hecke, *Excess floppy modes in metamaterials with symmetries.*

4.1 Introduction

The aim of this chapter is to gain insight into the nature and multiplicity of the excess zero modes that we numerically characterized in chapter 3. First, for the generic case the number of zero modes and states of self stresses can be determined by the pebble game [47, 48], a discrete algorithm that is exact in two dimensions and for generic quads. For symmetric quads however, this algorithm is not suitable. We therefore focus on gaining an approximate, yet accurate, understanding of the number of (excess) zero modes in diluted symmetric systems, which will be topology-based.

We start from the observation that the occurrence of excess modes is driven by densely connected patches, which are rigid in the generic case but, irrespective of size, feature a hinging mode in symmetric systems. Hence, we would like to consider our systems as connected groups of quads, that we will refer to as clusters, and in section 4.2 we give precise definitions that allow us to separate any system in a collection of clusters, connectors and remaining quads. We show examples of this partition, and point out that the remaining quads do not significantly contribute to Δ, as they almost equally contribute to n_s and n_g. We therefore define so-called *pruned* systems, where the remaining quads are removed, and that solely consist of clusters and connectors — we show that Δ for the full system and Δ' for the pruned systems are extremely close in section 4.3. In section 4.4 we consider the three distinct type of connectors that arise between two clusters, and show how they constrain the number of (excess) zero modes. We find that clusters with a sufficient number of connectors should be seen as a single cluster, and develop an iterative cluster merging algorithm. Finally, in section 4.5 we apply this topology-based iterative algorithm to determine n_s' and Δ' for the pruned systems, and show very close correspondence to the numerically obtained Δ'.

4.2 Clusters on the square and dual grid

In this section we introduce the notion of 4-blocks, that, once detected, can be used to unambiguously detect clusters, connectors and remaining quads. A 4-block consist of four quads connected in a loop [Fig. 4.1(a)] and has one internal degree of freedom. A quad can belong to one or

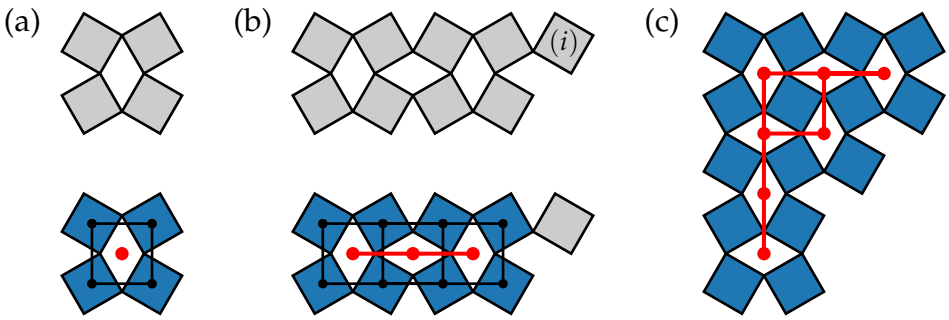

Figure 4.1: Detection of 4-blocks. Systems are initialized with grey quads, which are marked blue if they belong to a 4-block. The square and dual grid associated with the 4-blocks are respectively shown in black and red. (a-b) The top rows show unmarked quads of (a) a single 4-block and (b) a strip with one dangling quad, quad (i). The bottom rows display the associated square and dual grid, and the marked quads. (c) (Square grid not shown) As an additional example we show the dual grid of a large system that is not strip-like.

more 4-blocks, as is for example the case for the strips and loops (linearly connected 4-blocks) described in section 3.1; a quad can also belong to zero 4-blocks, such as quad (i) of the system shown in Fig. 4.1(b).

Formally, the presence of a quad in a diluted system can be expressed as the filling of a node on a square-like grid* (Fig. 4.1). Similarly, the presence of a 4-block can be expressed by filling a node on a dual, square-like grid, whose nodes lie in the center of each 4-block (Fig. 4.1). In a first step, we detect all 4-blocks, and track the quads of all 4-blocks [Figs. (4.1-4.2)]. After detecting all 4-blocks and filling the dual grid accordingly, we note that adjacent nodes on the dual grid correspond to 4-blocks that are connected and are part of the same cluster, and we thus connect these dual nodes [red lines in Figs. (4.1-4.2)]. Subsequently, we assign the same colour to all quads that belong to these connected 4-blocks, and use different colours for 4-blocks that are disconnected on the dual grid (Fig. 4.2). This procedure yields an unambiguous detection of clusters: As illustrated for the systems in Fig. 4.2, we have identified and coloured all connected 4-blocks, and find that each quad belongs to either zero (grey), one (colour) or in some cases, two clusters (bi-colour).

*For the generic quads, there is no regular underlying lattice. Nonetheless, the connectivity and topology of such networks are equivalent to that on a square lattice.

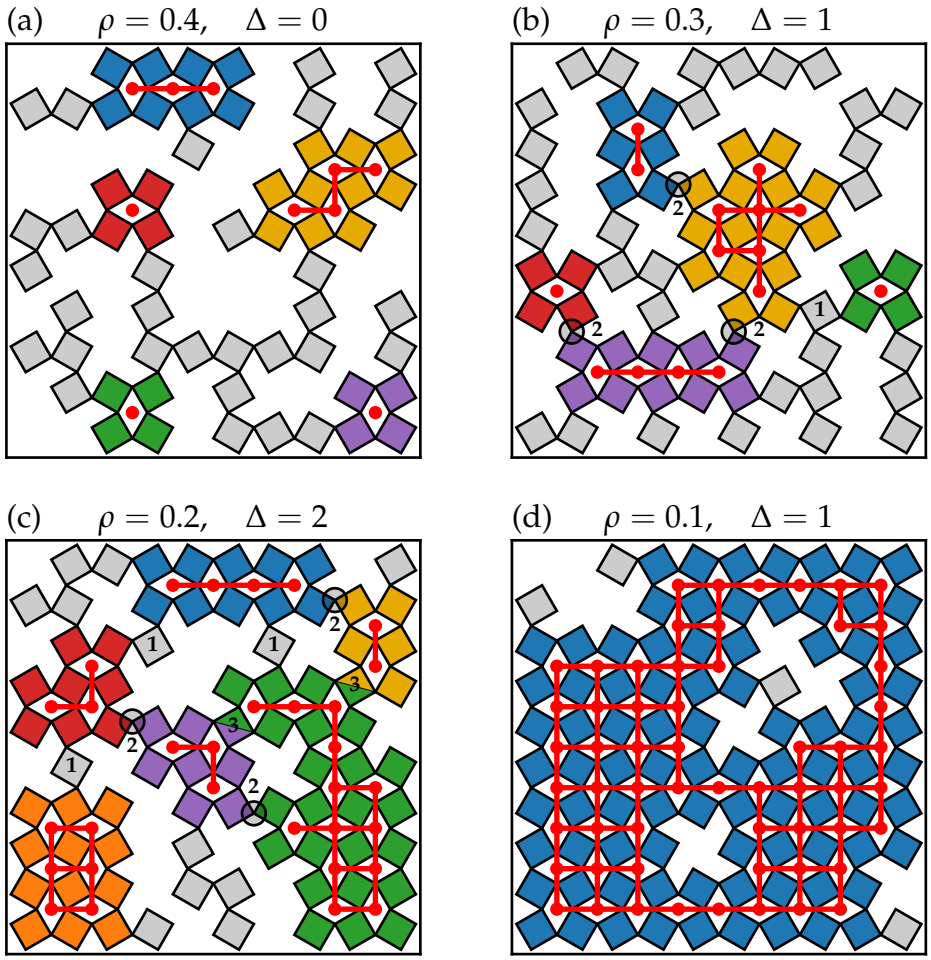

Figure 4.2: Clusters on the dual grid. Distinct clusters are indicated by different colours; the red nodes and lines display the dual grid. (a-d) Four independent randomly diluted systems of varying cutting fraction, shown from high to low ρ. The actual quads of different clusters can connect in three different manners, as indicated by the numbers 1, 2 and 3: Via a grey quad (type 1), direct connection (type 2, marked by small circles) or an shared quad (type 3 and bi-coloured). All grey quads that are not type-1 are remaining quads.

Distinct clusters can be connected in three different manners, as indicated by the numbers in Fig. 4.2, of which a more detailed overview is provided in Fig. 4.8. First, a grey quad may connect to two clusters and we will call this a type-1 connector [Fig. 4.8(a)]. Second, two clusters may directly be connected, leading to a type-2 connector [Fig. 4.8(b)]. Third, two clusters may share a quad, leading to a type-3 connector [Fig. 4.8(c)]. These names are not arbitrary — in what follows we will show that these lead to one, two or three constraints.

Finally, grey quads that are not type-1 connectors are classified as remaining quads. In the following section we will discuss the relevance of the remaining quads and show that most of these are not relevant for Δ. Altogether, in this section we have developed the notion of 4-blocks which allows us to partition any randomly diluted system into clusters, connectors and remaining quads.

4.3 Pruned systems

We now define pruned systems, where most of the remaining quads are removed, motivated by the aim to study the nature and multiplicity of the excess zero modes in the simplest possible setting. We therefore demonstrate that remaining quads contribute almost equally to n_s and n_g, and can thus be pruned without significantly altering Δ. The only remaining quads that easily can be detected and understood to have the potential to change Δ, are self-connectors — isolated quads that are connected to the same cluster [examples are shown in Fig. 4.2(d) and Fig. 4.6(a)]. These never modify n_s, but they may rigidify an otherwise hinging generic cluster, and we have therefore kept these self-connectors in our pruned systems. All other remaining quads are removed. In the following we describe the average number of excess zero modes in the pruned systems by $\langle \Delta' \rangle(\rho, N)$, with ρ the cutting fraction of the full systems, to facilitate comparison with Δ.

In Fig. 4.3 we have visualized the pruned systems that correspond to the full systems shown in Fig. 4.2. For each of these examples we find that the number of excess zero modes before and after pruning is the same ($\Delta = \Delta'$). One can understand this intuitively by noting that the remaining quads form dangling and floppy groups that equally contribute to n_s and n_g. Nonetheless, a quantitative comparison of the ensemble

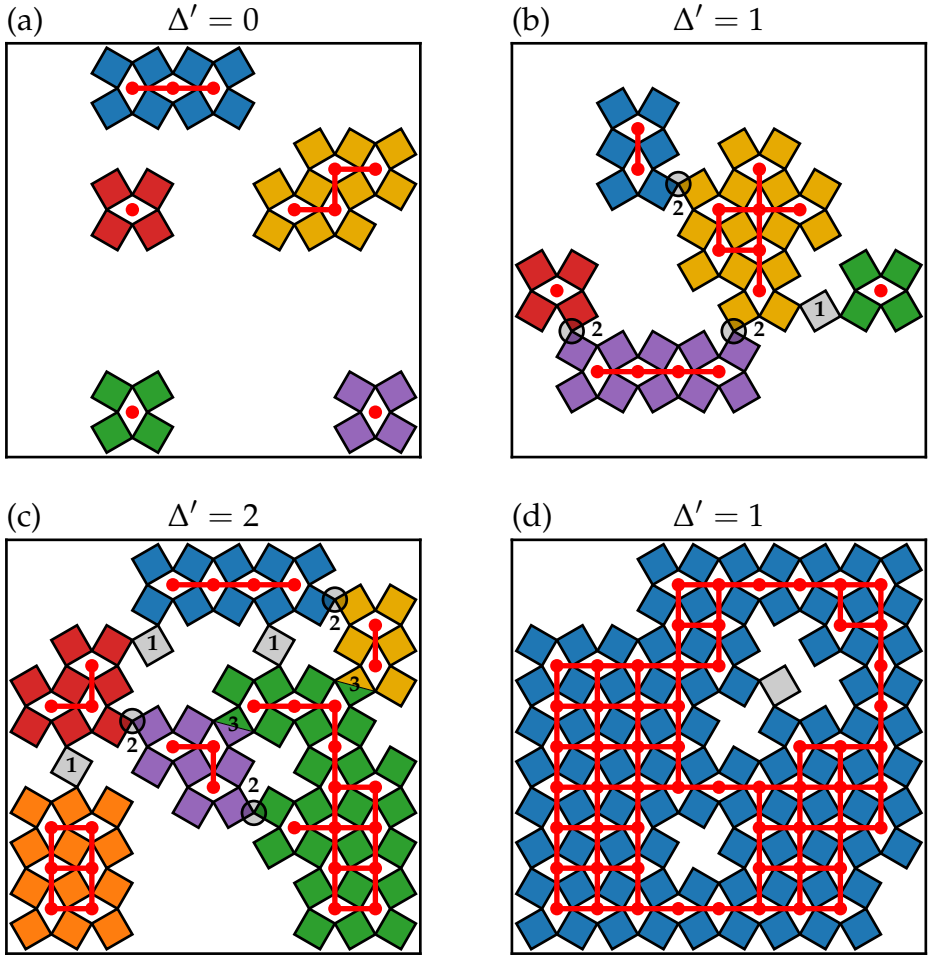

Figure 4.3: Pruned versions of the systems show in Fig. 4.2. Note that $\Delta' = \Delta$ for each of these examples.

averages $\langle\Delta\rangle$ and $\langle\Delta'\rangle$ as function of ρ and N, as obtained from another series of independent simulations, shows slight differences in the number of excess modes of pruned and full systems can occur (Fig. 4.4). As can be observed from panel (a), the curves $\langle\Delta\rangle(\rho, N)$ (solid lines) and $\langle\Delta'\rangle(\rho, N)$ (dashed lines) are essentially indistinguishable, but $[\langle\Delta'\rangle - \langle\Delta\rangle] / \langle\Delta\rangle^{\star}$, as plotted in panel (b), reveals differences that are most pronounced for intermediate cutting fractions. Here, $\langle\Delta\rangle^{\star}$ denotes the peak value of $\langle\Delta\rangle$.

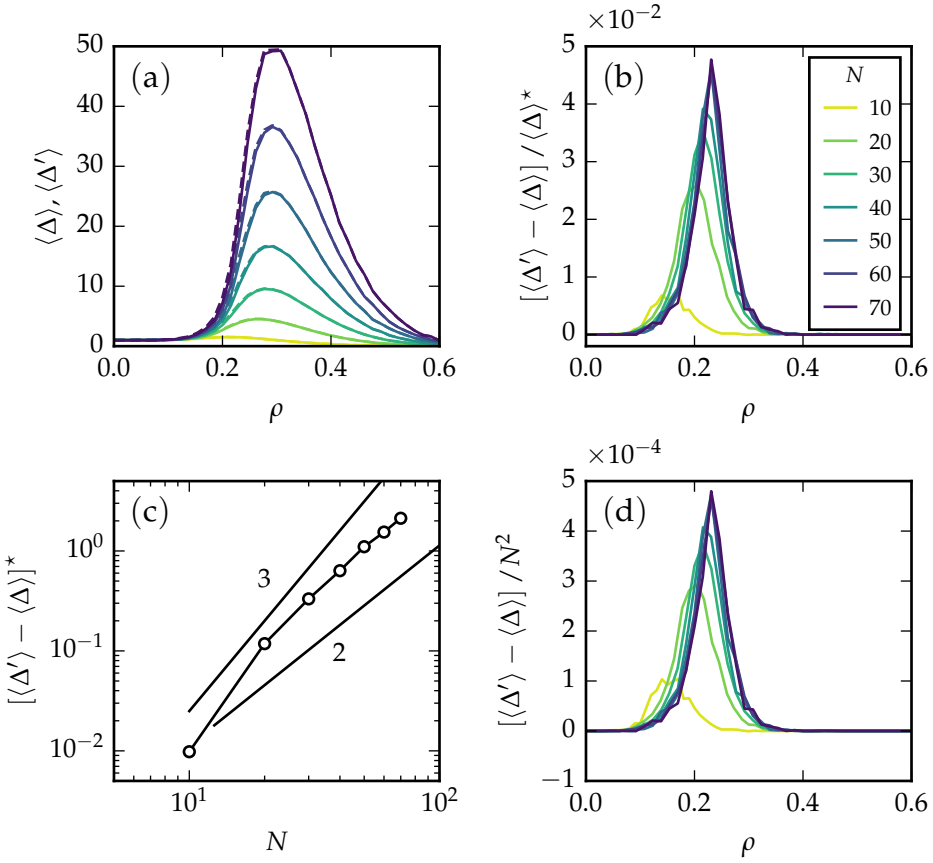

Figure 4.4: Excess zero modes in full and pruned systems, for a range of system sizes. (a) The average number of excess modes as function of ρ for full ($\langle\Delta\rangle$, solid lines) and pruned ($\langle\Delta'\rangle$, dashed lines) systems for a range of system sizes. (b) Deviations as compared to the peak value of the full systems, $\langle\Delta\rangle^\star$, show that relative deviations are maximally 5% for the system sizes considered. (c) The peak value of $\langle\Delta'\rangle - \langle\Delta'\rangle$ as function of N. (d) Deviations rescaled by N^2.

As can be seen, these relative differences never exceed 5% for the system sizes considered. In panel (c) we show the peak value of the deviations, $[\langle\Delta'\rangle - \langle\Delta\rangle]^\star$, as function of N. This shows that the deviations grow rapidly for small N, but for larger N, our data is consistent with a crossover to N^2 scaling — to accurately measure the asymptotic scaling exponent much larger system sizes are required. For completeness, in

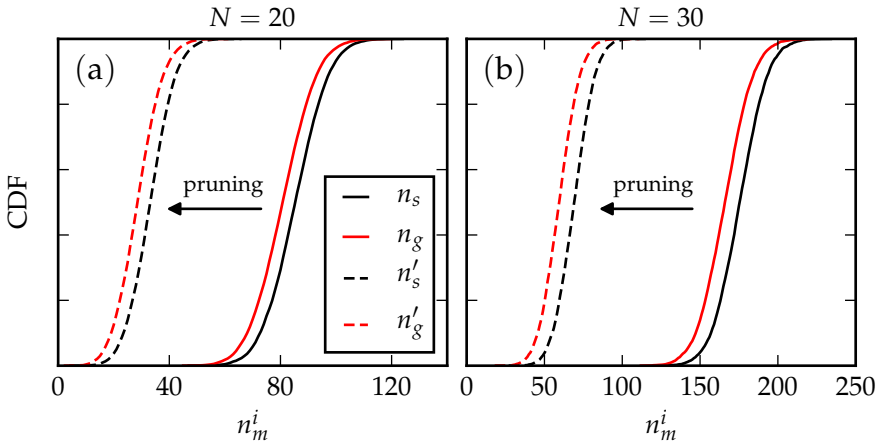

Figure 4.5: CDFs for the number of internal zero modes (n_m^i) in full and pruned systems, in the peak regime of $\langle\Delta\rangle$. The solid curves display data for the number of zero modes in the full symmetric (n_s) and generic systems (n_g); the dashed curves display data for the pruned symmetric (n'_s) and generic systems (n'_g). We show data for system sizes (a) $N = 20$ and (b) $N = 30$.

panel (d) we show the deviations rescaled by N^2, which leads to a reasonable collapse for large N. Our data thus suggests that the difference between $\langle\Delta\rangle$ and $\langle\Delta'\rangle$ is extensive. Altogether, these findings demonstrate that pruned systems accurately capture the excess zero modes of full systems, which allows us to study the nature and multiplicity of the excess zero modes in the simpler pruned systems.

To further show that pruned systems well describe the full systems, we also display some ensemble distributions of Δ and Δ' as CDFs in Fig. 4.5, for ρ that corresponds to the peak location of $\langle\Delta\rangle$. For both system sizes that are shown in Fig. 4.5, we observe a very similar translation of n_s and n_g as a result of pruning. These findings therefore further support that the number of excess zero modes in the full and pruned system are very close.

Finally, to gain insight in the cause of deviations between Δ and Δ', and the role of self-connectors, consider the three examples shown in Fig. 4.6. First, the strip-like cluster in panel (a) displays a typical example illustrating why we do not prune self-connectors; by keeping this self-connector, we find that $\Delta = \Delta' = 1$. In contrast, where we to prune

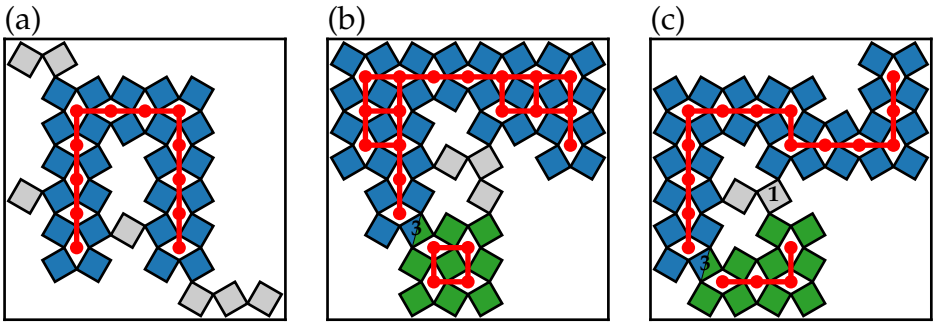

Figure 4.6: Cutting patterns that illustrate the role of self-connectors and deviations between Δ and Δ'. (a) Pruning this system while keeping the self-connector yields $\Delta = \Delta'$, whereas we would find $\Delta'' = 0$ if we additionally prune the self-connector. This illustrates that self-connectors rigidify hinging generic strips. (b-c) Cutting patterns for which pruning of remaining grey quads changes the number of excess zero modes ($\Delta \neq \Delta'$). Note that these examples do not contain self-connectors, such that $\Delta' = \Delta''$.

all remaining quads, we would find that $\Delta'' = 0$. The second and third example [panel (b-c)] display cutting geometries that do not contain self-connectors, but for which $\Delta \neq \Delta'$. These have to do with more complex clusters of remaining quads that, in general, will be hard to detect. Nonetheless, as we have shown in Fig. 4.4, deviations such as as displayed in Fig. 4.6(b-c) are rare and Δ and Δ' are very close.

4.4 Topology based counting argument

We now explain how we develop a counting argument to estimate n_s' from the topology of the clusters and their connectors. To establish this counting argument we will utilize the generalized Maxwell count [Eq. (3.3)], which can be adapted to the context of clusters (explicitly indicated by the superscript c) as:

$$N^c_{\text{dof}} - N^c_{\text{con}} = n^i_m + 3 - n^c_{ss}. \tag{4.1}$$

In the above equation, N^c_{dof} represents the number of internal and rotational/translational degrees of freedom of the clusters and N^c_{con} the

number of constraints of their associated connectors†. We note that large clusters feature a significant number of internal states of self-stress, but these we will ignore. However, when clusters are coupled, new states of self-stress may arise and we count these by n_{ss}^c. Hence, we see the clusters as 'black boxes' that can rotate, translate, and hinge — all internal states of self-stress are ignored. Thus, n_{ss}^c describes the number of redundant inter-cluster constraints given by the type 1,2 and 3 connectors. Lastly, recall that n_m^i expresses the number of internal zero modes, with $n_m^i = n_s'$ for symmetric systems. We furthermore note that Eq. (4.1) also applies to generic systems with $n_m^i = n_g'$, but as motivated already, our main focus is to count the number of zero modes in symmetric systems, rather than the zero modes in generic systems where exact algorithms to count these already exist [47, 48].

Below we first discuss how the number of (excess) zero modes can be determined in the simplest scenario in which connectors are absent ($N_{\text{con}}^c = n_{ss}^c = 0$). Subsequently, we consider systems in which connectors are present and explain how to correctly take the N_{con}^c constraints and n_{ss}^c self-stresses into account. Finally, we present a step-wise analysis of a (randomly diluted) system that exemplifies how our methodology can be applied to successfully count n_s'.

4.4.1 Counting without connectors

In the simplest scenario, there are no connectors between clusters and inter-cluster self-stresses are absent ($n_{ss}^c = 0$) — this typically occurs at either low [Fig. 4.3(d)] or high cutting fractions [Fig. 4.3(a)]. We now show that — in the absence of connectors — we can estimate the number of (excess) zero modes from a simple argument based on the multitude of clusters.

Using Eq. (4.1) we first note that $n_m^i = N_{\text{dof}}^c - 3$ in the absence of connectors. For symmetric systems, all clusters are hinging, and each cluster contributes 4 degrees of freedom. For a randomly diluted system that contains n_c clusters, we therefore immediately obtain $n_s' = 4n_c - 3$. To determine the number of *excess* zero modes we also need to obtain n_g'. In principle, our goal is not to develop a counting argument for n_g', since

†The constraints introduced by the connectors should not be confused with the internal constraints of an individual cluster. The internal constraints constitute clusters, but do not constrain the motion between adjacent clusters.

this is already captured by the pebble game [47, 48]. However, in the very special case where constraints and inter-cluster self-stresses are absent, we can approximate the outcome of the pebble game using a simple argument — which helps us to gain insight into the nature and multiplicity of the excess zero modes. We therefore proceed by providing an approximate counting method for n'_g.

To determine n'_g we need to distinguish hinging clusters and rigid clusters. For generic systems we have discussed before that while strips have one hinging mode, larger clusters are rigid; generic clusters can therefore either contribute 3 (rigid clusters) or 4 (hinging clusters) degrees of freedom. Assuming that of the n_c clusters, n_r are rigid and n_h are hinging, we obtain $n'_g = 4n_h + 3n_r - 3$. Combining the expressions for n'_s and n'_g, this yields the rigid-cluster-based estimate $\Delta_r = n'_s - n'_g = n_r$, demonstrating that the number of excess zero modes is tantamount to the number of rigid clusters in the absence of connectors. Hence, excess modes are induced as a result of sufficiently large clusters that are rigid in the generic case, but retain their hinging mode in the symmetric case.

Comparison of Δ_r and exact results — We now systematically compare the rigid-cluster-based prediction $\langle \Delta_r \rangle(\rho, N)$ (dashed lines) and the exact results $\langle \Delta \rangle(\rho, N)$ (solid lines) based on the Hessian matrix, as obtained from a large number of independent simulations. These simulations are based on two assumptions: First, we did not prune these systems to reduce numerical computation time, as this circumvents the need to detect remaining quads and connectors. This does not affect the outcome for the number of rigid clusters. Second, counting of the number of rigid clusters is approximate. A sufficient condition for rigidity is that somewhere in the cluster dual nodes are connected in a loop. We detect the most common loop that occurs in dense clusters, where one or more primitive loops of length four occur [Fig. 4.1(c)]. In principle, the smallest loop on the dual grid can be longer than four [e.g. as in Fig. 3.3(c)]. However, these cases are rare and yield a negligible overestimation of n_r, which therefore does not affect the main findings we will discuss now.

In Fig. 4.7 we display $\langle \Delta_r \rangle(\rho, N)$ (dashed lines) and the exact results $\langle \Delta \rangle(\rho, N)$ (solid lines). As can be observed from Fig. 4.7(a), $\langle \Delta_r \rangle$ qualitatively captures the peak behaviour of $\langle \Delta \rangle$ and yields, as expected, an excellent approximation for large cutting fractions; in this regime the sys-

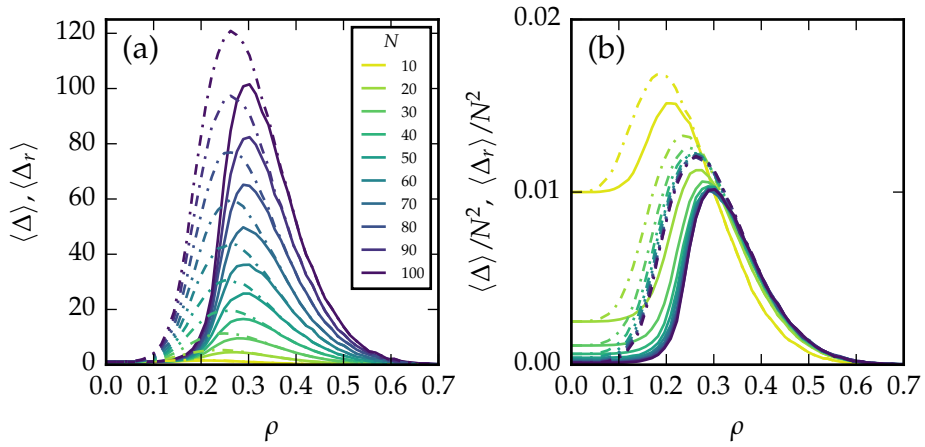

Figure 4.7: Comparison of the average number of excess zero modes predicted by exact calculations $\langle\Delta\rangle(\rho)$ (solid lines) and the simultaneous rigid-cluster-based approximation $\langle\Delta_r\rangle(\rho)$ (dashed lines), for a range of system sizes. We have used the same ensemble size for each N as in Fig. 3.12 for the data shown. (a) $\langle\Delta_r\rangle$ shows excellent agreement with $\langle\Delta\rangle$ for cutting fractions beyond the peak location of $\langle\Delta\rangle$. (b) Scaling collapse of $\langle\Delta\rangle$ and $\langle\Delta_r\rangle$ in the $N \to \infty$ limit for the data shown in panel (a).

tems contain a few rigid clusters as well as numerous isolated hinging clusters and floppy groups of loosely connected quads — only the rigid clusters contribute to Δ. In contrast, $\langle\Delta_r\rangle$ displays significant deviations from $\langle\Delta\rangle$ for intermediate ρ. Comparison of the large N asymptotics of $\langle\Delta_r\rangle$ —which similar to $\langle\Delta\rangle$ scale as N^2— with the asymptotics of $\langle\Delta\rangle$ shows that these deviations are characterized by a peak value which is consistently overestimated, and a peak location with a slight offset to the left [Fig. 4.7(b)].

The observed deviations expose the effect of connectors. For intermediate ρ the clusters are strongly entangled by connectors of type 1,2 and 3 and consideration of their associated self-stresses is necessary to accurately estimate n_s' and n_g'. As discussed before, in the generic case there exists an exact algorithm to determine n_g' and the self-stresses. However, in the symmetric case this algorithm is not suitable and our main goal therefore is to develop an approximate counting argument for the number of (excess) zero modes and self-stresses in these systems.

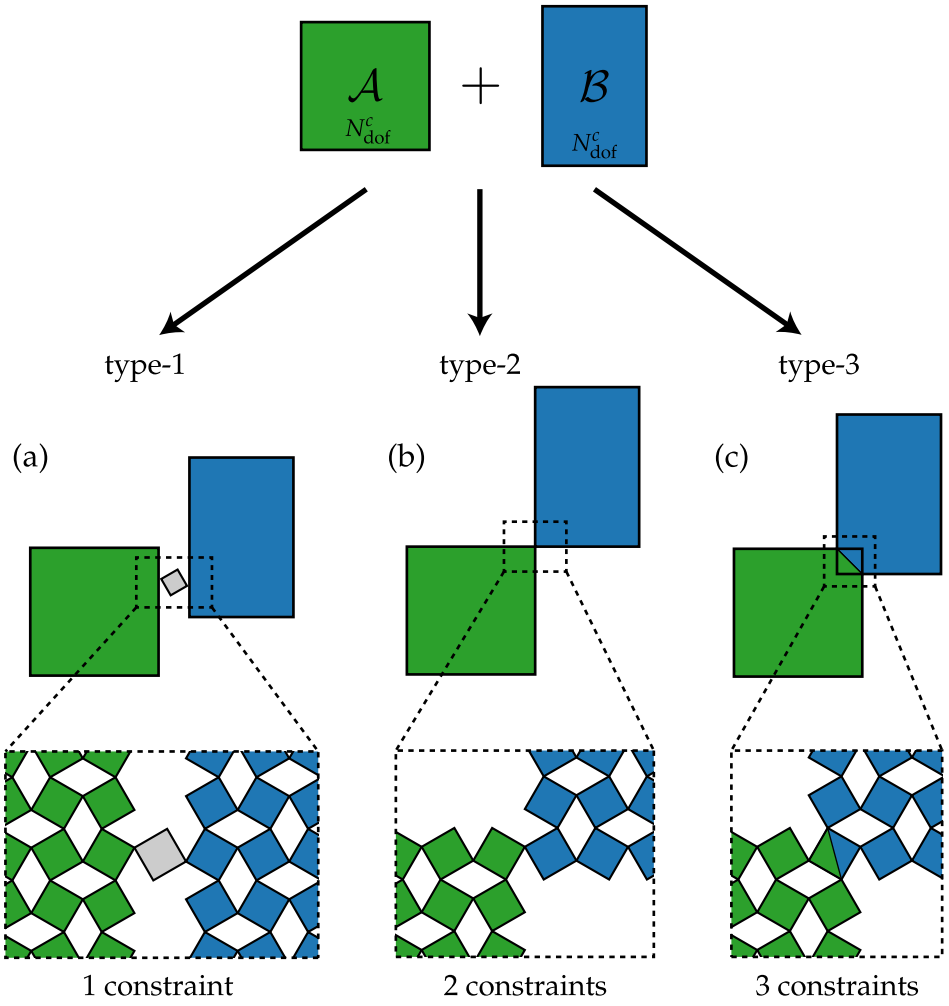

Figure 4.8: Cluster connector types. There exist three distinct manners in which clusters $\mathcal{A}$ and $\mathcal{B}$ may be connected, namely via a type-1 (left), type-2 (middle) or type-3 (right) connector. These connectors, according to their names, introduce precisely 1, 2 or 3 constraints, as is indicated at the bottom of the figure. In the main text we provide a derivation for the number of constraints associated with each connection type.

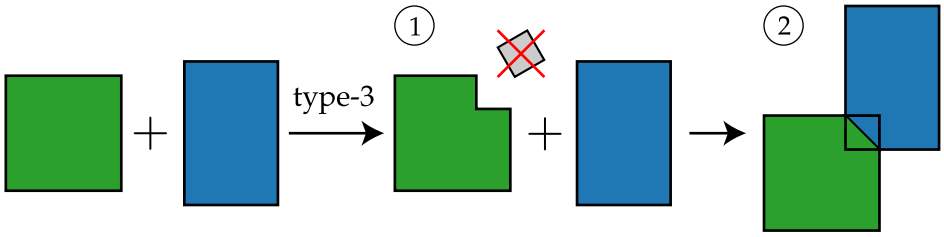

Figure 4.9: Step-wise explanation of connection type-3. In step 1, the upper right quad of the green cluster is removed and two associated bonds are cut. In step 2 both clusters are connected and two bonds are restored, leading to no net change in the number of bonds and the net removal of 3 degrees of freedom. Hence, the number of zero modes as a result of the type-3 connection is lowered by 3.

4.4.2 Connectors, constraints and inter-cluster self-stresses

Before presenting a counting argument that takes into account connectors, we now first show that connectors of type 1,2 and 3, conform to their names, introduce precisely 1, 2 and 3 constraints when connecting a pair of clusters. Moreover, we explain the appearance of inter-cluster self-stresses as a result of these connectors.

Connectors and constraints. — To evidence the mentioned number of constraints associated with each connection type, we consider a system that consists of two clusters, $\mathcal{A}$ and $\mathcal{B}$, and determine how n_s of this two-cluster system is lowered for each connection type. In Fig. 4.8 we display a detailed graphical representation of the three distinct manners in which cluster $\mathcal{A}$ and $\mathcal{B}$ can be connected. Before the clusters are connected $n_s = N^c_{\text{dof}} - 3 = 5$, where each cluster contributes 4 degrees of freedom. These 5 zero modes should be interpreted as the independent hinging of both clusters (2 zero modes) and relative translations or rotations of the clusters (3 zero modes). After the clusters are connected by a type 1, or 2 or 3 connector, some of their relative motions become constrained, and n_s will respectively be lowered by one, two or three — which is equivalent to the presence of one, two or three constraints. To understand these connectors add one, two or three constraints, consider the zoomed areas in Fig. 4.8. First, for a type-1 connection the grey quad adds 3 degrees of freedom and 2 extra bonds, hence we lose one zero mode. Second, a

type-2 connection introduces a single additional bond, hence we lose two zero modes. Third, a connection type-3 is more subtle and can be seen as removing a single quad (three degrees of freedom), without adding new bonds, thereby lowering the number of zero modes by three. This is illustrated in more detail in Fig. 4.9.

Inter-cluster self-stresses. — Above we have illustrated the lowering of n_s as a result of a *single* type-1, *or* type-2, *or* type-3 connector. To understand the role of self-stresses we now consider the same two-cluster in the presence of *multiple* connectors and note that the lowering of n_s is bound to the minimum $n_s = 1$; coupled symmetric clusters always attain a global hinging mode, regardless of the number of constraints these share. As an example, consider the two-cluster system shown in Fig. 4.10 that contains two type-3 connectors (6 constraints). For this system one can readily envision that the connectors constrain all relative motions of the green cluster with respect to the blue cluster (and vice versa); the system only allows for a single dependent internal zero mode in which the motions of both clusters are coupled — global hinging. The cluster pair is dependent, acts as a single cluster with $n_s = 1$, and from Eq. (4.1) we accordingly find that the clusters share 2 inter-cluster self-stresses ($n^c_{ss} = 2$). Hence, the system contains 2 *degenerate* (redundant) constraints.

The example discussed above illustrates a general observation which is most easily understood by the consideration of Table 4.1. Here we tabulated n_s and n^c_{ss} as function of the number of constraints (N^c_{con}), where

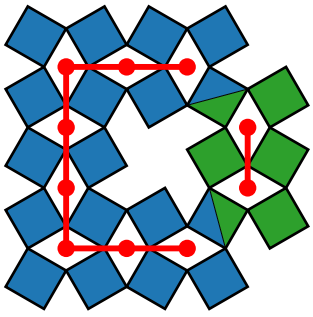

Figure 4.10: The clusters in this system exhibit no relative motions ($n_s = 1$) due to two type-3 connectors and effectively thus behave as a single cluster.

two-cluster system		
N^c_{con}	n_s	n^c_{ss}
0	5	0
1	4	0
2	3	0
3	2	0
$\downarrow n_s$ constant $\downarrow$		
4	1	0
5	1	1
6	1	2

Table 4.1: Number of zero modes (n_s) and inter-cluster states of self-stress (n^c_{ss}), as function of the number of constraints (N^c_{con}) for a two-cluster system. For $N^c_{\text{con}} \geq 4$ the number of internal zero modes becomes constant, as indicated by the shaded region.

we note that N^c_{con} is related to the number of type-1,2 and 3 connectors via

$$N^c_{\text{con}} = n_1 + 2n_2 + 3n_3, \tag{4.2}$$

with n_1,n_2 and n_3 the number of type 1,2 and 3 connectors. Starting from two unconnected clusters ($n_1 = n_2 = n_3 = 0$), Table 4.1 clearly shows that for each constraint added, n_s is lowered by one. The lowering of n_s persists until all relative motions of the clusters become constrained ($n_s = 1$), which requires precisely 4 constraints. From this point, the presence of any additional constraints does no longer affect n_s, but leads to the development of inter-cluster self-stresses instead.

4.4.3 Counting including connectors

In this section we present a counting argument which is suitable for symmetric systems and that takes into account the presence of connectors. The challenge in counting n'_s is that that the number of inter-cluster self-stresses generally is non-zero: Whereas the left hand side of Eq. (4.1) is easily calculated based on the number of clusters and constraints of the connectors, we need to know n^c_{ss} in order to calculate n'_s. In what follows we therefore develop a counting method that *iteratively* eliminates

the inter-cluster self-stresses, yielding an hierarchy of predictions for n_s', based on the following methodology:

(i) Given a randomly diluted system, we first partition the system into clusters, connectors and remaining quads, and subsequently prune the system.

(ii) We merge clusters that share four or more constraints. This cluster coarsening eliminates (some of the) the inter-cluster self-stresses.

(iii) After the merging of clusters, we may find that new clusters have formed that again share four or more constraints — we iterate until no more clusters can be merged.

(iv) In each iteration step, we calculate the estimate for n_s' from the topology of the clusters and their connectors, according to

$$n_{s,i} = 4n_{c,i} - N^c_{\text{con},i} - 3, \tag{4.3}$$

where $n_{c,i}$ and $N^c_{\text{con},i}$ are the number of clusters and constraints associated with iteration step i.

We will now first clearly motivate this methodology, and then provide a worked-out example. Step (i) is straightforward and already explained in Sections (4.2-4.3). The merging of cluster pairs as described in steps (ii) and (iii) ensures inter-cluster states of self-stress become internal and do no longer contribute to n^c_{ss}, which circumvents the need to explicitly count these. For example, we could treat the system in Fig. 4.10 as two distinct clusters with 8 degrees of freedom, 6 constraints, 4 zero modes and 2 self-stresses, but the simpler approach is to merge the clusters into a single (unconstrained) cluster that features 4 degrees of freedom and zero inter-cluster self-stresses. A sufficient condition for merging is that two clusters share 4 (or more constraints); this condition is based on Table 4.1, which we used previously to motivate that clusters with four or more constraints are dependent and develop inter-cluster self-stresses. Finally, Eq. (4.3) as given in step (iv) is based on Eq. (4.1), where we note that the number of inter-cluster self-stresses does not appear in Eq. (4.3) as we tentatively assume $n^c_{ss} = 0$ after the cluster merging in each iteration step.

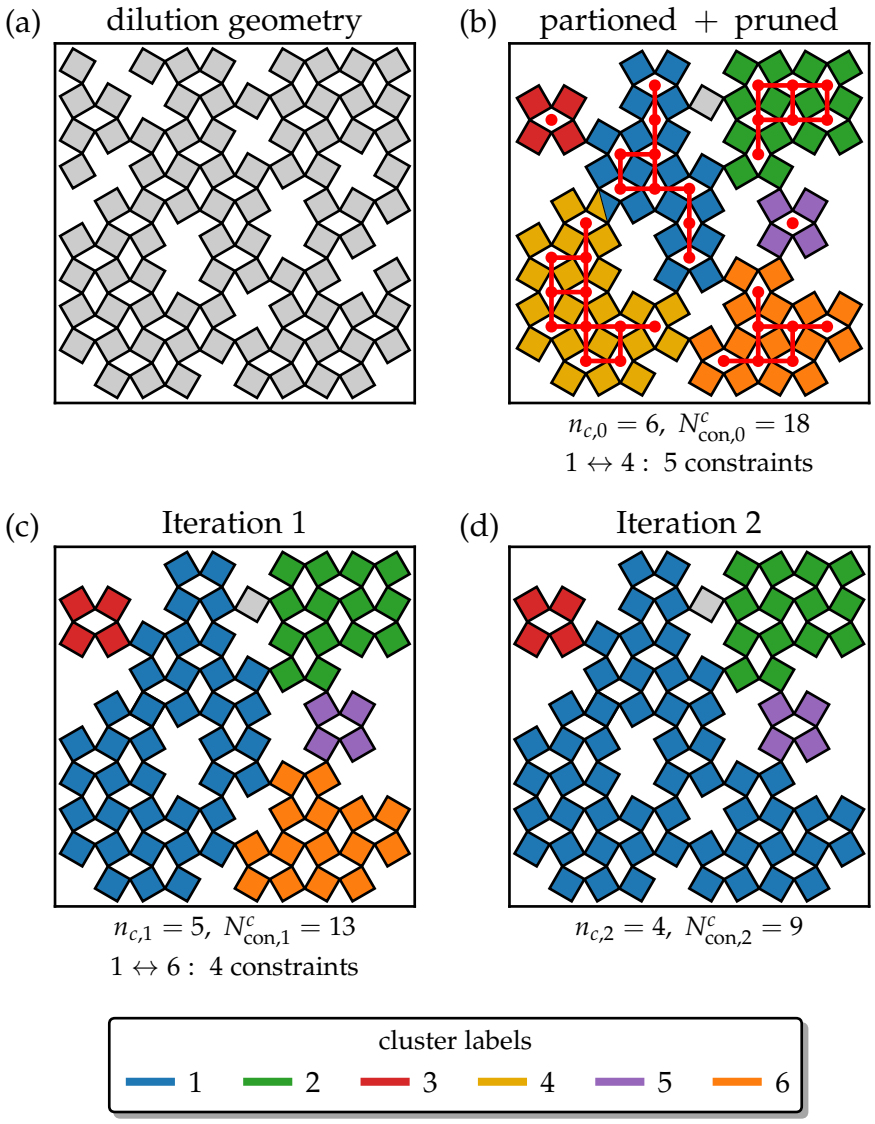

Figure 4.11: Visualization of the iterative merging of clusters to estimate n'_s (see main text). At the bottom of each of the respective panels we provide the number of clusters $n_{c,i}$ and constraints $N^c_{\text{con},i}$. The text '$\mathcal{A} \leftrightarrow \mathcal{B}$' additionally indicates the labels of cluster pairs $\mathcal{AB}$ that share sufficient constraints for merging. (a) Initial random dilution geometry. (b) Partitioned and pruned system. (c-d) Subsequent merging of clusters. For simplicity, the dual grid is only shown in panel (b).

Worked-out example. — To gain intuition for the iterative counting argument, we finalize this section by calculating the hierarchy of predictions $n_{s,i}$ for the system shown in Fig. 4.11(a). We will show that this system requires two merging iterations and that the result as obtained from the final iterated topology of the clusters and their connectors is in agreement with exact results based on the Hessian matrix, namely $n_s' = 4$.

initial estimate (no iterations) $(n_{s,0})$**. —** To obtain the initial estimate for n_s' we partition the randomly diluted system and prune the remaining quads [Fig. 4.11(b)]. From the resulting topology of the clusters and their connectors, we note that there are $n_{c,0} = 6$ clusters and $N^c_{\text{con},0} = 18$ constraints, tantamount to 1 type-1 connector, 7 type-2 connectors and 1 type-3 connector, and determine accordingly that $n_{s,0} = 4 \times 6 - 18 - 3 = 3$.

estimate for one iteration $(n_{s,1})$**. —** By inspection of the clusters and their connectors in Fig. 4.11(b) we find that clusters 1 and 4 are qualified for merging; these share 5 constraints (one type-2 and 3 connector), whereas all other cluster pairs share less than 4 constraints. We therefore merge cluster 1 and 4 by assigning these the same colour, which leads to the (new) topology of the clusters and their connectors as displayed in Fig. 4.11(c). Due to the cluster merging we lose 1 cluster, 1 type-2 connector and 1 type-3 connector, such that we now obtain that $n_{c,1} = 5$ and $N^c_{\text{con},1} = 13$. The new estimate therefore yields $n_{s,1} = 4 \times 5 - 13 - 3 = 4$.

estimate for two iterations $(n_{s,2})$**. —** Due to the formation of new clusters in the previous iteration [Fig. 4.11(c)], we now also find that clusters 1 and 6 qualify for merging. We therefore also merge these clusters to obtain the topology as shown in Fig. 4.11(d), for which we accordingly find that $n_{c,2} = 4$ and $N^c_{\text{con},2} = 9$. This yields the estimate $n_{s,2} = 4 \times 4 - 9 - 3 = 4$, which is also the final estimate since Fig. 4.11(d) contains no more clusters that satisfy the merging rule. We thus find that our result as obtained via counting is in agreement with the exact result based on the Hessian matrix, demonstrating that we can count n_s' from the topology of the clusters and their connectors. In the next section we test the general accuracy of this approach.

4.5 Counting of (excess) zero modes

In this section we compare exact results for the number of (excess) zero modes in symmetric systems, based on the Hessian matrix, against the topology based estimates that have been developed above. We in particular focus on the sequence of predictions for Δ', rather than n_s' itself, since the main goal of this chapter is to gain insight in the nature and multiplicity of the *excess* zero modes. We therefore define $\Delta_i = n_{s,i} - n_g'$, where $n_{s,i}$ follows from the iterative counting argument and n_g' from exact Hessian based calculations, and show that Δ_∞ (final iterated result) yields a tight lower bound on the exact Δ'. Finally, to understand deviations between Δ_∞ and Δ', we compare $n_{s,\infty}$ to n_s' and discuss a number of examples for which our iterative counting method is inaccurate.

4.5.1 Results

Here we test the accuracy of Δ_i as function of system size N and cutting fraction ρ, by comparing the average estimates $\langle\Delta_i\rangle(\rho,N)$ to the exact results $\langle\Delta'\rangle(\rho,N)$. In order to obtain $\langle\Delta_i\rangle$, we have numerically implemented the iterative counting method. This Python-based code automatically partitions each randomly diluted systems into clusters, connectors[‡] and remaining quads, and subsequently iteratively merges clusters that satisfies the merging rule. In this way we acquire Δ_i for a large number of independent randomly diluted systems, allowing us to obtain reasonably well statistically converged data for $\langle\Delta_i\rangle$ (we used the same ensemble sizes as described in section 3.3.2). Recall that $i = 0$ corresponds to the initial system for which no clusters have been merged yet. For $i = 1$ we have merged the clusters once, for $i = 2$ twice, etc. The final topology, which contains no more clusters that satisfy the merging rule, is denoted by $i = \infty$.

In Fig. 4.12 we show the average iterative predictions $\langle\Delta_0\rangle(\rho)$, $\langle\Delta_1\rangle(\rho)$, $\langle\Delta_2\rangle(\rho)$ and $\langle\Delta_\infty\rangle(\rho)$ and the exact result $\langle\Delta'\rangle(\rho)$ for two system sizes, $N = 10$ and $N = 90$. For clarity we do not display the estimates that fall in between $i = 2$ and $i = \infty$. As can be observed, the most naive approximation that neglects inter-cluster self-stresses, $\langle\Delta_0\rangle$, accurately captures

[‡]In appendix 4.A we explain how each connection type is numerically detected using the adjacency matrix of the system and of individual clusters.

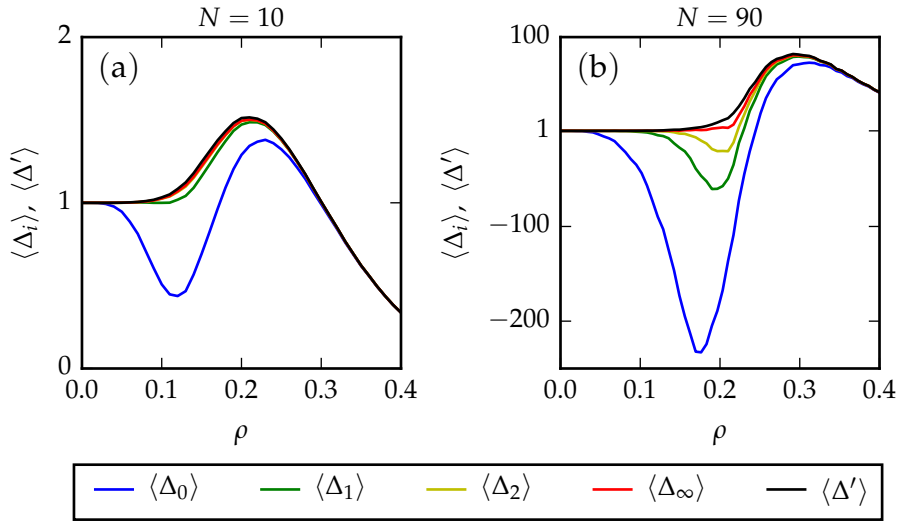

Figure 4.12: Iterative topology based estimates $\langle\Delta_0\rangle, \langle\Delta_1\rangle, \langle\Delta_2\rangle$ and Δ_∞ compared against the exact Hessian-based result $\langle\Delta'\rangle$. We show results for (a) $N = 10$ and (b) $N = 90$.

$\langle\Delta'\rangle$ for large cutting fractions, but displays significant deviations for intermediate cutting fractions. This finding is fully consistent with the expectation that inter-cluster self-stresses are present for strongly connected clusters (intermediate ρ), but absent for clusters that share few to none connectors (large ρ). The estimate after one merging iteration, $\langle\Delta_1\rangle$, already leads to a significantly improved estimate for the number of excess zero modes for each of the system sizes shown; the cluster merging eliminates a large number of self-stresses such that $\langle\Delta_1\rangle$ appears much closer to $\langle\Delta'\rangle$ than $\langle\Delta_0\rangle$. However, the new topologies of the clusters and connectors as obtained after one iteration again contain self-stresses such that $\langle\Delta_1\rangle$ still deviates from $\langle\Delta'\rangle$. The second merging iteration again eliminates these self-stresses, and as can be seen, $\langle\Delta_2\rangle$ yields an improved estimate for $\langle\Delta'\rangle$. The described improvement persists for the iterations thereafter ($i = 3,4..$) (not shown) up to the point where all of the clusters are merged, yielding the final estimate $\langle\Delta_\infty\rangle$. Fig. 4.12 demonstrates that we find very close correspondence of $\langle\Delta'\rangle$ and $\langle\Delta_\infty\rangle$ (which we will show to be a lower bound below) for each of the system sizes shown. Nonethe-

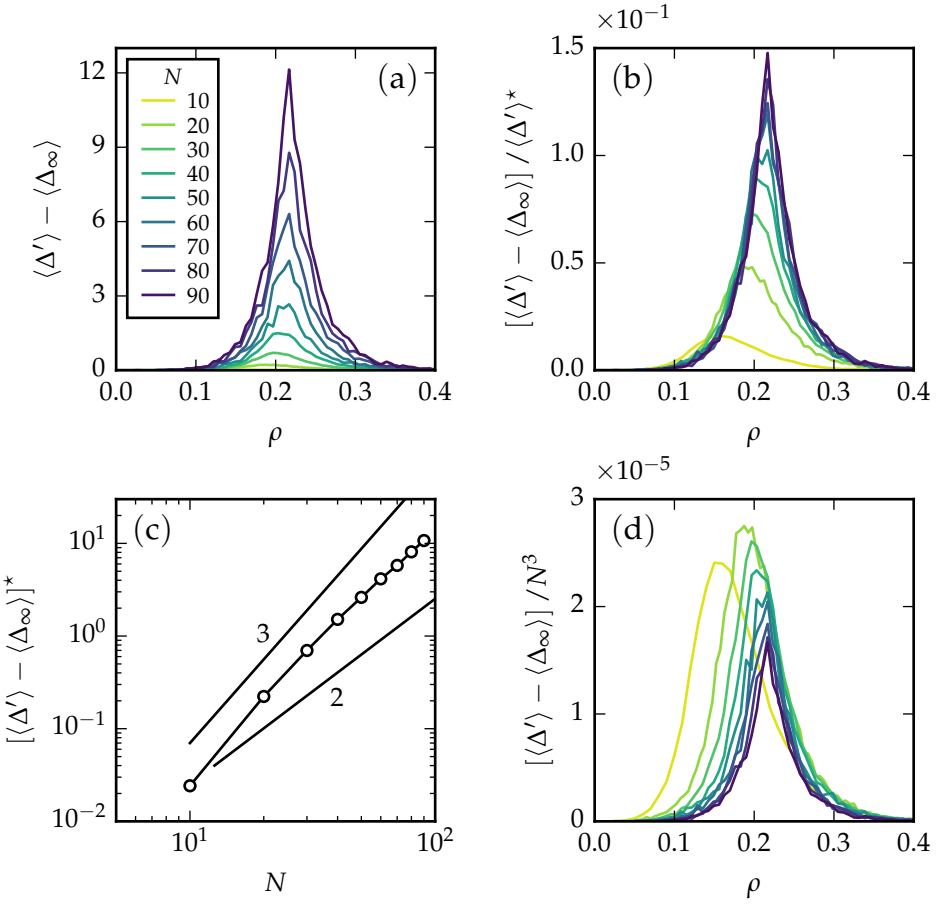

Figure 4.13: Comparison of $\langle\Delta'\rangle$ and $\langle\Delta_\infty\rangle$ for a range of system sizes. (a) The final deviations, $\langle\Delta'\rangle - \langle\Delta_\infty\rangle$ as a function of ρ. (b) Deviations as compared to the peak value of $\langle\Delta'\rangle$, $\langle\Delta'\rangle^\star$, show that relative deviations are maximally 15% for the largest system size considered ($N = 90$). (c) The peak value of $\langle\Delta'\rangle - \langle\Delta_\infty\rangle$ as function of N. (d) Deviations rescaled by N^3.

less, we observe small deviations between $\langle\Delta_\infty\rangle$ and $\langle\Delta'\rangle$, which implies the final iterated topologies contain remaining inter-cluster self-stresses.

In Fig. 4.13 we systematically compare $\langle\Delta'\rangle$ and $\langle\Delta_\infty\rangle$ for system sizes $N = 10, 20, \ldots, 80, 90$. Panel (a) shows that the final difference between our iterative counting method and the exact number of excess zero modes,

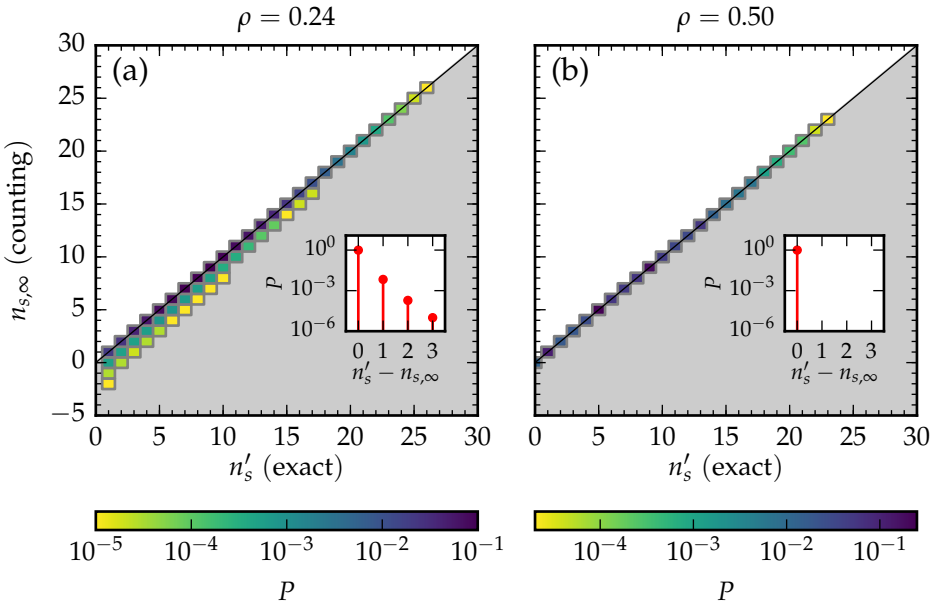

Figure 4.14: Discrete joint probability distributions as function of n_s' and $n_{s,\infty}$, for $N = 10$ and an ensemble size of 10^5 independent simulations. The solid black lines describe $n_s' = n_{s,\infty}$ and the shaded areas indicate the regions $n_s' > n_{s,\infty}$. (a) For $\rho = 0.24$ our counting method is exact for 99% of the simulations and yields a lower bound on n_s'. (b) For $\rho = 0.5$ our counting argument is exact for all simulations. Inset graphs: Discrete probability distribution of $n_s' - n_{s,\infty}$.

$\langle \Delta' \rangle - \langle \Delta_\infty \rangle$, grows with system size and is strongest for $\rho \approx 0.2$ (significantly below the peak location at $\rho \approx 0.3$). As can be seen in panel (b), we find that the relative deviations $[\langle \Delta' \rangle - \langle \Delta_\infty \rangle] / \langle \Delta' \rangle^\star$, with $\langle \Delta' \rangle^\star$ the peak average of $\langle \Delta' \rangle$, are maximally 15% for the largest system size considered. Panel (c) shows that the peak value of the deviations, $[\langle \Delta' \rangle - \langle \Delta_\infty \rangle]^\star$, initially grows faster than N^3, and then slowly crosses over to a smaller effective exponent; our data shows that this exponent is smaller than 3 [see panel (d)], and it is conceivable that ultimately deviations grow as N^2, i.e., are extensive, similar to the data in, e.g., Fig. 4.4.

Comparison of n_s' and $n_{s,\infty}$. — To understand the deviations between $\langle \Delta_\infty \rangle$ and $\langle \Delta' \rangle$ we now consider the discrete probability distributions as function of n_s' and $n_{s,\infty}$ in Fig. 4.14. Panel (a) demonstrates a general

and important feature of our iterative counting argument: $n_{s,\infty}$ yields a strict lower bound on n_s'. Deviations are rare, and occur when one or more connectors are degenerate (examples are discussed below), resulting in complex inter-cluster self-stresses that are not eliminated by our iterative merging method. According to Eq. (4.1) these remaining self-stresses yield an estimate for n_s' which is too low. Therefore, $n_{s,\infty}$ yields a lower bound on n_s', and accordingly, Δ_∞ yields a lower bound on $\langle \Delta' \rangle$. Nonetheless, our counting method provides an excellent approximation to n_s' — for $N = 10$ and $\rho = 0.24$ we find that our counting method is accurate in 99% of the cases [Fig. 4.14(a)]. Note that strongly diluted systems typically do not contain remaining self-stresses such that our counting method is exact for all simulations in that case [Fig. 4.14(b)].

We finally discuss two dilution patterns to illustrate the role of degenerate connectors that lead to complex inter-cluster self-stresses that are not eliminated by the iterative merging procedure (Fig. 4.15). In panel (a) we show 3 clusters that are connected in a loop and in this system none of the clusters satisfies the merging rule. Therefore, we estimate $n_{s,\infty} = 12 - 9 - 3 = 0$ (we count 4 clusters and 9 constraints). However, the correct answer is $n_s' = 1$; the system attains a global hing-

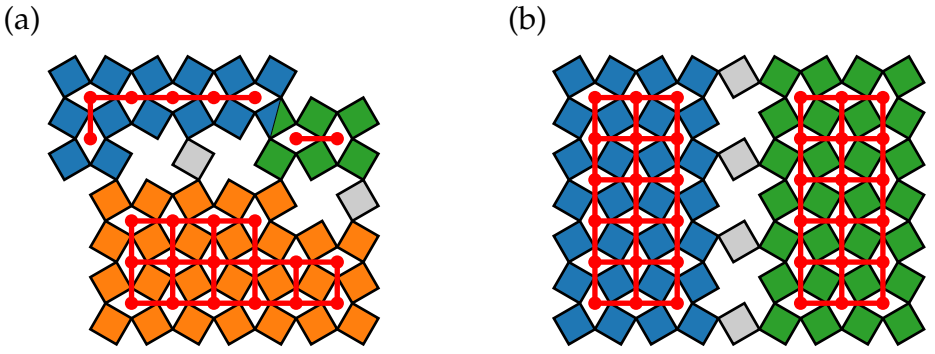

Figure 4.15: Dilution examples that contain special cases of degenerate connectors. (a) In this example the upper left type-1 connector is degenerate, but not eliminated by the iterative merging. This system has one excess zero mode $(n_s' = 1, n_g' = 0)$. (b) The two clusters shown satisfy the merging rule in principle, but can nonetheless be sheared with respect to each other. This system has three excess zero modes $(n_s' = 3, n_g' = 0)$.

ing mode. Apparently, the system contains one redundant constraint, and we have numerically confirmed the upper left type-1 connector (connector between the blue and orange cluster) is redundant; its removal does not change the numerically obtained value for n_s'. In panel (b) we show two clusters that share 4 type-1 connectors on row 1,3,5 and 7. In principle, these two clusters satisfy the merging rule, but one can readily understand that the connectors for this special geometry do not constrain all of the relative motions — the clusters can always shear with respect to each other. Therefore, the estimate $n_{s,\infty} = 1$ is incorrect, and we numerically confirmed that $n_s' = 3$ (global hinging + shear + a quartic mode). We moreover numerically found that one can add an infinite amount of type-1 connectors on every odd row (e.g. 1,3,5,7,9,...) without reducing the number of zero modes; the minimum number of type-1 connectors for $n_s' = 3$ is two, every connector added thereafter is degenerate. Both of the discussed geometries show examples of complex inter-cluster self-stresses that are not correctly taken into account by the iterative merging. Nonetheless, as we have shown in Fig. 4.13, deviations introduced by such special dilution geometries are relatively small.

4.6 Conclusions

We developed an approximate counting method for the number of (excess) zero modes in systems of hinging squares. We therefore first presented a procedure to partition any randomly diluted system into clusters, connectors and remaining quads. We then showed that pruning of the remaining quads does not significantly affect the number of excess zero modes, which allowed us study the nature and multiplicity of the excess zero modes in the simplest possible setting, where quads that are irrelevant for Δ are removed. To develop the counting argument we subsequently treated the clusters as 'black boxes' that can rotate, translate and hinge, showed how each of the three types of connectors constrains the number of zero modes and developed an iterative cluster algorithm to take into account the inter-cluster self-stresses that appear between sufficiently strongly connected clusters. Finally, we compared the predictions of our iterative counting argument against exact Hessian-based results for a large number of independent randomly diluted systems, and showed that we obtain a tight lower bound on $\langle \Delta' \rangle$.

Appendix

4.A Detecting cluster-constraints

In this appendix we explain the algorithms devised to detect type 1,2 and 3 constraints [Figs. (4.16-4.18)]. To demonstrate these algorithms we will use a simple system that consists of two clusters, denoted $\mathcal{A}$ and $\mathcal{B}$. Quads that belong to cluster $\mathcal{A}$ are coloured blue, quads that belong to cluster $\mathcal{B}$ green, and quads that belong to neither of those are coloured grey.

4.A.1 Type 3 constraint

Type 3 constraints are fairly easy to detect in comparison to type 2 and 1 constraints. This is because two clusters connected through a type 3 constraint share a quad, as depicted in Fig. 4.16. Therefore, it suffices to find the intersections of the set of quads that belong to cluster $\mathcal{A}$ and $\mathcal{B}$. For the example shown, the set of quads for both clusters are $\mathcal{A} = \{0,1,2,3\}$ and $\mathcal{B} = \{3,4,5,6\}$, such that the intersection equals $\mathcal{A} \cap \mathcal{B} = \{3\}$. The number of elements in the intersection then equals the number of type 3 constraints. When $\mathcal{A}$ and $\mathcal{B}$ are disjoint (no quads in common), the clusters encompass no type 3 constraints.

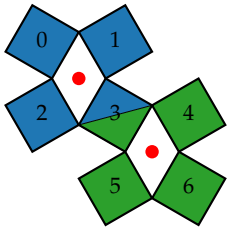

Figure 4.16: Type 3 constraint. Quad number 3 is shared between the blue and green cluster, as indicated by the bi-coloured quad.

4.A.2 Type 2 constraint

To detect type 2 constraints, we use the adjacency matrix of the system, C. This matrix indicates whether pairs of quads are adjacent: Element C_{ij} is set to one when quad i is adjacent to quad j, and zero otherwise. For

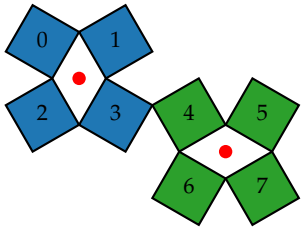

Figure 4.17: Type 2 constraint. The blue cluster ($\mathcal{A}$) and the green cluster ($\mathcal{B}$) are connected via quads 3 and 4.

the system shown in Fig. 4.17, the adjacency matrix is

$$C = \begin{array}{c} \text{label} \\ 0 \\ 1 \\ 2 \\ 3 \\ 4 \\ 5 \\ 6 \\ 7 \end{array} \begin{array}{c} \begin{array}{cccccccc} 0 & 1 & 2 & 3 & 4 & 5 & 6 & 7 \end{array} \\ \begin{bmatrix} \times & 1 & 1 & 0 & 0 & 0 & 0 & 0 \\ & \times & 0 & 1 & 0 & 0 & 0 & 0 \\ & & \times & 1 & 0 & 0 & 0 & 0 \\ & & & \times & 1 & 0 & 0 & 0 \\ & & & & \times & 1 & 1 & 0 \\ & & & & & \times & 0 & 1 \\ & & & & & & \times & 1 \\ & & & & & & & \times \end{bmatrix} \end{array}, \tag{4.4}$$

where we only provide the upper triangular part of the symmetric matrix for clarity. Furthermore, the crosses on the main diagonal indicate that quads cannot be connected to themselves.

The goal then is to extract all elements from the adjacency matrix that connect cluster $\mathcal{A}$ to $\mathcal{B}$, which, in this case, is C_{34}. In order to find such elements, we define the adjacency sub-matrices $C^{\mathcal{A}}$ en $C^{\mathcal{B}}$ that are constructed from C as follows. We define a sub-matrix $\mathcal{A}$ for which we retain only the rows and columns of C that belong to $\mathcal{A}$, and we follow a similar procedure to construct $\mathcal{B}$. We then find that

$$C^{\mathcal{A}} = \begin{bmatrix} \times & 1 & 1 & 0 & 0 & 0 & 0 & 0 \\ & \times & 0 & 1 & 0 & 0 & 0 & 0 \\ & & \times & 1 & 0 & 0 & 0 & 0 \\ & & & \times & 1 & 0 & 0 & 0 \\ & & & & \times & 0 & 0 & 0 \\ & & & & & \times & 0 & 0 \\ & & & & & & \times & 0 \\ & & & & & & & \times \end{bmatrix} \text{ and } C^{\mathcal{B}} = \begin{bmatrix} \times & 0 & 0 & 0 & 0 & 0 & 0 & 0 \\ & \times & 0 & 0 & 0 & 0 & 0 & 0 \\ & & \times & 0 & 0 & 0 & 0 & 0 \\ & & & \times & 1 & 0 & 0 & 0 \\ & & & & \times & 1 & 1 & 0 \\ & & & & & \times & 0 & 1 \\ & & & & & & \times & 1 \\ & & & & & & & \times \end{bmatrix}. \tag{4.5}$$

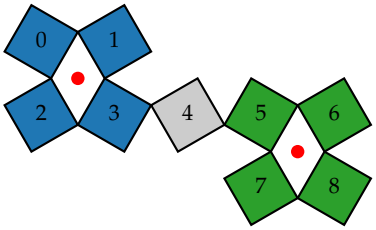

Figure 4.18: Type 1 constraint. The blue cluster ($\mathcal{A}$) and the green cluster ($\mathcal{B}$) are connected via a single quad (4), that is neither a member of $\mathcal{A}$ nor of $\mathcal{B}$.

Finally, two clusters share a type 2 constraint for all ij that satisfy $C_{ij}^{\mathcal{A}} = C_{ij}^{\mathcal{B}} \neq 0$.

4.A.3 Type 1 constraint

We now discuss type 1 constraints [Fig. 4.18], which are most difficult to detect. To find this constraint type, we first determine the system's adjacency matrix, yielding

$$C = \begin{array}{c} \text{label} \\ 0 \\ 1 \\ 2 \\ 3 \\ 4 \\ 5 \\ 6 \\ 7 \\ 8 \end{array} \begin{array}{c} \begin{array}{ccccccccc} 0 & 1 & 2 & 3 & 4 & 5 & 6 & 7 & 8 \end{array} \\ \left[\begin{array}{ccccccccc} \times & 1 & 1 & 0 & 0 & 0 & 0 & 0 & 0 \\ 1 & \times & 0 & 1 & 0 & 0 & 0 & 0 & 0 \\ 1 & 0 & \times & 1 & 0 & 0 & 0 & 0 & 0 \\ 0 & 1 & 1 & \times & 1 & 0 & 0 & 0 & 0 \\ 0 & 0 & 0 & 1 & \times & 1 & 0 & 0 & 0 \\ 0 & 0 & 0 & 0 & 1 & \times & 1 & 1 & 0 \\ 0 & 0 & 0 & 0 & 0 & 1 & \times & 0 & 1 \\ 0 & 0 & 0 & 0 & 0 & 1 & 0 & \times & 1 \\ 0 & 0 & 0 & 0 & 0 & 0 & 1 & 1 & \times \end{array}\right] \end{array}. \tag{4.6}$$

Subsequently, we eliminate all internal bonds of cluster $\mathcal{A}$ and $\mathcal{B}$. Put differently, we cut all bonds between quads that constitute cluster $\mathcal{A}$ and $\mathcal{B}$. This is equivalent to setting all columns of C associated with quads in $\mathcal{A}$ and $\mathcal{B}$ to zero. The resulting reduced matrix then leaves us with all connections to quads that neither are in $\mathcal{A}$ nor in $\mathcal{B}$. Performing this procedure on C reveals that only elements C_{34} and C_{54} would persist. Since quad 4 is connected to quad 3, which is in $\mathcal{A}$, and quad 5, which is in $\mathcal{B}$, these clusters must be connected through a type 1 constraint.

Summary

Mechanical metamaterials are man-made materials which derive their unusual properties from their structure rather than their composition. Their structure, or architecture, often consists of periodically arranged building blocks whose mutual interactions realize unusual properties. In this thesis, we study the role of two aspects of mechanical metamaterials: (i) the beam ligaments and (ii) the microstructures of hinging squares. Both provide functionality to a wide variety of mechanical metamaterials [4, 20, 25–29, 36–38, 40, 44]. However, as we motivate in the introductory chapter of this thesis, several open problems arise on both aspects. First, although the mechanical behaviour of slender beam ligaments is well understood, the finite-width ligaments that often occur in mechanical metamaterials lead to new physics; wide beams exhibit a negative post-buckling stiffness, characterized by a decreasing force after buckling, which is not well understood. Second, fully filled microstructures of hinging squares constitute an auxetic mechanism [1, 20], but possible new zero modes derived from (diluted) microstructures with missing squares remain largely unexplored. How do the number of zero modes increase in diluted systems of hinging squares, can we count these, and what is the spatial structure of such modes? In this thesis, we address these open problems, thereby providing the necessary understanding to fully leverage the characteristics of wide beam ligaments and diluted collections of hinging squares for the design of novel mechanical functionalities.

In **chapter 2** we focus on beams and develop a 1D nonlinear model to describe the negative post-buckling stiffness, or subcritical buckling, of wide neo-Hookean [52] beams. We start by demonstrating that subcritical buckling is a robust phenomenon that does not originate from boundary-induced singularities nor from 3D effects. To this end, we compare experiments and fully realistic 3D numerical simulations against 2D simulations with idealized boundary conditions. In all cases, we find that the post-buckling stiffness of wide beams varies systematically with the beams aspect ratio t, and becomes negative for $t \gtrsim 0.12$. This allows us to focus on the simpler 2D setting to pinpoint the physical mechanism at stake in subcritical buckling. Specifically, we show that the missing crucial ingredient to account for subcritical buckling is the material nonlinearity in the axial stress-strain relation, which is due to the large deformations involved in wide beam buckling. We then construct an 1D energy density

functional by combining the Mindlin-Reissner beam description [41] with a nonlinearity in the axial stress-strain relation, and derive a closed set of beam equations by minimizing the beam's elastic energy. We have solved these equations analytically to determine the post-buckling stiffness in this model, and find excellent agreement between theory, experiments and simulations, without adjustable parameters. Altogether, the work presented in this chapter extends the understanding of the post-buckling of structures featuring wide elastic beams and opens up avenues for the design of post-instabilities in metamaterials.

In **chapter 3** we study the anomalous excess zero modes that arise in randomly diluted collections of rigid quadrilaterals, linked at their tips. The most basic example of an excess zero mode occurs for systems of full filling (no quads removed). Whereas large systems of generic quads are rigid, in contrast, large symmetric systems featuring regular, identical squares posses one global hinging zero mode [1, 20], irrespective of size. Here we focus on the number of excess zero modes, defined as the difference between the number of zero modes in symmetric and generic systems with identical dilution patterns. We perform a large number of independent simulations and show that the average number of excess zero modes as function of the number of removed quads exhibits a peak that exceeds one; this indicates there exist dilution patterns featuring more than one excess zero mode. By quantifying this (average) maximum as function of system size and the fraction of removed quads, we demonstrate that the number of excess zero modes is an intrinsic quantity, which exhibits finite size scaling with simple mean field exponents. Furthermore, we periodically tile a 6×6 unit cell to design dilution geometries with a density of zero modes that is six times higher than the peak value for random cutting, independent of system size. Lastly, we study the occurrence of excess zero modes for random bond removal and find strong similarities with the scaling behaviour for quad removal. In summary, this chapter demonstrates the existence of an arbitrary number of excess zero modes in randomly diluted systems of hinging squares.

In **chapter 4**, the final chapter of this thesis, we develop an approximate method to count the number of (excess) zero modes in systems of hinging squares. Starting from the observation that the occurrence of excess modes is driven by densely connected patches of quads (which have one zero mode in the symmetric case, but no zero modes in the

generic case), we develop a procedure to partition a given system into clusters, connectors and remaining quads. We demonstrate that the remaining quads contribute very similarly to the number of zero modes in the generic and symmetric case, and are thus irrelevant for the number of excess zero modes. This allows us to focus on the simplified, pruned systems, which solely consist of clusters and connectors. To estimate the number of (excess) zero modes in the pruned systems we treat the clusters as 'black boxes' with four degrees of freedom (translation, rotation and hinging), and demonstrate how their motions are constrained by the presence of three type of connectors. One subtle feature of strongly connected clusters is that these exhibit inter-cluster self-stresses due to redundant connectors, and we eliminate most of these self-stresses by the iterative merging of clusters. This procedure yields an iterative discrete algorithm that estimates the number of zero modes. We finally compare these predictions against exact Hessian-based results, and find that our estimate is a tight lower bound on the number of (excess) zero modes of the pruned systems. Hence, we are able to predictively understand the number of (excess) zero modes in diluted systems of hinging squares.

Samenvatting

Mechanische metamaterialen zijn kunstmatige materialen die hun bijzondere eigenschappen danken aan hun structuur en niet zozeer aan de eigenschappen van het materiaal waaruit deze gefabriceerd zijn. Deze structuur, of architectuur, bestaat vaak uit periodiek geordende bouwstenen, waarvan het collectief gedrag leidt tot bijzondere (macroscopische) eigenschappen. In dit proefschrift beschouwen we twee aspecten van mechanische metamaterialen: (i) flexibele staafverbindingen en (ii) microstructuren bestaande uit scharnierende vierkantjes. Beide aspecten spelen een belangrijke rol in een breed scala aan metamaterialen [4, 20, 25–29, 36–38, 40, 44]. Echter roept de toepassing van beide aspecten ook nieuwe, ontbeantwoorde vragen op, zoals we motiveren in het introductiehoofdstuk van dit proefschrift. Ten eerste, alhoewel het mechanische gedrag van dunne staven goed begrepen is, introduceren staven met een eindige dikte, zoals die veelal voorkomen in mechanische metamaterialen, nieuwe fysica die nog niet goed begrepen wordt; brede staven vertonen een negatieve stijfheid, gekarakteriseerd door een afnemende kracht voor toenemende compressie, na het optreden van de knikinstabiliteit. Ten tweede, volledig gevulde microstructuren van scharnierende vierkantjes bezitten precies één (globale) vrije beweging die wordt gekenmerkt door het collectief, tegenovergesteld roteren van vierkantjes [1, 20], maar potentiële vrije bewegingen die voortkomen uit (uitgedunde) microstructuren met missende vierkantjes zijn volledig onverkend gebleven. Hoe groeit het aantal vrije bewegingen in systemen met missende vierkantjes, kunnen we deze tellen, en wat is de ruimtelijke structuur van deze nieuwe vrije bewegingen? In dit proefschrift beantwoorden we de bovengenoemde open vragen. Hiermee verschaffen we de nodige inzichten om de eigenschappen van dikke staven en uitgedunde verzamelingen van scharnierende vierkantjes volledig te begrijpen, alvorens deze met volle potentie kunnen worden ingezet voor het ontwerp van nieuwe mechanische functionaliteiten.

In **hoofdstuk 2** focussen we op staven en ontwikkelen we een niet-linear 1D model om de negatieve stijfheid na de knikinstabiliteit, ook wel subkritisch knikken genoemd, van dikke 'neo-Hookean' [52] staven te beschrijven. Om dit model te ontwikkelen laten we eerst zien dat subkritisch knikgedrag een robuust verschijnsel is dat niet wordt veroorzaakt door 3D effecten of singulariteiten als gevolg van randeffecten. We doen

dit door experimenten en volledig realistische 3D simulaties te vergelijken met 2D simulaties met sterk versimpelde randcondities. Voor alle drie de gevallen vinden we dat de stijfheid na de knikinstabiliteit systematisch varieert met de breedte-lengte verhouding, t, en dat deze negatief wordt voor $t \gtrsim 0.12$. Om het fysische mechanisme dat verantwoordelijk is voor het subkritische knikgedrag te achterhalen, richten we ons op de meest simpele, 2D situatie. We laten in het bijzonder zien dat het cruciale, missende ingredient om het subkritische knikgedrag correct te beschrijven de niet-lineariteit in de axiale spanning-rek relatie is, als gevolg van de grote deformaties die verbonden zijn met het knikken van dikke staven. Vervolgens gebruiken we dit inzicht om een niet-lineare 1D energiedichtheids-functionaal op te stellen door de Mindlin-Reissner beschrijving voor staven [41] te combineren met een niet-lineariteit in de axiale spanning-rek relatie; minimalisatie van de totale elastische energie van de staaf op basis van deze energiedichtheid resulteert in een gesloten set van staafvergelijkingen. We hebben deze vergelijkingen analytisch opgelost voor de stijfheid na de knikinstabiliteit, en we vinden een uitstekende overeenkomst tussen theorie, experimenten en simulaties, zonder het gebruik van vrije parameters. Het werk in dit hoofdstuk leidt hiermee tot een beter begrip van het mechanisch gedrag van structuren waarin dikke staven functionaliteit leveren, en het biedt tevens handvatten om mechanisch gedrag na het optreden van (knik)instabiliteiten goed doordacht te ontwerpen.

In **hoofdstuk 3** bestuderen we buitengewone vrije bewegingen die verschijnen in willekeurig uitgedunde verzamelingen van rigide vierhoekjes, die verbonden zijn aan hun hoekpunten. Het simpelste voorbeeld van een buitengewone vrije beweging treedt op in volledig gevulde systemen, waarin (nog) geen vierhoekjes zijn verwijderd. Grote systemen bestaande uit generieke vierhoekjes zijn rigide, maar grote symmetrische systemen die bestaan uit identieke *vierkantjes* bezitten precies één vrije beweging [1, 20], onafhankelijk van de systeemgrootte. In dit hoofdstuk richten we ons op het aantal buitengewone vrije bewegingen in uitgedunde systemen, gedefinieerd als het verschil tussen het aantal vrije bewegingen in symmetrische en generieke systemen, met een identiek patroon van verwijderde vierhoekjes. Door een groot aantal onafhankelijke simulaties uit te voeren, laten we zien dat het gemiddelde aantal buitengewone vrije bewegingen als functie van het aantal verwijderde

vierhoekjes een maximum heeft dat groter is dan één; dit toont aan dat er uitgedunde systemen van vierhoekjes bestaan met meer dan één buitengewone vrije beweging. Vervolgens quantificeren we dit (gemiddelde) maximum als functie van de systeemgrootte en de fractie van het aantal verwijderde vierhoekjes, en demonstreren we dat het aantal buitengewone vrije bewegingen een intrinsieke grootheid is die beschreven wordt door schalingsrelaties met simpele, gemiddelde exponenten. Daarnaast ontwerpen we een periodieke bouwsteen bestaande uit 6×6 vierhoekjes, waaruit we grotere systemen opbouwen met een dichtheid aan buitengewone vrije bewegingen die zes keer hoger is dan de piekwaarde van willekeurig uitgedunde systemen, onafhankelijk van de systeemgrootte. Als laatste bestuderen we het optreden van buitengewone vrije bewegingen voor het verwijderen van de verbindingen tussen de hoekpunten van vierhoekjes, en hiervoor vinden we sterke overeenkomsten met het beschreven schalingsgedrag voor verwijderde vierkantjes. In conclusie, dit hoofdstuk toont aan dat er een arbitrair aantal buitengewone vrije bewegingen bestaat in willekeurig uitgedunde verzamelingen van scharnierende vierkantjes.

In **hoofdstuk 4**, het laatste hoofdstuk van dit proefschrift, ontwikkelen we een telmethode om het aantal (buitengewone) vrije bewegingen voor systemen van scharnierende vierkantjes te benaderen. Beginnend met de observatie dat het verschijnen van buitengewone vrije bewegingen wordt veroorzaakt door verbonden gebiedjes van vierhoekjes (die één vrije beweging hebben in het symmetrische geval, maar geen vrije beweging in het generieke geval), ontwikkelen we een procedure om een gegeven systeem onder te verdelen in clusters, connectoren en overblijvende vierhoekjes. We laten zien dat de overblijvende vierhoekjes vrijwel altijd gelijkwaardig bijdragen aan het aantal vrije bewegingen in het generieke en symmetrische geval, zodat deze irrelevant zijn voor het aantal buitengewone vrije bewegingen. We vestigen onze aandacht daarom op de versimpelde, gereduceerde systemen, die uitsluitend bestaan uit clusters en connectoren. Om het aantal (buitengewone) vrije bewegingen in de gereduceerde systemen te benaderen, beschouwen we de clusters als 'zwarte dozen' met vier vrijheidsgraden (translatie, rotatie en scharnieren), en laten we zien hoe de bewegingingen tussen clusters worden beperkt door de aanwezigheid voor ieder van de drie verschillende typen connectoren die optreden. Een subtiele eigenschap van sterk verbonden clusters

is dat deze zogenaamde zelf-spanningen bezitten als gevolg van overtollige connectoren. Om het aantal vrije bewegingen correct te benaderen, elimineren we de meeste van deze zelf-spanningen door het iteratief samenvoegen van sterk verbonden clusters. Deze procedure resulteert in een discreet algoritme dat het aantal vrije bewegingen stapsgewijs benadert. Uiteindelijk vergelijken we de voorspellingen die volgen uit ons algoritme met exacte berekeningen gebaseerd op de Hessiaan, waarmee we demonstreren dat ons algoritme een nauwkeurige ondergrens oplevert voor het aantal (buitengewone) vrije bewegingen in de gereduceerde systemen. We zijn daarmee dus in staat om het aantal (buitengewone) vrije bewegingen in uitgedunde systemen van scharnierende vierkantjes te voorspellen.

Publication list

On work presented in this thesis:

(8) L.A. Lubbers and M. van Hecke
Excess floppy modes in metamaterials with symmetries.
In preparation for Phys. Rev. Lett.

(7) L.A. Lubbers, M. van Hecke and C. Coulais
A nonlinear beam model to describe the postbuckling of wide neo-Hookean beams.
J. Phys. Mech. Solids **106**, 191-206 (2017).

(6) C. Coulais, J.T.B. Overvelde, L.A. Lubbers, K. Bertoldi and M. van Hecke
Discontinuous buckling of wide beams and metabeams.
Phys. Rev. Lett. **115**, 044301 (2015).
Featured as a Synopsis in Physics

On other work:

(5) S. Karpitschka, A. Pandey, L.A. Lubbers, J.H. Weijs, L. Botto, S. Das, B. Andreotti and J.H. Snoeijer
Dynamical theory of the inverted Cheerios effect.
Soft Matter **13**, 6000-6010 (2017).

(4) S. Karpitschka, A. Pandey, L.A. Lubbers, J.H. Weijs, L. Botto, S. Das, B. Andreotti and J.H. Snoeijer
Liquid drops attract or repel by the inverted Cheerios effect.
PNAS **113**, 7403 (2016).
Featured in The New York Times

(3) L.A. Lubbers, Q. Xu, S. Wilken, W.W. Zhang and H.M. Jaeger
Dense suspension splat: Monolayer spreading and hole formation after impact.
Phys. Rev. Lett. **113**, 044502 (2014).
Featured as a Synopsis in Physics

(2) L.A. Lubbers, J.H. Weijs, L. Botto, S. Das, B. Andreotti and J.H. Snoeijer
Drops on soft solids: free energy and double transition of contact angles.
J. Fluid Mech. **747**, R1 (2014).

(1) J. F. Hernández-Sánchez, L. A. Lubbers, A. Eddi and J. H. Snoeijer
Symmetric and asymmetric coalescence of drops on a substrate.
Phys. Rev. Lett. **109**, 184502 (2012).

Curriculum vitae

I was born on June 3rd, 1989 in Oldenzaal, the Netherlands. I grew up in the neighbouring village Denekamp and attended my secondary education at the *Twents Carmel College* with joint locations in Denekamp and Oldenzaal.

After obtaining my vwo degree in 2007, I directly started my BSc studies in Applied Physics at the *University of Twente* with a minor in Aircraft Engineering. In 2011, I completed my bachelors *cum laude* with a research project in the Optical Sciences group titled *Analyzing and simulating the coherent control model*. I then continued with the MSc programme in Applied Physics specializing in fluid physics, at the same university. During my masters I worked on three major projects, all of which have been published (see publications). The first project was an optional capita selecta project on drop coalescence performed at the Physics of Fluids (PoF) group in Twente, and the second project was an internship at the *James Franck Institute* in Chicago, on the impact of dense suspensions on solid surfaces. The third and final project was my master thesis titled *Liquid drops on soft solids*, again carried out within the PoF group. I received my MSc degree *cum laude* in November 2013.

Throughout my Bsc and MSc studies I have been teaching assistant for four different undergraduate courses, most of which I supervised three times. I was active simultaneously for *Twente Academy*, where I assisted high school students with their final school research project ('profielwerkstuk'), and organized activities at (primary) schools to introduce the world of science to school children of age 4-14, teachers and parents.

In December 2013, I left the Twente region to start my PhD in physics at *Leiden University* under the supervision of Prof. dr. Martin van Hecke. I presented my work at international conferences in Madrid (Spain), Oxford (United Kingdom), Denver, Purdue, San Antonio, Baltimore and New Orleans (United States). During my PhD, I was teaching assistant for the undergraduate course 'Statistical Physics' (2x) and the graduate course 'Mechanical Metamaterials', and (co)-supervised a number of undergraduate students.

In May 2018, I started working at TNO as Junior Scientist Innovator at the Explosions, Ballistics and Protection department located in Rijswijk.

Acknowledgements

This thesis marks the end of a four-year period of scientific research and the obtained results would not have been possible without the help, support and encouragement of many people who I would like to thank.

Martin, we first met at the Soft Matter meeting in Twente in May 2013 and half a year later I would start my PhD in Leiden. Thank you so much for providing me this opportunity, it has not only broadened my scientific knowledge, but also allowed me to further develop myself on a personal level by moving to a different part of the Netherlands. I furthermore thank you for the scientific support and discussions, which have been invaluable, as well as your excellent empathy for non-scientific related issues. Finally, I felt privileged for the numerous opportunities you gave me (and the group) to travel to international conferences.

Corentin, without a doubt you made my start in Leiden much easier. As an office-mate you quickly familiarized me with beam theory and the simulation package *Abaqus*, helping me tremendously in getting my first project to run. We quickly became a team and our discussions on neo-Hookean elasticity in a later stadium of my PhD have been extremely useful for the work presented in this thesis and our related publications. I furthermore appreciate your great enthusiasm and solid faith that helped getting our beam theory published.

I would like to thank Daniëlle for the always smoothly arranged forms for and during my PhD. Bas Overvelde and Katia Bertoldi, it was great working with you on the metabeam project. Thanks to my colleagues in Leiden and Amsterdam for scientific discussions, support and company during conferences, schools or other activities: Geert, Bastiaan, Peter, Anne, Song-Chuan, Jeroen, Vera, Casper vd W., Daniela, Melissa, Stefania, Indrani, Ruben, Rachel, Koen, Giorgio, Agustin, Jenny and my office mates Scott, Nitin and Matthieu. Merlijn, I would like to thank you in particular for your excellent help with Python and for sharing your code to create good-looking plots. Casper B., Willem and Mara, I enjoyed working with you on your undergraduate projects.

Finally, I wish to express my gratitude to my parents, sisters and friends (7-dagenlang, Enschede, Aquamania and Huize Boot) for the ungoing support. Hebe, even though we are not together anymore, you played an important role during my PhD and I am grateful for that.

Bibliography

[1] K. Bertoldi, V. Vitelli, J. Christensen, and M. van Hecke, "Flexible mechanical metamaterials", Nat. Rev. Mater. **2**, 17066 (2017).

[2] L. D. Landau, L. P. Pitaevskii, A. M. Kosevich, and E. Lifshitz, *Theory of elasticity*, 3rd ed., Vol. 7 (Butterworth-Heinemann, 1986).

[3] R. S. Lakes, "Foam structures with a negative Poisson's ratio", Science **235**, 1038–1040 (1987).

[4] T. Mullin, S. Deschanel, K. Bertoldi, and M. C. Boyce, "Pattern transformation triggered by deformation", Phys. Rev. Lett. **99**, 084301 (2007).

[5] R. S. Lakes and K. Elms, "Indentability of conventional and negative Poisson's ratio foams", J. Compos. Mater. **27**, 1193–1202 (1993).

[6] K. L. Alderson, A. P. Pickles, P. J. Neale, and K. E. Evans, "Auxetic polyethylene: The effect of a negative Poisson's ratio on hardness", Acta Metall. Mater. **42**, 2261 –2266 (1994).

[7] J. B. Choi and R. S. Lakes, "Fracture toughness of re-entrant foam materials with a negative Poisson's ratio: Experiment and analysis", Int. J. Fract. **80**, 73–83 (1996).

[8] F. Scarpa, L. G. Ciffo, and J. R. Yates, "Dynamic properties of high structural integrity auxetic open cell foam", Smart Mater. Struc. **13**, 49 (2004).

[9] K. E. Evans, "The design of doubly curved sandwich panels with honeycomb cores", Compo. Struct. **17**, 95 –111 (1991).

[10] A. Alderson and K. L. Alderson, "Auxetic materials", Proc. Inst. Mech. Eng. G **221**, 565–575 (2007).

[11] Y. Liu and H. Hu, "A review on auxetic structures and polymeric materials", Sci. Res. Essays **5**, 1052–1063 (2010).

[12] F. Scarpa, "Auxetic materials for bioprostheses [In the spotlight]", IEEE Signal Process Mag. **25**, 128–126 (2008).

[13] K. E. Evans and A. Alderson, "Auxetic materials: Functional materials and structures from lateral thinking!", Adv. Mater. **12**, 617–628 (2000).

[14] Q. Liu, "Literature review: Materials with negative Poisson's ratios and potential applications to aerospace and defence", DSTO Group, DTIC Document No. DSTO–GD–0472 (2006).

[15]G. W. Milton, "Composite materials with Poisson's ratios close to -1", J. Mech. Phys. Solids **40**, 1105 –1137 (1992).

[16]E. A. Friis, R. S. Lakes, and J. B. Park, "Negative Poisson's ratio polymeric and metallic foams", J. Mater. Sci. **23**, 4406–4414 (1988).

[17]B. D. Caddock and K. E. Evans, "Microporous materials with negative Poisson's ratios. I. Microstructure and mechanical properties", J. Phys. D. Appl. Phys. **22**, 1877 (1989).

[18]K. E. Evans, M. A. Nkansah, I. J. Hutchinson, and S. C. Rogers, "Molecular network design", Nature **353**, 124 (1991).

[19]M. C. Rechtsman, F. H. Stillinger, and S. Torquato, "Negative Poisson's ratio materials via isotropic interactions", Phys. Rev. Lett. **101**, 085501 (2008).

[20]J. N. Grima and K. E. Evans, "Auxetic behavior from rotating squares", J. Mater. Sci. Lett. **19**, 1563–1565 (2000).

[21]L. J. Gibson and M. F. Ashby, *Cellular solids: Structure and properties* (Cambridge University Press, 1999).

[22]R. S. Lakes, "Deformation mechanisms in negative Poisson's ratio materials: Structural aspects", J. Mater. Sci. **26**, 2287–2292 (1991).

[23]M. van Hecke, "Jamming of soft particles: Geometry, mechanics, scaling and isostaticity", J. Phys. Condens. Matter **22**, 033101 (2009).

[24]L. Euler, "Additamentum I de curvis elasticis, methodus inveniendi lineas curvas maximi minimivi proprietate gaundentes", Opera Omnia I **24**, 232–297 (1774).

[25]K. Bertoldi, M. C. Boyce, S. Deschanel, S. M. Prange, and T. Mullin, "Mechanics of deformation-triggered pattern transformations and superelastic behavior in periodic elastomeric structures", J. Mech. Phys. Solids **56**, 2642 –2668 (2008).

[26]K. Bertoldi, P. M. Reis, S. Willshaw, and T. Mullin, "Negative Poisson's ratio behavior induced by an elastic instability", Adv. Mater. **22**, 361–366 (2010).

[27]J. T. B. Overvelde, S. Shan, and K. Bertoldi, "Compaction through buckling in 2D periodic, soft and porous structures: Effect of pore shape", Adv. Mater. **24**, 2337–2342 (2012).

[28]J. Shim, S. Shan, A. Košmrlj, S. H. Kang, E. R. Chen, J. C. Weaver, and K. Bertoldi, "Harnessing instabilities for design of soft reconfigurable auxetic/chiral materials", Soft Matter **9**, 8198–8202 (2013).

[29]K. Bertoldi, "Harnessing instabilities to design tunable architected cellular materials", Annu. Rev. Mater. Res. **47**, 51–61 (2017).

[30]Z. P. Bažant and L. Cedolin, *Stability of structures: elastic, inelastic, fracture, and damage theories* (Dover Publications, 2003).

[31]P. M. Reis, "A perspective on the revival of structural (in)stability with novel opportunities for function: From Buckliphobia to Buckliphilia", Journal of Applied Mechanics **82**, 111001 (2015).

[32]Y. Forterre, J. M. Skotheim, J. Dumais, and L. Mahadevan, "How the venus flytrap snaps", Nature **433**, 421–425 (2005).

[33]S. Poppinga and M. Joyeux, "Different mechanics of snap-trapping in the two closely related carnivorous plants Dionaea muscipula and Aldrovanda vesiculosa", Phys. Rev. E **84**, 041928 (2011).

[34]W. H. Wittrick, W. H. Wittrick, D. M. Myers, and W. R. Blunden, "Stability of a bimetallic disk", Q. J. Mech. Appl. Math. **6**, 15–31 (1953).

[35]A. Pandey, D. E. Moulton, D. Vella, and D. P. Holmes, "Dynamics of snapping beams and jumping poppers", Europhys. Lett. **105**, 24001 (2014).

[36]J. Shim, C. Perdigou, E. R. Chen, K. Bertoldi, and P. M. Reis, "Buckling-induced encapsulation of structured elastic shells under pressure", Proc. Natl. Acad. Sci. **109**, 5978–5983 (2012).

[37]S. Babaee, J. Shim, J. C. Weaver, E. R. Chen, N. Patel, and K. Bertoldi, "3D soft metamaterials with negative Poisson's ratio", Adv. Mater. **25**, 5044–5049 (2013).

[38]C. Coulais, E. Teomy, K. de Reus, Y. Shokef, and M. van Hecke, "Combinatorial design of textured mechanical metamaterials", Nature **535**, 529–532 (2016).

[39]L. A. Lubbers, M. van Hecke, and C. Coulais, "A nonlinear beam model to describe the postbuckling of wide neo-Hookean beams", J. Mech. Phys. Solids **106**, 191 –206 (2017).

[40]C. Coulais, J. T. B. Overvelde, L. A. Lubbers, K. Bertoldi, and M. van Hecke, "Discontinuous buckling of wide beams and metabeams", Phys. Rev. Lett. **115**, 044301 (2015).

[41]E. Reissner, "On one-dimensional finite-strain beam theory: The plane problem", English, Z. Angew. Math. Phys. **23**, 795–804 (1972).

[42]A. Magnusson, M. Ristinmaa, and C. Ljung, "Behaviour of the extensible elastica solution", Int. J. Solids Struct. **38**, 8441 –8457 (2001).

[43]A. Humer, "Exact solutions for the buckling and postbuckling of shear-deformable beams", Acta Mech. **224**, 1493–1525 (2013).

[44]B. Florijn, C. Coulais, and M. van Hecke, "Programmable mechanical metamaterials", Phys. Rev. Lett. **113**, 175503 (2014).

[45]S. Feng and P. N. Sen, "Percolation on elastic networks: New exponent and threshold", Phys. Rev. Lett. **52**, 216–219 (1984).

[46]S. Feng, M. F. Thorpe, and E. Garboczi, "Effective-medium theory of percolation on central-force elastic networks", Phys. Rev. B **31**, 276–280 (1985).

[47]D. J. Jacobs and M. F. Thorpe, "Generic rigidity percolation: The pebble game", Phys. Rev. Lett. **75**, 4051–4054 (1995).

[48]D. J. Jacobs and M. F. Thorpe, "Generic rigidity percolation in two dimensions", Phys. Rev. E **53**, 3682–3693 (1996).

[49]M. Sahimi, "Non-linear and non-local transport processes in heterogeneous media: From long-range correlated percolation to fracture and materials breakdown", Phys. Rep. **306**, 213 –395 (1998).

[50]W. G. Ellenbroek, V. F. Hagh, A. Kumar, M. F. Thorpe, and M. van Hecke, "Rigidity loss in disordered systems: Three scenarios", Phys. Rev. Lett. **114**, 135501 (2015).

[51]J. C. Maxwell, "L. on the calculation of the equilibrium and stiffness of frames", Philos. Mag. **27**, 294–299 (1864).

[52]R. W. Ogden, *Non-linear elastic deformations* (Dover Publications, 1997).

[53]P. M. Reis, H. M. Jaeger, and M. van Hecke, "Designer matter: A perspective", Extreme Mech. Lett. **5**, 25–29 (2015).

[54]D. P. Holmes and A. J. Crosby, "Snapping surfaces", Adv. Mater. **19**, 3589–3593 (2007).

[55]D. Terwagne, M. Brojan, and P. M. Reis, "Smart surfaces: Smart morphable surfaces for aerodynamic drag control", Adv. Mater. **26**, 6659–6659 (2014).

[56]K. Danas and N. Triantafyllidis, "Instability of a magnetoelastic layer resting on a non-magnetic substrate", J. Mech. Phys. Solids **69**, 67 –83 (2014).

[57]J. S. Biggins, B. Saintyves, Z. Wei, E. Bouchaud, and L. Mahadevan, "Digital instability of a confined elastic meniscus", Proc. Natl. Acad. Sci. **110**, 12545–12548 (2013).

[58]M. P. Brenner, J. H. Lang, J. Li, J. Qiu, and A. H. Slocum, "Optimal design of a bistable switch", Proc. Natl. Acad. Sci. **100**, 9663–9667 (2003).

[59]Q. Wang, Z. Suo, and X. Zhao, "Bursting drops in solid dielectrics caused by high voltages", Nat. Comm. **3**, 1157 (2012).

[60]T. Li, C. Keplinger, R. Baumgartner, S. Bauer, W. Yang, and Z. Suo, "Giant voltage-induced deformation in dielectric elastomers near the verge of snap-through instability", J. Mech. Phys. Solids **61**, 611–628 (2013).

[61]J. T. B. Overvelde, T. Kloek, J. J. A. D'haen, and K. Bertoldi, "Amplifying the response of soft actuators by harnessing snap-through instabilities", Proc. Natl. Acad. Sci. **112**, 10863–10868 (2015).

[62]K. Autumn, Y. A. Liang, S. T. Hsieh, W. Zesch, W. P. Chan, T. W. Kenny, R. Fearing, and R. J. Full, "Adhesive force of a single gecko foot-hair", Nature **405**, 681–685 (2000).

[63]R. F. Shepherd, F. Ilievski, W. Choi, S. A. Morin, A. A. Stokes, A. D. Mazzeo, X. Chen, M. Wang, and G. M. Whitesides, "Multigait soft robot", Proc. Natl. Acad. Sci. **108**, 20400–20403 (2011).

[64]J. W. Hutchinson and W. T. Koiter, "Postbuckling theory", Appl. Mech. Rev. **23**, 1353–1366 (1970).

[65]B. Budiansky, "Theory of buckling and post-buckling behavior of elastic structures", Adv. Appl. Mech. **14**, 1–65 (1974).

[66]J. M. Davies, P. Leach, and D. Heinz, "Second-order generalised beam theory", J. Constr. Steel Res. **31**, 221–241 (1994).

[67]M. A. Vaz and D. F. C. Silva, "Post-buckling analysis of slender elastic rods subjected to terminal forces", Int. J. Nonlinear Mech. **38**, 483–492 (2003).

[68]C. E. N. Mazzilli, "Buckling and post-buckling of extensible rods revisited: A multiple-scale solution", Int. J. Nonlinear Mech. **44**, 200–208 (2009).

[69]G. Geymonat, S. Müller, and N. Triantafyllidis, "Homogenization of nonlinearly elastic materials, microscopic bifurcation and macroscopic loss of rank-one convexity", Arch. Ration. Mech. Anal. **122**, 231–290 (1993).

[70]O. Lopez-Pamies and P. P. Castañeda, "On the overall behavior, microstructure evolution, and macroscopic stability in reinforced rubbers at large deformations: I-Theory", J. Mech. Phys. Solids **54**, 807–830 (2006).

[71]O. Lopez-Pamies and P. P. Castañeda, "On the overall behavior, microstructure evolution, and macroscopic stability in reinforced rubbers at large deformations: II-Application to cylindrical fibers", J. Mech. Phys. Solids **54**, 831–863 (2006).

[72]J.-C. Michel, O. Lopez-Pamies, P. P. Castañeda, and N. Triantafyllidis, "Microscopic and macroscopic instabilities in finitely strained porous elastomers", J. Mech. Phys. Solids **55**, 900–938 (2007).

[73]A. Goriely, R. Vandiver, and M. Destrade, "Nonlinear Euler buckling", Proc. Royal Soc. A **464**, 3003–3019 (2008).

[74]S. P. Timoshenko and J. M. Gere, *Theory of elastic stability* (Dover Publications, 2012).

[75]E. L. Reiss, "Column buckling—an elementary example of bifurcation", in *Bifurcation theory and nonlinear eigenvalue problems*, edited by J. B. Keller and S. Antman (W. A. Benjamin, New York, 1969), pp. 1–16.

[76]S. S. Antman, "The theory of rods", in *Linear theories of elasticity and thermoelasticity* (Springer, 1973), pp. 641–703.

[77]S. S. Antman and G. Rosenfeld, "Global behavior of buckled states of nonlinearly elastic rods", SIAM Rev. **20**, 513–566 (1978).

[78]S. S. Antman and J. F. Pierce, "The intricate global structure of buckled states of compressible columns", SIAM J. Appl. Math. **50**, 395–419 (1990).

[79]Y. Goto, T. Yamashita, and S. Matsuura, "Elliptic integral solutions for extensional elastica with constant initial curvature", Struct. Eng./Earthq. Eng. **4**, 299–309 (1987).

[80]G. Yoshiaki, Y. Tomoo, and O. Makoto, "Elliptic integral solutions of plane elastica with axial and shear deformations", Int. J. Solids Struct. **26**, 375–390 (1990).

[81]A. Pflüger, *Stabilitätsprobleme der elastostatik* (Springer, 2013).

[82]J. C. Simo and L. Vu-Quoc, "On the dynamics in space of rods undergoing large motions—A geometrically exact approach", Comput. Methods Appl. Mech. Eng. **66**, 125–161 (1988).

[83]C. Y. Wang, "Post-buckling of a clamped-simply supported elastica", Int. J. Nonlinear Mech. **32**, 1115–1122 (1997).

[84]H. Irschik and J. Gerstmayr, "A continuum mechanics based derivation of Reissner's large-displacement finite-strain beam theory: The case of plane deformations of originally straight Bernoulli-Euler beams", Acta Mech. **206**, 1–21 (2009).

[85]E. Reissner, "On one-dimensional large-displacement finite-strain beam theory", Stud. Appl. Math. **52**, 87–95.

[86]J. C. Simo, "A finite strain beam formulation. The three-dimensional dynamic problem. Part I", Comput. Methods Appl. Mech. Eng. **49**, 55–70 (1985).

[87]J. C. Simo and L. Vu-Quoc, "A three-dimensional finite-strain rod model. Part II: Computational aspects", Comput. Methods Appl. Mech. Eng. **58**, 79–116 (1986).

[88]J. C. Simo and L. Vu-Quoc, "A geometrically-exact rod model incorporating shear and torsion-warping deformation", Int. J. Solids Struct. **27**, 371–393 (1991).

[89]L. Pocivavsek, R. Dellsy, A. Kern, S. Johnson, B. Lin, K. Y. C. Lee, and E. Cerda, "Stress and fold localization in thin elastic membranes", Science **320**, 912–916 (2008).

[90]H. Diamant and T. A. Witten, "Compression induced folding of a sheet: an integrable system", Phys. Rev. Lett. **107**, 164302 (2011).

[91]B. Audoly, "Localized buckling of a floating elastica", Phys. Rev. E **84**, 011605 (2011).

[92]C. Coulais, "Periodic cellular materials with nonlinear elastic homogenized stress-strain response at small strains", Int. J. Solids Struct. **97-98**, 226–238 (2016).

[93]M. C. Boyce and E. M. Arruda, "Constitutive models of rubber elasticity: A review", Rubber Chem. Technol. **73**, 504–523 (2000).

[94]R. Narayanasamy, R. S. N. Murthy, K. Viswanatham, and G. R. Chary, "Prediction of the barreling of solid cylinders under uniaxial compressive load", J. Mech. Work Technol. **16**, 21–30 (1988).

[95]I. Doghri, *Mechanics of deformable solids: Linear, nonlinear, analytical and computational aspects* (Springer, 2000).

[96]M.-W. Moon, S. H. Lee, J.-Y. Sun, K. H. Oh, A. Vaziri, and J. W. Hutchinson, "Wrinkled hard skins on polymers created by focused ion beam", Proc. Natl. Acad. Sci. **104**, 1130–1133 (2007).

[97]J. Huang, M. Juszkiewicz, W. H. de Jeu, E. Cerda, T. Emrick, N. Menon, and T. P. Russell, "Capillary wrinkling of floating thin polymer films", Science **317**, 650–653 (2007).

[98]Y. Cao and J. W. Hutchinson, "From wrinkles to creases in elastomers: The instability and imperfection-sensitivity of wrinkling", Proc. Royal Soc. A **468**, 94–115 (2011).

[99]B. Audoly and Y. Pomeau, *Elasticity and geometry: From hair curls to the nonlinear response of shells* (Oxford University Press, 2010).

[100]J. N. Goodier and S. P. Timoshenko, *Theory of elasticity*, 3rd ed. (McGraw-Hill Education, 1970).

[101]S. P. Timoshenko, "On the transverse vibrations of bars of uniform cross-section", Philos. Mag. **43**, 125–131 (1922).

[102]S. P. Timoshenko, "On the correction for shear of the differential equation for transverse vibrations of prismatic bars", Philos. Mag. **41**, 744–746 (1921).

[103]G. R. Cowper, "The shear coefficient in Timoshenko's beam theory", J. Appl. Mech. **33**, 335–340 (1966).

[104]J. R. Hutchinson, "Shear coefficients for Timoshenko beam theory", J. Appl. Mech. **68**, 87–92 (2000).

[105]S. T. Thornton and J. B. Marion, *Classical dynamics of particles and systems*, 5th ed. (Brooks Cole, 2003).

[106]J. Guckenheimer and P. Holmes, *Nonlinear oscillations, dynamical systems, and bifurcations of vector fields*, Vol. 42 (Springer, 1983).

[107]P. P. Castañeda", "The effective mechanical properties of nonlinear isotropic composites", J. Mech. Phys. Solids **39**, 45–71 (1991).

[108]M. F. Ashby and Y. J. M. Bréchet, "Designing hybrid materials", Acta Mater. **51**, 5801–5821 (2003).

[109]Y. Cho, J.-H. Shin, A. Costa, T. A. Kim, V. Kunin, J. Li, S. Y. Lee, S. Yang, H. N. Han, I.-S. Choi, and D. J. Srolovitz, "Engineering the shape and structure of materials by fractal cut", Proc. Natl. Acad. Sci. **111**, 17390–17395 (2014).

[110]S. Yang, I.-S. Choi, and R. D. Kamien, "Design of super-conformable, foldable materials via fractal cuts and lattice kirigami", MRS Bull. **41**, 130–138 (2016).

[111]J. Yoon, S. Cai, Z. Suo, and R. C. Hayward, "Poroelastic swelling kinetics of thin hydrogel layers: Comparison of theory and experiment", Soft Matter **6**, 6004–6012 (2010).

[112]D. P. Holmes, M. Roche, T. Sinha, and H. A. Stone, "Bending and twisting of soft materials by non-homogenous swelling", Soft Matter **7**, 5188–5193 (2011).

[113]J. Kim, J. A. Hanna, M. Byun, C. D. Santangelo, and R. C. Hayward, "Designing responsive buckled surfaces by halftone gel lithography", Science **335**, 1201–1205 (2012).

[114]M. Pezzulla, S. A. Shillig, P. Nardinocchi, and D. P. Holmes, "Morphing of geometric composites via residual swelling", Soft Matter **11**, 5812–5820 (2015).

[115]J.-H. Na, N. P. Bende, J. Bae, C. D. Santangelo, and R. C. Hayward, "Grayscale gel lithography for programmed buckling of non-euclidean hydrogel plates", Soft Matter **12**, 4985–4990 (2016).

[116]A. Sydney Gladman, E. A. Matsumoto, R. G. Nuzzo, L. Mahadevan, and J. A. Lewis, "Biomimetic 4D printing", Nat. Mater. **15**, 413–418 (2016).

[117]A. Sharma, A. J. Licup, K. A. Jansen, R. Rens, M. Sheinman, G. H. Koenderink, and F. C. MacKintosh, "Strain-controlled criticality governs the nonlinear mechanics of fibre networks", Nat. Phys. **12**, 584–587 (2016).

[118]P. Wang, F. Casadei, S. Shan, J. C. Weaver, and K. Bertoldi, "Harnessing buckling to design tunable locally resonant acoustic metamaterials", Phys. Rev. Lett. **113**, 014301 (2014).

[119]A. Nasto, A. Ajdari, A. Lazarus, A. Vaziri, and P. M. Reis, "Localization of deformation in thin shells under indentation", Soft Matter **9**, 6796–6803 (2013).

[120]T. Frenzel, C. Findeisen, M. Kadic, P. Gumbsch, and M. Wegener, "Tailored buckling microlattices as reusable light-weight shock absorbers", Adv. Mater. **28**, 5865–5870.

[121]J. R. Raney, N. Nadkarni, C. Daraio, D. M. Kochmann, J. A. Lewis, and K. Bertoldi, "Stable propagation of mechanical signals in soft media using stored elastic energy", Proc. Natl. Acad. Sci. **113**, 9722–9727 (2016).

[122]C. Coulais, D. Sounas, and A. Alù, "Static non-reciprocity in mechanical metamaterials", Nature **542**, 461–464 (2017).

[123]D. Lay, *Linear algebra and its applications* (Addison-Wesley, Reading, Mass, 2003).

[124]W. Feller, *An introduction to probability theory and its applications*, Vol. 2 (John Wiley & Sons, 2008).